

INVESTIGATION AND MATHEMATICAL MODELING OF ACOUSTIC RELEASE OF
DOXORUBICIN FROM MICELLES

by

Youssef Ashraf Alhariri

A Thesis Presented to the Faculty of the
American University of Sharjah
College of Engineering
In Partial Fulfillment
of the Requirements
for the Degree of

Master of Science in
Chemical Engineering

Sharjah, United Arab Emirates

July 2020

Declaration of Authorship

I declare that this thesis is my own work and, to the best of my knowledge and belief, it does not contain material published or written by a third party, except where permission has been obtained and/or appropriately cited through full and accurate referencing.

Signature Youssef Ashraf Alhariri

Date 22/7/2020

The Author controls copyright for this report.

Material should not be reused without the consent of the author. Due acknowledgement should be made where appropriate.

© Year 2020

Youssef Ashraf Alhariri

ALL RIGHTS RESERVED

Approval Signatures

We, the undersigned, approve the Master's Thesis of Youssef Ashraf Alhariri

Thesis Title: Investigation and Mathematical Modeling of Acoustic Release of Doxorubicin from Micelles

Date of Defense: 21-May-2020

| Name, Title and Affiliation | Signature |
|--|------------------|
| Dr. Ghaleb Husseini Professor, Department of Chemical Engineering Thesis Advisor | |
| Dr. Rana Sabouni Assistant Professor, Department of Chemical Engineering Thesis Co-Advisor | |
| Dr. Nai-Shyong Yeh Professor of Practice, Department of Chemical Engineering Thesis Committee Member | |
| Dr. Nahid Awad Visiting Scholar Thesis Committee Member | |
| Dr. Sameer Al-Asheh Interim Head of Department Department of Chemical Engineering | |
| Dr. Lotfi Romdhane Associate Dean for Graduate Studies and Research College of Engineering | |
| Dr. Sirin Tekinay Dean College of Engineering | |
| Dr. Mohamed El-Tarhuni Vice Provost for Graduate Studies Office of Graduate Studies | |

Acknowledgment

All praise is due to Allah Almighty, who is the source of all knowledge in this world and whose countless bounties have enabled me to work and complete this thesis successfully.

I would not have been able to finish my thesis without the guidance of my committee members, help from friends, and support from my dear family.

I would like to sincerely thank both my advisors Dr. Ghaleb Husseini and Dr. Rana Sabouni, for providing knowledge, guidance, support, and motivation throughout my research stages. I am deeply thankful for their generous aid, worthy discussions, and suggestions.

I also offer my gratitude to my father and my mother. My research would not have been possible without their help, their constant support and encouragement, and their good wishes.

I would like to express my gratitude to the American University of Sharjah for granting me graduate teaching assistant scholarship which enabled me to complete my degree and a chance to gain experience in academia.

Dedication

To my dear father, to my beloved mother, and to my dear sister, in recognition of your endless love, support, and encouragement.

Abstract

Given the growing concern over the increasing number of people diagnosed with cancer and the high prevalence of unwanted side effects associated with chemotherapy on healthy tissues, this thesis aims to provide better, safer, and more effective treatment modalities. In this work, a targeted nanocarrier is loaded with an anti-cancer drug. Results of ultrasound release experiments are used to compare the response of different micellar types to acoustic waves. The investigated micelles include non-targeted micelles, folated micelles, micelles stabilized using an interpenetrating network of N,N-diethylacrylamide, and micelles formed using PEO-b-poly(NIPAAm-co-HEMA-lactate_n). Acoustic release of the chemotherapeutic drug Doxorubicin (DOX) from micelles, was investigated using both 70-kHz and 80-kHz ultrasound at the following power densities: 0.76, 2.389, 2.546, 3.540, 5.013, 5.432, and 5.914 W/cm². Next, mathematical modeling is applied to capture drug release kinetics from these nanovehicles. The investigated models are zero-order, first-order, Higuchi, Hixon-Crowell, Korsmeyer-Peppas, Weibull, Baker-Lonsdale, and Hopfenberg. Using statistics and the rate constants deduced, the effects of temperature, power density, and micellar type on drug release were investigated. Results showed that the release from folated micelles is slightly higher compared to release from non-folated micelles. This may be due to the conjugation of the folate moiety, which renders the micelles more sensitive to ultrasound (sonosensitive), by reducing their stability. Moreover, an increase in any of the experimental variables (mechanical index, temperature, or power density) leads to an increase in the percent of drug released. Finally, the Higuchi model provided the best fit to the experimental data, which means that the acoustic data available conform to this model's assumptions and release mechanism. In conclusion, using micelles as drug delivery carriers and ultrasound as a trigger modality may reduce the side effects associated with chemotherapy.

Keywords: *cancer; micelles; targeting; moieties; Pluronic P105; folic acid.*

Table of Contents

| | |
|---|----|
| List of Figures | 9 |
| List of Tables | 12 |
| Chapter 1. Introduction | 13 |
| 1.1. Overview | 13 |
| 1.2. Thesis Objectives | 16 |
| Chapter 2. Background and Literature Review..... | 17 |
| 2.1. Micelles | 17 |
| 2.2. Targeting Schemes | 18 |
| 2.2.1. Passive targeting. | 19 |
| 2.2.2. Active targeting..... | 20 |
| 2.3. Targeting Moieties | 20 |
| 2.3.1. Transferrin..... | 21 |
| 2.3.2. Aptamers..... | 22 |
| 2.3.3. Antibodies..... | 22 |
| 2.3.4. Peptides..... | 23 |
| 2.3.5. Folic acid..... | 23 |
| 2.4. Ultrasound | 24 |
| Chapter 3. Materials and Methods | 26 |
| 3.1. Materials..... | 26 |
| 3.1.1. Preparation of pluronic p105 (non-stabilized micelles)..... | 26 |
| 3.1.2. Preparation of stabilized P105 micelles (NanoDeliv)..... | 26 |
| 3.1.3. Preparation of PEO-b-poly(NIPAAm-co-HEMA-lactate _n) micelles (PNHL)..... | 27 |
| 3.1.4. Conjugating Pluronic P105 to folic acid..... | 27 |
| 3.2. Methods..... | 28 |
| 3.2.1. Chamber design. | 28 |
| 3.2.2. Chamber data analysis. | 29 |
| 3.2.3. Kinetic modeling of drug release..... | 30 |
| 3.2.4. Model dependent methods. | 34 |
| Chapter 4. Results | 40 |
| 4.1. Comparison of Release from Folated and non-Folated Micelles | 40 |
| 4.2. Drug Release Percentage for Different Cases | 42 |
| 4.3. Kinetic Modeling of Drug Release..... | 45 |
| 4.3.1. Zero-Order model | 45 |

| | |
|---|----|
| 4.3.2. First-Order model..... | 48 |
| 4.3.3. Higuchi model..... | 51 |
| 4.3.4. Hixson-Crowell model..... | 55 |
| 4.3.5. Korsmeyer-Peppas model (the Power-Law model)..... | 58 |
| 4.3.6. Weibull model..... | 62 |
| 4.3.7. Baker–Lonsdale model | 65 |
| 4.3.8. The Hopfenberg model. | 67 |
| 4.4. Data Fitting..... | 69 |
| 4.5. Release Constant (k) Dependence on Power Density and Temperature. | 70 |
| 4.5.1. Release constant dependence on power density. | 70 |
| 4.5.2. The release constant dependence on temperature. | 75 |
| Chapter 5. Conclusion..... | 77 |
| Reference..... | 78 |
| Vita..... | 87 |

List of Figures

| | |
|--|----|
| Figure 1.1: The Most Common Cancers Worldwide [5]. | 14 |
| Figure 1.2: Statistical Percentages of Cancer Patients in each Gender [5]. | 14 |
| Figure 2.1: Micelles Structure [21]. | 18 |
| Figure 2.2: How Micellization occurs and CMC Effect [23]. | 19 |
| Figure 2.3: Passive Targeting [28]. | 20 |
| Figure 2.4: Active Targeting [28]. | 21 |
| Figure 2.5: Ultrasonic Bubble Formation [37]. | 25 |
| Figure 3.1: Example for One Release Pulse of Folated Micelles at 5.91 W/cm ² [52]. | 29 |
| Figure 4.1: Percent release of DOX from folated (PF) and non-folated micelles (POH) as a function of acoustic power density at 80 kHz. | 40 |
| Figure 4.2: Percent release of DOX from folated (PF) and non-folated micelles (POH) as a function of the mechanical index. | 42 |
| Figure 4.3: Percent release for drug released from non-stabilized P105 micelles (POH) at three different temperatures (25°C, 37°C, 56°C), in addition to the drug release percent from stabilized micelles (PNHL and NanoDeliv). | 44 |
| Figure 4.4: The fit of experimental data to the zero-order model for non-folated micelles DOX release at 3.54 W/cm ² power density | 47 |
| Figure 4.5: The fit of experimental data to the zero-order model for non-folated P105 micellar DOX release at 3.54 W/cm ² power density | 47 |
| Figure 4.6: The fit of experimental data to the first-order model for non-folated micelles DOX release at 3.54 W/cm ² power density | 50 |
| Figure 4.7: The fit of experimental data to the first-order model for folated micelles DOX release at 3.54 W/cm ² power density | 50 |
| Figure 4.8: Representation of drug concentration profile according to Higuchi model assumptions [91]. | 51 |
| Figure 4.9: The fit of experimental data to the Higuchi model for non-folated micelles DOX release at 3.54 W/cm ² power density | 54 |
| Figure 4.10: The fit of experimental data to the Higuchi model for folated micelles DOX release at 3.54 W/cm ² power density | 54 |
| Figure 4.11: The fit of experimental data to the Hixon-Crowell model for non-folated micelles DOX release at 3.54 W/cm ² power density | 57 |

| | |
|--|----|
| Figure 4.12: The fit of experimental data to the Hixon-Crowell model for folated micelles DOX release at 3.54 W/cm ² power density | 57 |
| Figure 4.13: The fit of experimental data to the Korsmeyer-Peppas model for DOX release from non-targeted micelles at a power density of 3.54 W/cm ² .. | 61 |
| Figure 4.14: The fit of experimental data to the Korsmeyer-Peppas model for DOX release from folated micelles at a power density of 3.54 W/cm ² | 61 |
| Figure 4.15: Example of a Percolation Fractal Embedded on a 2-dimensional Square Lattice, where the Exits are marked by a dark color, and gray for blocked areas [90]..... | 62 |
| Figure 4.16: The fit of experimental data to the Weibull model for DOX release from non-folated micelles at a power density of 3.54 W/cm ² | 64 |
| Figure 4.17: The fit of experimental data to the Weibull model for DOX release from folated micelles at a power density of 3.54 W/cm ² | 65 |
| Figure 4.18: The fit of experimental data to the Baker-Lonsdale model for DOX release from non-folated micelles at a power density of 3.54 W/cm ² | 66 |
| Figure 4.19: The fit of experimental data to the Baker-Lonsdale model for DOX release from folated micelles at a power density of 3.54 W/cm ² | 67 |
| Figure 4.20: The fit of experimental data to the Hopfenberg model for DOX release from non-folated micelles at a power density of 3.54 W/cm ² | 68 |
| Figure 4.21: The fit of experimental data to the Hopfenberg model for DOX release from folated micelles at a power density of 3.54 W/cm ² | 69 |
| Figure 4.22: Plot illustrating the activation power density required to release encapsulated DOX from micelles [52]. | 71 |
| Figure 4.23: Zero-order model plot used to find the acoustic activation power density for release from folated micelles | 71 |
| Figure 4.24: First-order model plot used to find the acoustic activation power density for release from folated micelles | 72 |
| Figure 4.25: Higuchi model plot used to find the acoustic activation power density for release from folated micelles | 72 |
| Figure 4.26: Hixon-Crowell model plot used to find the acoustic activation power density for release from folated micelles | 73 |
| Figure 4.27: Korsmeyer-Peppas model plot used to find the acoustic activation power density for release from folated micelles | 73 |

| | |
|---|----|
| Figure 4.28: Weibull model plot used to find the acoustic activation power density for release from folated micelles | 74 |
| Figure 4.29: Baker-Lonsdale model plot used to find the acoustic activation power density for release from folated micelles | 74 |
| Figure 4.30: Hopfenberg model plot used to find the acoustic activation power density for release from folated micelles | 75 |
| Figure 4.31: Plot illustrating the activation energy required to release encapsulated DOX from micelles [52]. | 76 |
| Figure 4.32: Plot used to find the activation energy for release from non-folated micelles for different temperatures | 76 |

List of Tables

| | |
|---|----|
| Table 3.1: Diffusional drug release from polymeric systems [75]. | 36 |
| Table 4.1: Heat map for %release data for both non-folated and folated micelles..... | 43 |
| Table 4.2: Key to Table 4.1 | 43 |
| Table 4.3: Heat map for data of different types of micelles and micelles at different temperatures at a power density of 0.76 W/cm ² | 45 |
| Table 4.4: Key to Table 4.3 | 45 |
| Table 4.5: The average of k values for non-folated for each model at six power densities. | 69 |
| Table 4.6: The average of R ² values for non-folated for each model at six power densities..... | 70 |
| Table 4.7: The average of k values for folated for each model at six power densities. | 70 |
| Table 4.8: The average of R ² values for folated for each model at six power densities. | 70 |
| Table 4.9: Values of PDa and A for each model | 75 |

Chapter 1. Introduction

1.1. Overview

Humans now live longer than ever, which is an excellent achievement in the 21st century, but they are also spending a larger portion of their lives being sick. Billions of bacteria, viruses, parasites, and fungi are trying to designate people as their hosts. These intruders can access human bodies through cuts, the GI tract, or other ways to enter the bloodstream of potential patients. As soon as these intruders gain access to the host, they start using the body's resources and doubling their numbers either in minutes, days, weeks, months, or even years. They move at first through the body without being detected by the immune system. Human bodies have developed this super-little army with guards, soldiers, intelligence, weapons factories, and communicators to protect people from dying.

Yet the threat does not always come from outside the human body; sometimes, the threat can come from an “error” that occurred in the human body. For example, cancer is one of the most threatening and incurable diseases if not treated at an early stage or in the right way. Mutations are the real culprit behind causing cancer, but what causes these abnormal mutations? There are three main factors that are responsible. The first is due to random errors that occur every time a cell divides and copies its DNA to make two new cells [1], [2]. This routine process happens millions of times every day in everyone's body and usually does no harm. However, cancers can occur when such errors affect an important gene rather than an unimportant gene [1], [2]. Mutations can also be caused by environmental factors [3]. To illustrate, some people increase the chance of developing mutations in their bodies by their risky behaviors, which include sunbathing or smoking. The third and final factor for mutation comes from the inheritance of a diseased gene [4]. The new faulty cells are stopped by the immune system, and they are either repaired or destroyed [1], [2], but occasionally these cells can find a way to slip past the immune system and multiply in a rapid and uncontrolled manner. These new cells can proliferate to form a lump or tumor [1], [2].

The Figures 1.1 and 1.2 show the following: First, the percent of most commonly diagnosed cancer types worldwide in 2018 and the percent of people diagnosed with cancer in each gender worldwide in the same year [5]. Cancer is seen

as an important issue that must be tackled and eliminated in the near future. This can only be done by looking for unconventional curing methods.

MOST COMMONLY DIAGNOSED CANCER TYPES

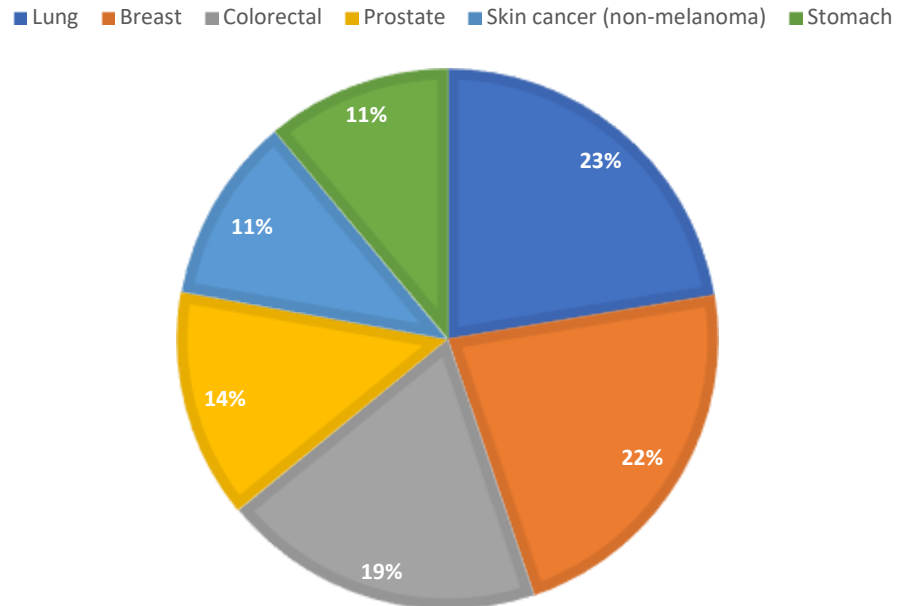


Figure 1.1: The Most Common Cancers Worldwide [5].

CANCER PATIENTS IN EACH GENDER

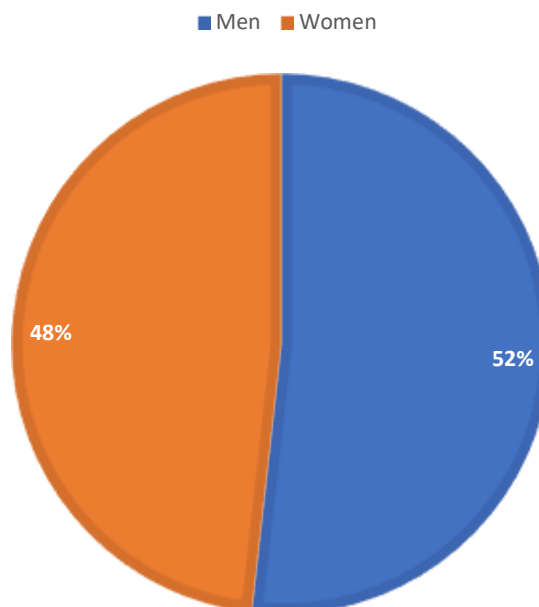


Figure 1.2: Statistical Percentages of Cancer Patients in each Gender [5]

The ancient Egyptians were the first to discover cancer as it was written in several papyri [1]. Yet, at that time, they believed that there was no cure for it. There are many ways to cure cancer today, either by surgical means, radiotherapy, chemotherapy, or by combining these methods. Many difficulties, however, stand in the way of full proof of cancer treatment. This is due to a variety of cancer types, as well as a lack of tumor selectivity [6]. Usually, in chemotherapy, known or conventional anticancer drugs have short circulation time in blood and disperse rapidly through the body. This results in a decrease in drug efficiency, and it is toxic to normal cells in the body [6]. In recent decades, however, scientists and engineers have begun to look for alternatives to overcome the above-mentioned issues.

“There’s plenty of room at the bottom,” a quote by Nobel prize winner in the field of physics Richard Feynman. The reason behind his quote is that he believed in the possibility of manipulating individual atoms that would enable people to have a better future. He said this sentence in the twentieth century, but now it is a reality with the introduction of nano-scale technologies. Nanotechnology can be defined as the ability to design, characterize, produce nanoscale (1-500 nm) materials, structures, devices, and systems and control their size and shape [7]. Nanomedicine is another important term to recognize. Nanomedicine is a subsection of nanotechnology where nanodevices and nanostructures are designed to monitor, repair, construct, and control human biological systems at a molecular level [6].

Hence, the introduction of drug delivery systems was imminent. Drug delivery systems (DDS) is a field that focuses on the use of nanoparticles (part of nanomedicine) such as liposomes, microcapsules, polymeric nanoparticles, and micelles to deliver and target diseased tissues for therapy [7]. To deliver and target these nanocarriers to tumor cells, they need to be designed in such a way that the drug is easily released. Here, arises the idea of stimuli-responsive drug delivery systems. This concept was first proposed in the late 1970s with the use of thermosensitive liposomes for the local release of drugs through hyperthermia [8], [9]. Stimuli-responsive nanocarriers are nano-sized delivery vehicles that have a unique structure. Their structure renders them more responsive to an external signal. There are various types of stimuli that can trigger drug release from these nanocarriers [8], [9]. These stimuli can be generally divided into internal (pH, glutathione, enzymes) and external (physical stimuli, i.e., heat, light, magnetic fields, and ultrasound) [8], [9]. There are two ways the drug is conjugated to

the nanocarriers: first is by encapsulating the drug inside the core of the nanocarrier, second is by linking the drug chemically to the nanocarrier surface [8]. Realizing which technique of conjugation is used will aid in determining which drug release stimuli to be utilized. In this thesis, the drug will be encapsulated inside the nanocarrier, and ultrasound will be used as external stimuli because it is non-invasive and can easily penetrate deep into the body.

1.2. Thesis Objectives

Due to the increasing number of people diagnosed with cancer and the high threat of anticancer drug intoxication to normal tissues, this thesis aims to propose a better, safer, and more efficient solution to these problems. This thesis focuses on studying the release of Dox from four different types of micelles targeted nanocarrier loaded with the anti-cancer drug Doxorubicin. In order to accomplish these aims, the following objectives were set:

- Studying the acoustic release of the chemotherapeutic drug Doxorubicin (DOX) from non-targeted micelles, folated micelles, micelles stabilized using an interpenetrating network of N,N-diethylacrylamide, and micelles formed using PEO-b-poly(NIPAAm-co-HEMA-lactate_n) using both 70-kHz and 80-kHz ultrasound at the following power densities: 0.76, 2.389, 2.546, 3.540, 5.013, 5.432, and 5.914 W/cm².
- Applying eight mathematical models to capture the kinetics of acoustic release from these nanocarriers. These models zero-order, first-order, Higuchi, Hixon-Crowell, Korsmeyer-Peppas, Weibull, Baker-Lonsdale, and Hopfenberg.
- Examining other effects that may have an impact on DOX release from the micelles, including temperature, power density, and micellar type.
- Using the Arrhenius equation to deduce the activation energy, and a modified Arrhenius equation to calculate an activation power density for this acoustic release phenomenon.

1.3. Thesis Organization

The remaining thesis is organized in the following manner: Chapter 2 provides a background on micelles, targeting schemes, targeting moieties, and ultrasound. The material and methods are discussed in Chapter 3. Chapter 4 discusses the results gained from experiments and mathematical modeling. Finally, chapter 5 is summarizing the thesis and outlines the major findings.

Chapter 2. Background and Literature Review

This chapter will discuss micelles, targeting schemes, targeting moieties, and ultrasound. A brief background is given on what micelles are, how they are formed, and what types are available. The chapter then details both passive and active targeted schemes. Subsequently, presenting targeting moieties studied in literature such as transferrin, aptamers, antibodies, peptides, and folic acid. A short description of what ultrasound is and how it functions. For the past 20 years, micelles and ultrasound have been investigated for the co-delivery of cancer drugs in vitro [9]–[15]. Also, In vitro and in vivo experiments have been reported, and results show promise for using micelles and ultrasound in cancer treatment [16]–[20].

2.1. Micelles

To design an effective DDS, the aforementioned nanoparticles must meet some criteria. These criteria include having a small size in the range of 1-500 nm, be able to biodegrade, have high drug loading capacity, be able to circulate in the body for longer times, and have the ability to accumulate in targeted areas [21]. Another factor the nanoparticles should overcome is multiple drug resistance (MDR). MDR is defined as the ability of cancer cells to withstand the different types of anticancer drugs. Several types of nanoparticle are capable of handling and overcoming all these problems, with micelles showing promise [21].

Block copolymers can be defined as macromolecules that have two or more different types of polymers that can be arranged by ring-opening polymerization or free-radical polymerization, —resulting in block copolymers with linear and/or radial arrangements. There are types of block copolymers that must be taken into account so that they are biocompatible and biodegradable [22]. For example, there are di-block copolymers or amphiphilic (hydrophilic-hydrophobic) like poly(ethylene glycol)-poly(ϵ - caprolactone), and there are tri-block copolymers (hydrophilic-hydrophobic-hydrophilic) like poly(ethylene oxide)-poly (propylene oxide)-poly(ethylene oxide) which are called *Pluronics* [22]. As shown in Figure 2.1, micelles have a structure of hydrophilic shell and a hydrophobic core formed through self-assembly), to reach a size that falls between 10 to 500 nm. Micelles are mainly suitable for two main reasons: they are able to transport the anticancer drugs through site-specific delivery, and they are easy to be engineered and manipulated for the drug and satisfy the delivery sites

specific needs [7]. Micelles consist of two main parts; the first is the hydrophobic core, where the hydrophobic drug is loaded inside and a hydrophilic shell that covers around the core, increasing the solubility of the drug. The hydrophilic shell is constructed from either poly(ethylene glycol) (PEG) or poly(ethylene oxide) (PEO) [22]. These polymers are inexpensive, have low toxicity, and protect the core from threats such as hydrolysis and enzymatic degradation. In addition, these polymers are capable of being unrecognized by the reticuloendothelial system (RES), thus, giving the micelles stealth properties. The core of a micelle can be made from poly(propylene oxide) (PPO), poly(L-lactide) (PLA) or any other hydrophobic polymer giving the micelle the ability to encapsulate the hydrophobic drug [22].

As mentioned earlier, micelles are the aggregation of block copolymers in aqueous solution. To elaborate more on how the self-assembly process occurs, an important term must be introduced: the critical micellar concentration (CMC). The CMC is defined as the minimum concentration needed for the polymer to form micelles [23]. Figure 2.2 represents how at low CMC levels, the block copolymers are both suspended in bulk solution and dispersed on the air-water interface [23]. As the polymer concentration increases, the system will reach the CMC. Further increase in the polymer concentration beyond the CMC level will result in initiating the formation of micelles in the bulk solution.

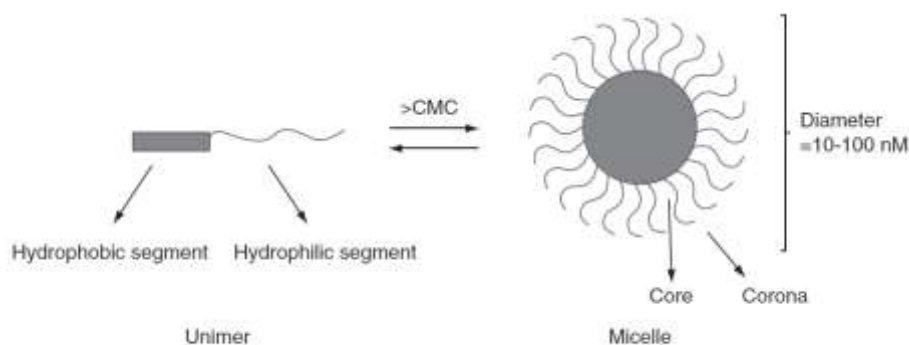


Figure 2.1: Micelles Structure [21].

2.2. Targeting Schemes

Many potential drugs do not reach the clinical trial phase due to their low water solubility, poor bioavailability, and severe side effects [24]. Yet encapsulating these drugs into nanocarriers such as micelles will improve their bioavailability and water solubility. In addition, it helps the drug to be isolated from the healthy body cells minimizing drug side effects, protecting the drug from degradation and controlling its

release, a phenomenon termed drug targeting. The aim of drug targeting is to deliver a high concentration of the drug directly to the tumor, accumulating, and then releasing the drug. This section will discuss the two types of targeting: passive and active targeting.

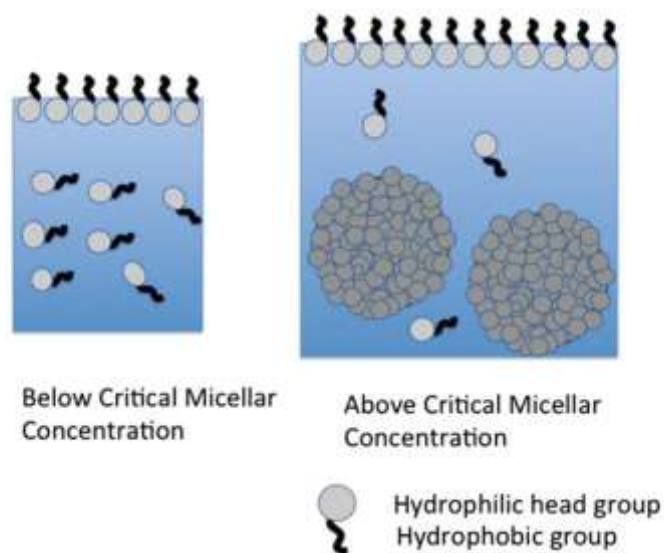


Figure 2.2: How Micellization occurs and CMC Effect [23].

2.2.1. Passive targeting. The passive targeting scheme is mainly dependent on the enhanced permeability and retention effect (EPR). The term angiogenesis means the process of rapidly forming and growing new blood vessels [22], [24]–[26]. Healthy tissues always go through this process, resulting in blood vessels with tight endothelial lining. While the tumor tissue exhibits a unique vasculature characterized by high permeability, meaning that the endothelial lining of the blood vessels has large gaps [22], [24]–[26]. As a result, the nanocarriers, when passing through the tumor blood vessels, are able to leave blood vessels to diffuse into interstitial spaces and deliver the drug [22], [24]–[26]. Furthermore, the tumor vasculature has low lymphatic drainage, which means that the nanocarriers delivering the drug can be retained (accumulate) inside the tumor tissue for treatment [22], [24]–[26]. The EPR effect will not be effective unless the drug nanocarriers (in this case micelles) are coated with a material that can protect it from being excluded by the reticuloendothelial system (RES), also as known as a mononuclear phagocytic system (MPS) [22], [24]–[26]. In earlier sections, poly(ethylene glycol) (PEG) and poly(ethylene oxide) (PEO) were used as coatings to nanocarriers giving them stealth properties. Having both of these conditions together will result in a DDS that passively targets the tumor.

Yet, this type of targeting has limitations: its inability to distinguish between healthy and tumor cells and having an insufficient concentration in tumor areas. Figure 2.3 gives a detailed representation of the passive targeting process.

2.2.2. Active targeting. Active targeting was developed to help in overcoming the limitations of passive targeting. Active targeting is mainly dependent on the over-expression of markers or receptors on the tumor cells, e.g., folate and transferrin [22], [25], [27]. Moreover, due to having these markers, nanocarriers (in this case, micelles) are chemically conjugated with targeting moieties that enable them to bind with the over-expressed markers [22], [25], [27]. Figure 2.4 represents the process of active targeting. There are many types of targeting moieties that can be chemically conjugated to the micelles, such as folate, transferrin, aptamers, antibodies, and peptides [22], [25], [27].

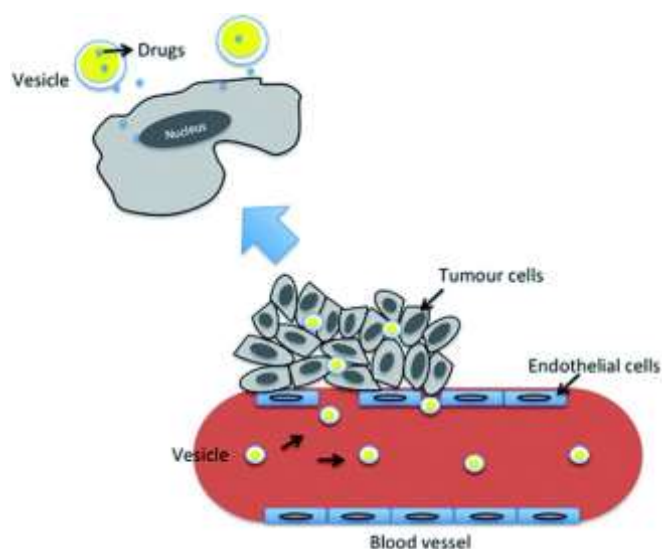


Figure 2.3: Passive Targeting [28].

2.3. Targeting Moieties

Active targeting of cancer cells helps in attacking the cells specifically through site-specific attachment. These attachments are conjugated on the surface of micelles, and they bind to the specific receptors on the cancer cell, are internalized, and release the drug they encapsulate. They are helpful in the reduction of potentially toxic side effects on healthy normal tissues. The moieties in this report are ligands that include transferrin, aptamers, antibodies, small molecules (Folic Acid), and peptides. To choose the correct ligand, three important conditions must be met: first is that the targeted

antigen or receptor must be in high density covering tumor cells, second is that the receptor can respond to endocytosis, and finally, it is immunogenetic [22]

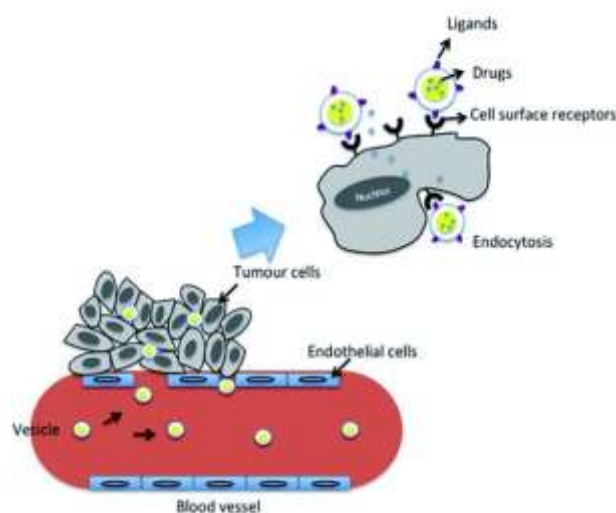


Figure 2.4: Active Targeting [28].

2.3.1. Transferrin. Transferrin is 80-kDa glycoprotein that is produced by the liver and is responsible for the transportation and regulation of iron in the cells. The process goes as follows, as soon as the transferrin molecule binds to the transferrin receptors (TFR) located on the cell surface, the transferrin is endocytosed into acidic compartments in the cell, i.e., endosomes and lysosomes [26]–[28]. The iron attached to the transferrin start dissociating, and the dissociated transferrin is being recycled back and released from the cell [26], [27]. The transferrin receptors are overexpressed on the cancer cells, and it gives an indication of the malignancy of the tumor [28]. This process caught the eye of researchers in the field of anticancer therapeutics as an option for targeted delivery via nanoparticles (NPs). As an example, Sahoo and colleagues developed a nanoparticle composed of copolymerized PLGA and poly (vinyl alcohol) (PVA) conjugated with transferrin on the surface (NPs-Tf) in order to enhance the therapeutic efficiency of paclitaxel a chemotherapeutic drug. The results showed that (NPs-Tf) could inhibit both cellular proliferation and tumor growth while sustaining both good release profiles and an increase in cellular uptake. Moreover, a comparison was made to illustrate how the free paclitaxel has reduced cellular proliferation by only 20%, while the conjugated NPs reduced it by 70% [29]. To sum up, transferrin shows a promising future in the field of ligand-mediated targeting.

2.3.2. Aptamers. Aptamers are another class of ligands or moieties that, in recent decades, caught the attention of researchers due to its high affinity and specificity. They are short, small (15-kDa), and single-stranded oligonucleotides of both DNA and RNA, which can fold in different conformations giving it the ability to ligand bind [22], [27], [30], [31]. Yet, there is a difficulty in forming aptamers because finding the right sequence that can both fold and be able to engage in ligand binding is not an easy task and is time-consuming. Researchers in 1990s developed a new technique to aid them in examining large numbers of both RNA and DNA sequences in order to get aptamers to act as targeting ligands. This new technique is called SELEX or systematic evolution of ligand by exponential amplification [22], [27], [30], [31]. This ligand has been studied extensively through the years as it shows great results in targeted delivery. To illustrate, many prostate cancer cells overexpress on their surface a prostate-specific membrane antigen (PSMA). Dhar et al. conjugated a nanoparticle carrier made of poly(D,L-lactic co-glycolic acid) and poly(ethylene glycol) with PSMA aptamer and loading with cisplatin in a prostate platinum-based chemotherapeutic drug. Cisplatin has the ability to interfere with DNA transcription [32]. Their results showed that the encapsulated drug is 80 times more toxic to prostate cancer cells when compared to administering free cisplatin [32].

2.3.3. Antibodies. Antibodies are large Y-shaped glycoprotein. They are like aptamers in terms of binding to the surface of nanoparticles and targeting specific antigens present on the cell membrane. Initially, utilizing antibodies had two main limitations. The first is being that antibodies were derived from mice resulting in immune response from the human body and leading to limited effectiveness and duration for the treatment to take effect [9], [15]. The second limitation was related to the lack of specificity of antibodies for targeting antigen sites [22], [27], [30], [31], [33]. Eventually, as modern technology is developing, these limitations were overcome by having antibodies derived from murine proteins [9], [15], [22]. These proteins are being manipulated to have high specificity for targeting sites and to provoke any human immune system response [22], [27], [33]. As an illustration, the epidermal growth factor receptor EGFR can be seen overexpressed in many cancer types. This receptor can bind to two different ligands: transforming growth factor-alpha and epidermal growth factor [34]. As soon as these ligands bind to EGFR, they stimulate both cell growth and the rapid proliferation of cells. Accordingly, blocking the ligand-receptor interaction will

reduce both cell growth and proliferation [34]. In order for this to occur, antibodies are utilized to interfere with that interaction. Russell et al. conjugated anti-EGFR antibodies to nanoparticles and loaded them with cisplatin and DOX. The results showed an increase by tenfold in the eradicating efficiency of the tumor [34].

2.3.4. Peptides. Peptides are made from amino acids, which can have either linear or cyclic shapes. Peptides are short sequences of up to 40 amino acids connected by amide bonds [9], [15], [19], [24]. Their small molecular size enables them to have a simple three-dimensional structure resulting in much higher stability and resilience to the surrounding environment. Furthermore, they are easy to synthesize and conjugate, making them less expensive to manufacture [27], [30]. In order to produce them, phage display is utilized as a screening tool that helps in detecting peptide sequences with high affinities to specified targets. For example, RGD (arginine-glycine-aspartic acid), comes from large functional proteins (derived from sequence of extracellular matrix) which are fibronectin, fibrinogen, laminin and collagen [31], [33], [35]. The main reasoning behind using RGD is that it inhibits the angiogenesis in solid tumors by binding to $\alpha_3\beta_v$ and $\alpha_5\beta_v$ integrins that are over-expressed during tumor formation [28]. Nasongkla et al. conjugated polymeric micelles with RGD on the surface and loading into it DOX [36]. The nanoparticles were made of poly(ϵ -caprolactone)(PCL)-poly(ethylene glycol) (PEG). These particles were introduced to Kaposi's sarcoma-derived cells, and it showed a thirty-fold increase in cellular uptake when compared to non-functionalized polymeric micelles [36].

2.3.5. Folic acid. Folic acid is considered one of the small molecules that can be conjugated to nanoparticles for targeted drug delivery. Since it is a small molecule, it has two main advantages; low manufacturing cost and high stability [26], [27], [30]. With these advantages, the pre-formulation conjugation is simple, and it gives more flexibility to be able to tune and synthesize conjugated nanoparticles. Folic acid, known as vitamin B9, is widely utilized due to its high affinity ($K_D \sim 10^9$ M) and high specificity towards folate receptors (FR) [22], [35]. These folate receptors are 38 kDa glucosyl-phosphatidylinositol-anchored glycoprotein, which is overexpressed on many types of cancer tumors such as ovarian, brain, breast lung, colon, and renal [28]. This receptor lets in particles conjugated with folic acid to be internalized and introduced into the cytoplasm [31], [33]. This ability caught the eye of researchers, thus they started experimenting with this moiety. Yoo and his colleagues created a copolymer made from

poly(D,L-lactic-co-glycolic acid) (PLGA), PEG conjugated with folic acid [37]. This polymeric micelle was loaded with DOX and tested for both its cardiotoxicity and cytotoxicity and compared the results with free DOX [37]. Their results illustrated a decrease in cardiotoxicity, an increase in cellular uptake, and increase in circulation time. This meant that these polymeric micelles are able to differentiate between healthy and tumor tissues and the ability of folic receptors to introduce the particles to the cytoplasm in an easier manner [37].

2.4. Ultrasound

Simply ultrasound consists of sound waves with a frequency above 20 kHz, which is inaudible to the human ears. There are many fields in medicine that utilize ultrasound technology such as imaging, lithotripsy, ultrasound sound Doppler, tissue ablation, and transdermal drug delivery. Ultrasound, when compared to other external stimuli, is advantageous due to the ability to focus them in a specified region in a non-invasive way and can be controlled remotely. Ultrasound can be categorized into two main sections: low frequency (the range is between 20-200 kHz) and high frequency (the range is > 200 kHz) [8], [38]. Each of these categories has its advantages and disadvantages. For low-frequency ultrasound, it can penetrate deeper into the body and have a lower attenuation constant [8], [38]. However, it falls short because it can generate strong cavitation effects, and the longer the wavelength, the harder it is to focus the waves. As a result, exposing human tissues to low-frequency ultrasound will cause the destruction of healthy and vital tissues by ultrasonic cavitation [8], [38]. On the other hand, utilizing high-frequency ultrasound shows a more promising future since the high intensity of the wave is concentrated in a small area only. Thus, there is no damage occurring to nearby tissue other than the focused area. However, the cavitation in high-frequency ultrasound is weak, which imposes difficulty in disrupting micelles [8]. In order to solve this issue, an ultrasound sensitive copolymer is designed.

Ultrasound has two main effects, thermal and cavitation effects. For the thermal effect, it does not have a high impact like cavitation, but it must be taken into consideration. When using high-frequency ultrasound, the attenuation is much higher than low frequency. Therefore, the high frequency cannot penetrate deep enough into the body but can convert the high attenuation energy into heat [8], [38]. This results in a good thermal effect. In terms of cavitation effects, Figure 2.5 shows how the

ultrasonic wave goes through the liquid environment to form microbubbles that expand in size and collapse in a concise duration of time.

The cavitation effects can be divided into two main phenomena: inertial cavitation and stable cavitation [8]. Inertial cavitation occurs when microbubbles form and oscillate in an unstable manner, expanding two or three folds their resonant size

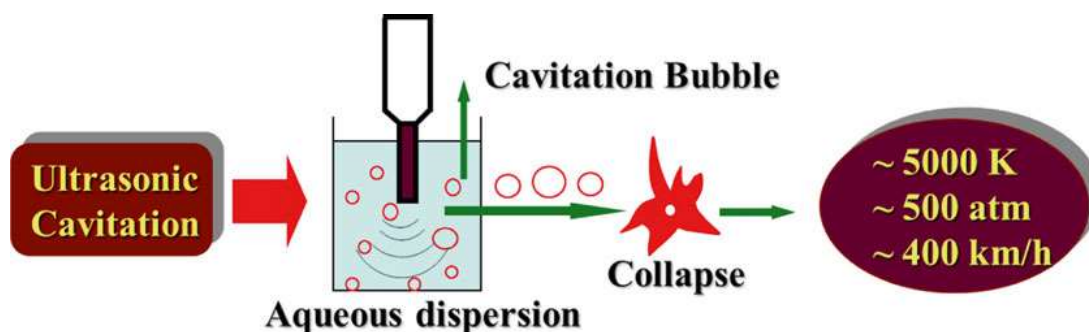


Figure 2.5: Ultrasonic Bubble Formation [37].

and finally collapsing violently [8]. While in stable cavitation, the microbubble can withstand expansion and compression forces for longer acoustic cycles having the diameter of the bubble vary around equilibrium diameter and finally bursting [8]. To sum up, regarding the cavitation effects, the focus will be towards the inertial cavitation as a major mechanism for disrupting polymeric micelles. Several papers have been published that combine liposomes [39]–[42], nanocarrier conjugated with targeted moieties with ultrasound [43]–[49]. In this work, the use of acoustic power in conjunction with DOX-loaded micelles will be modeled [50].

Chapter 3. Materials and Methods

This section shall discuss the proposed materials and methods that are going to be used to fulfill the thesis objectives. The first part of this section will tackle the preparation methods for different chemical reagents that are used in this paper. The chapter will begin with the method for preparing Pluronic P105 (non-stabilized micelles) stock solutions [51]. Then, the preparation method for P105 micelles stabilized using an interpenetrating network of N,N-diethylacrylamide (NanoDelivTM) and micelles formed by PEO-b-poly(NIPAAm-co-HEMA-lactate_n) (PNHL) [51]. Finally, the method for conjugating of Pluronic (P105) and folic acid (FA) [52], [53]. The second part from this section will briefly illustrate the design of the setup used to run the experiments and how to measure the kinetics of acoustically activated drug release from micelles [52], [53]. Third part from this section will extensively discuss the modeling of the acoustic release from different types of micelles this was achieved using mechanistic models, stochastic models, and statistical models which are used for treating the results as it will be shown again in the next chapter [51], [53]–[65]. Finally, a short explanation about the mechanical index and its significance [66].

3.1. Materials

3.1.1. Preparation of pluronic P105 (non-stabilized micelles). The preparation of Pluronic (BASF, Mount Olive, NJ) stock solutions by dissolving P105 in phosphate-buffered saline (PBS) to reach a final concentration of 10wt%. Then we will be adding DOX to the P105 solutions at room temperature to have a solution with a final DOX concentration of 10 µg/ml in 10wt% Pluronic. Also, the drug is dissolved in PBS to have the same concentration as earlier steps [9].

3.1.2. Preparation of stabilized P105 micelles (NanoDeliv). Now going on to the next major step, which will be forming the interpenetrating network of poly-N,N-diethylacrylamide (poly-NNDEA) in Pluronic P105 micelles, the next steps are applied [15]. The initial step involves adding a 40 ml aliquot of double distilled water that contains 10 wt% P105 to a round-bottom flask. NNDEA monomer will then be introduced to the flask to get a final concentration of 0.05wt% monomer. After that, N,N-bis(acryoyl)cystamine (BAC) was added as a cross-linking agent to get BAC:NNDEA mole ratio of 1:20. 2,2'-azobis(isobutyronitrile) (AIBN) has been added as an initiator to have AIBN: NNDEA mole ratio of 1:100.

Next, the flask was attached to a water condenser and purged with nitrogen with no heat for at least one hour. The system is then allowed to polymerize for 24 hours at a temperature of 65°C with continuous magnetic stirring and nitrogen purging. Then, the DOX stock solution was introduced to the resulting NanoDeliv at ambient room temperature to attain a final concentration of 10 µg/ml.

3.1.3. Preparation of PEO-b-poly(NIPAAm-co-HEMA-lactate_n) micelles (PNHL). The first step is to synthesize oligolactate esters of 2-hydroxyethyl methacrylate (HEMA-lactate_n) (n= the number of lactate units in a oligolactate). This process is completed by the ring-opening oligomerization of lactide utilizing HEMA as an initiator and stannous octoate as a catalyst [54]. In summary, the formed mixture was subsequently stirred at a temperature of 110°C under nitrogen purging up until the lactide was molten. Afterward, a catalytic amount of stannous octoate was dissolved in toluene and later introduced to the mixture in a dropwise manner. The mixture was then left to react for one hour. The final pursued stoichiometry was 3 or 5 lactate units per HEMA. The next step is the incorporation of polyethylene oxide (PEO) into the block copolymer by synthesizing the PEO macroinitiator, which is done in two steps. First, 4,4'-azobis(4-cyanopentanoic acid) was treated with SOCl₂ for 20 minutes at a temperature of 100°C to finally convert it to the corresponding acid chloride: 4,4'-azobis(4-cyanopentanoyl chloride) (ABCPC). Second, the PEO macroinitiator was prepared via a condensation reaction of ABCPC and PEO in dry dichloromethane in the presence of an excess amount of triethylamine and left for 24 hours [54]. Radical polymerization was used to synthesize PEO-b-poly(NIPAAm-co-HEMA-lactate_n) from NIPAAm combined with HEMA-lactate_n, which was obtained earlier using the PEO macroinitiator. The copolymerization process was performed at a temperature of 80°C for 24 hours in a nitrogen atmosphere. Later, the solution was allowed to cool down to ambient room temperature and concentrated it at reduced pressure. This newly formed solid was later dissolved in distilled water to obtain a solution with a concentration of 100 mg/ml. After that, centrifuged the solution for 30 minutes (10,000 rpm, Eppendorf 5415C) at a temperature of 40°C to separate unreacted PEO. Finally, the precipitated copolymer products have been dried under reduced pressure conditions.

3.1.4. Conjugating pluronic P105 to folic acid. The synthesis of P105-FA was done using 1,1-carbonyldiimidazole (CDI, Sigma Aldrich) [67]. Around 1.03g folic acid (Sigma Aldrich) was added in 100 ml of dried DMSO. Approximately

0.410g CDI was later added and set aside to react at ambient room temperature for 4 hours under dark conditions. For the FA activated solution mentioned above, around 30.0g of Pluronic P105 (BASF), which had been dried overnight under vacuum conditions, has been added to this solution. This solution was left to react in darkness and at ambient room temperature for 20 hours. By the end of the reaction, the solution was dialyzed for two days against DMSO and another two days against DD-water. Then, this purified product has been lyophilized and stored at a temperature of -20°C . An NMR spectra test was done to confirm the formation of P105-FA. This test confirmed P105-FA formation as it demonstrated a broad peak at 3.7 ppm (which is expected due to PEG being the backbone) and characteristic peak at 2.3, 6.6, 7.6, and 8.6 ppm which is due to FA conjugation. In the release experiment, a solution was prepared from phosphate-buffered saline (PBS) and P105-FA, having a concentration of 5.0 wt%. Later, DOX was added with micelles and mixed at ambient room temperature, reaching a final concentration of 10 $\mu\text{g/ml}$. The product solution was degassed overnight. A brook haven instrument (Model BI-DSI) equipped with particular specifications for this experiment was used to measure the hydrodynamic diameter of micelles which was found to be 10.2 ± 0.2 nm [52], [53].

3.2. Methods

3.2.1. Chamber design. A custom chamber was designed to measure the fluorescence variation and, therefore, DOX release caused by ultrasound. In order to split a beam of argon ion laser (Ion Laser Technology, Model 5500 A), a metal-film neutral density attenuator beam splitter is mounted. Thus, the beam was split into two portions. A portion of the split beam was guided to a photodetector (utilized for monitoring the laser power), the other portion of the beam was fed into the fiber optic bundle [52], [53]. The drug's concentration is quantified by measuring fluorescence emissions, which is generated by a specific excitation wavelength of 488 nm. Transmission of excitation light to the sample and capturing fluorescence emissions both are carried out by using a fiber-optic probe (which is made of 100 bundled multimode fiber, each one is around 40 cm in length). The light emitted was channeled through a dielectric Band-Pass filter (omega optical model 535DF35) and followed by a silicon photodetector (ZG&G450-1). The filter's purpose is to block any emissions that are generated below 517 nm, among them Rayleigh-scattered laser light.

To store and process the information, the fluorescence measurements were digitized. Finally, the Ultrasound Exposure Chamber temperature was set to 37 °C and maintained using a thermostat-controlled bath in order to mimic physiological conditions [52], [53].

3.2.2. Chamber data analysis. The aim of the chamber mentioned earlier was to measure the kinetics of acoustically activated drug release from micelles. The fluorescence of DOX decreased significantly when the encapsulated drug was released from the hydrophobic core of the micelles into the surrounding aqueous solution. Consequently, this indication helps in measuring the change in fluorescence intensity when ultrasound is applied. Figure 3.1 illustrates an example of a release pulse at 5.91 Watt/cm². The blue line in the Figure explains three main regions of a pulse: the first region corresponds to the fluorescence intensity of DOX before applying ultrasound (I_{PF}), the second region shows the intensity when the ultrasound is applied (I_{US}), and the last region shows the fluorescence intensity when the ultrasound is turned off (I_{PF}). The orange flat profile line below the pulse curve is corresponding to the fluorescence intensity of DOX (I_{PBS}) coupled with PBS and representing a 100% release of DOX into water. Moreover, the Figure also gives an insight into fast re-encapsulation that occurs when ultrasound is switched off. This insight indicated that a reduction in the interaction between the chemotherapeutic drug and normal tissue since the released drug is re-encapsulated back into nanocarriers when diffusing away from the sonicated volume [52], [53].

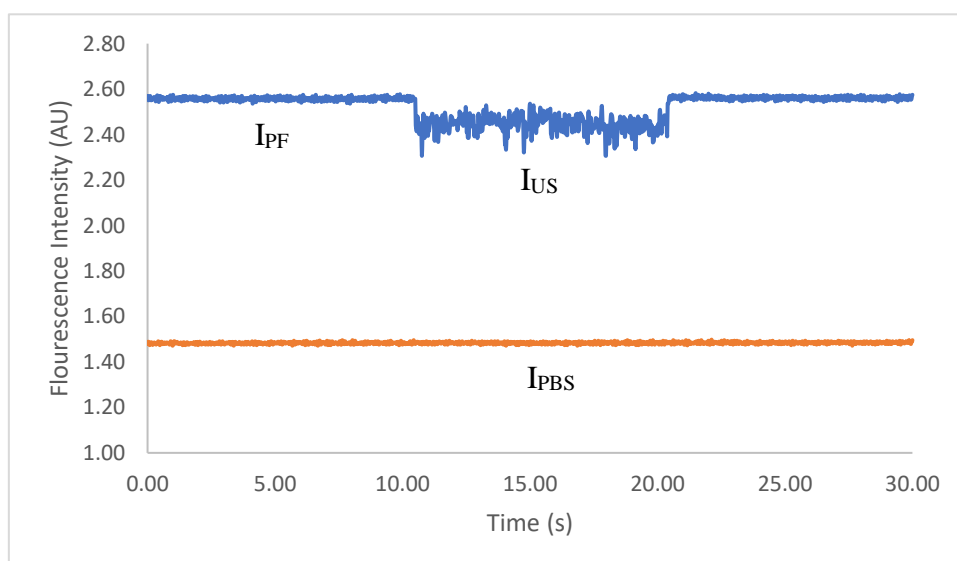


Figure 3.1: Example for One Release Pulse of Folated Micelles at 5.91 W/cm² [52].

The release experiments were conducted using 10 ml of the micellar DOX in a thin plastic tube and adding it to the bath at 37 °C, then applying 70-kHz ultrasound and recording the fluorescence level. As a result, to calculate the percentage release of the anti-neoplastic agent from these nanocarriers, the fluorescence intensities are used in the equation (1), where I_{PI05} is the initial intensity when the drug is encapsulated inside the micelles, I_{US} is the intensity when the ultrasound is applied, and I_{PBS} is the intensity of DOX in PBS. It represents 100% release (where all DOX molecules are interacting with water molecules [52], [53]).

$$\% \textit{release} = \frac{I_{PF} - I_{US}}{I_{PF} - I_{PBS}} \times 100\% \quad (1)$$

3.2.3. Kinetic modeling of drug release. In recent years, significant progress has been made in the field of drug delivery. These developments include advancements in mathematical/numerical modeling that aids in providing accurate estimates of the composition, dimensions and geometry, required drug dosage, and drug release profiles. Such developments may reduce the time needed for experimentation as well as decreasing the cost. The developed mathematical models often take into consideration the chemical, physical and biological aspects leading to a greater understanding of the processes underlying drug release, which will, in turn, further improve the safety of the developed products.

Takeru Higuchi led to the first scientific event that had a significant impact on the advancement of the drug delivery field, which started with his groundbreaking publication in 1961 [68]. Higuchi, a professor at the Universities of Wisconsin and Kansas, was the first pharmaceutical scientist to implement the principles of physical chemistry to the design of controlled release devices [68]. His famous equation calculating drug release from thin ointment film was the first stepping stone in the advancement of mathematical modeling of drug delivery systems [68], [69]. After that, more scientists proposed and derived various models, differing in accuracy and complexity, including both empirical/semi-empirical and mechanistic-realistic models. The distinction between the two is that the mathematical treatment of the former is strictly descriptive; it is not dependent on physical, chemical, or biological phenomena. As a result, the predictive ability of these models may be lower than the mechanistic models. Mechanistic-realistic models, on the other hand, are established on well-known

scientific phenomena such as dissolution, diffusion, precipitation, and swelling. The findings drawn from such models allow for the determination of system-specific parameters and the impact that these parameters have on the resultant drug release kinetics. Thus, in product development, the required composition, shape, size, and preparation technique of a novel treatment, with the desired properties, become theoretically predictable [69], [70]. The following factors should be considered when designing and/or using mathematical models for quantifying drug release [69]:

- 1- The first factor is concerned with the increase in the model complexity, which will enhance the accuracy of the mathematical theory. Thus, more physical, chemical, or biological phenomena should be taken into consideration to make the theory more realistic. Yet, having complex models will need more system-specific parameters making it cumbersome and difficult to gain quantitative predictions. Consequently, in developing a new mathematical theory for a specific drug delivery system, caution must be paid to consider dominant physical, chemical, and/or biological processes that affect the process to strike a balance between the accuracy and usability. For instance, if several mass transfer processes are occurring sequentially, take the slowest process (or the rate-limiting step) to consider in the model.
- 2- The second factor is dealing with the comparison between theoretical calculations and experimental results. There are two different types of comparisons that can be applied: the first involves the physical theory at play being fitted to experimental data, and the second involves directly comparing the theoretical predictions to independent experimental results. In the first situation, the model parameters are optimized in a manner to narrow the gap between experimental results and theoretical calculations. In the second situation, involves the comparison between independent experimental results and theoretical predictions, which will make the results more reliable. The reason for this is that system-specific parameters are calculated by fitting various sets of experimental results. Once all required model parameters have been calculated, it will be possible to predict the effects of different formulations and/or processing parameters on the properties of the system. Finally, the

respective formulations/devices are prepared, and the properties of the predicted systems are measured experimentally.

- 3- The last factor reveals that there is no standard mathematical theory that can be generalized to drug delivery systems of all nanocarrier and triggering techniques. Some models may only apply to a very small number of drug delivery systems, while others have a wider range of applications.

Based on the drug(s) type, incorporated drug dosage(s), the preparation technique, the geometry and dimensions of the drug delivery system, and Based on the drug(s) type, incorporated drug dosage(s), the preparation technique, the geometry and dimensions of the drug delivery scheme, and environmental conditions surrounding the system during drug release, any or more of the below phenomena may be involved in controlling the drug release [57], [69]: wetting the surface of the system, water penetrating through pores and/or continuous polymeric network, excipient and/or drug degradation, creation of water-filled pores, alterations in the geometry and/or dimensions of the systems under investigation, etc. Thus, mathematical models are being developed each in a different manner to satisfy the delivery system by considering the involvement of various specifications of the phenomena involved. It should be noted that most current modes simplify the overly complicated human body into one large well-stirred liquid tank. Also, some biological processes are typically not taken into consideration in developing pharmacokinetic models, including enzymatic degradation, intracellular drug transport, interactions with compounds in the extra- and intracellular space, drainage into the lymphatic system, transport across the blood-brain barrier (BBB) and other such complications. As a recommendation, these events are to be considered to get more holistic and realistic mathematical models [57], [69].

Regarding dissolution phenomena, the study of drug release kinetics is regulated by three main theories: first is the diffusion layer model (film theory), second Danckwert's model (surface renewal theory), and finally, the double barrier theory. The diffusion layer model comprises of two steps: the first step is the dissolution of the solid forming a stagnant film that is saturated with the drug, the second step includes the diffusion of the solubilized drug from the stagnant layer into the bulk of the solution; this step is the rate-determining step

in the process [56]. The equations (3.2) and (3.3) are representing the mathematical model of the diffusion layer model [55], [70], [71]:

- 1- The Noyes–Whitney equation, which was developed in the early 20th century, explains the solid dissolution process. Fick’s second law of diffusion is the foundation of this equation. Other assumptions include: the system particle having a spherical shape, the diffusion boundary thickness is constant, the diffusion boundary thickness is independent of particle size, and the drug dissolves uniformly. The equation shown below is the mathematical interpretation of the Noyes-Whitney equation:

$$\frac{dm}{dt} = kS(C_s - C) \quad (2)$$

In this equation, the variable m represents the amount of mass transferred per unit time t . This is achieved by the dissolution from the solid particle of instantaneous surface S , and k is a constant. The driving force for the dissolution process is displayed in the equation with the concentration gradient $(C_s - C)$. C stands for the concentration at a specific time, while C_s represents the equilibrium solubility of the solute. dm/dt referred to as the rate of the dissolution, which indicates the amount dissolved per unit area per unit time, and it has the units of $g/cm^2 \cdot s$. Once C concentration is 15% less than saturated solubility C_s , C would be deemed to have a negligible influence on the solid dissolution rate. For this instance, the solid dissolution is considered to be occurring under sink conditions. Furthermore, the surface area is considered only to be constant when the material amount present exceeds the saturation solubility, or at the very beginning of the experiments when a small quantity of the drug is dissolved.

- 2- The Nernst–Brunner equation is a modification to Noyes–Whitney equation where they used Fick’s first law of the diffusion in order to establish a relation between the constant k demonstrated in the equation (2) earlier and the solute diffusion coefficient resulting in the equation presented below [70]:

$$k = \frac{DS}{h\gamma} \quad (3)$$

The variable D is the diffusion coefficient, S is the surface area for the dissolving surface or diffusion layer area, γ is the volume of the solution, and h is the thickness of the diffusion layer. As Nernst and Brunner were formulating the equation, they assumed that the process occurring at the surface is faster compared to the transport process, and a linear concentration gradient is enclosed within the layer of the solution that is adhering to the solid surface.

In the case of Danckwert's model, it modifies the diffusion layer model by considering the packets that are present in the agitating fluid. The solute is absorbed by these packets or eddies at the solid-liquid interface and then transported into the bulk of the solution. The double barrier theory, on the other hand, proposes that an intermediate concentration will exist at the solid-liquid interface that comes from solvation, which is a function of solubility instead of diffusion.

Next, I will introduce the methods for investigating the kinetics of drug release from controlled-release dosage for medications, which are classified into three main categories: statistical methods, model-dependent methods (which is the focus in this thesis), and finally model-independent methods [51], [53], [62]–[65], [54]–[61].

3.2.4. Model dependent methods. Model-dependent methods have been developed by utilizing various mathematical representations that describe the dissolution/release profile of a drug delivery system [73]–[80]. After selecting a suitable function, model parameters are utilized to determine the dissolution profile. Deciding on a suitable function is generally achieved using non-linear regression analysis. Non-linear regression is a type of statistical analysis where observational data are added into a function that nonlinearly combines model parameters and depends on one or more independent variables [70], [81].

3.2.4.1. Zero-order kinetics. Zero-order kinetics explains the dosage forms that are difficult to disaggregate and exhibit slow drug release. Equation (4) illustrated below represents zero-order kinetics [70]:

$$Q_0 - Q_t = k_0 t \quad (4)$$

Q_o as shown in the equation is the initial amount of drug in the solution (in most cases $Q_o=0$), Q_t indicates the amount of drug dissolved at any given time t and k_o is the zero-order kinetics constant that has the units of concentration/time. The pharmaceutical dosage forms that are based on this profile release the same amount of drug per unit time and are thus ideal for attaining prolonged pharmacological action [82]. Studying systems that follow zero-order release kinetics requires plotting the cumulative amount of drug released versus time. This relation describes the dissolution of several types of modified dosage forms in addition to transdermal systems, osmotic systems, and matrix tablets with low solubility drugs [70].

3.2.4.2. First order kinetics. Gibaldi and Feldman were among the first who suggested applying this model for drug dissolution in 1967 and then Wagner in 1969. This model could also be expanded to explain the absorption and/or elimination of several drugs, but this mechanism is rather difficult to conceptualize theoretically [69]. The first-order drug release kinetics are shown in equation (5) [70]:

$$\frac{dc}{dt} = -kC \quad (5)$$

k stands for the first-order rate constant with units of time^{-1} . The data is plotted as the log of cumulative percentage of the remaining drug versus time, yielding a straight line that has a slope of $-k/2.303$. The equation is usually linearized to yield:

$$\log(C) = \log(C_o) - \frac{kt}{2.303} \quad (6)$$

Here C is the amount of drug release at any given time t , C_o is the initial concentration of the drug, and as previously mentioned k is the first-order rate constant.

3.2.4.3. Hixon-Crowell model. The objective of developing this model is to have the ability to explain or describe the release for systems under the assumption of variable surface area and diameter. Hixon and Crowell identified that the particle's shrinking area is directly proportional to the cubic root of its volume. Thus, they derived an equation that described the rate of dissolution depending on the cubic root of the weight of the particles [69], [70]:

$$W_o^{\frac{1}{3}} - W_t^{\frac{1}{3}} = \kappa t \quad (7)$$

Here W_o is the initial amount of drug in the pharmaceutical dosage form, W_t is the remaining amount of drug in the pharmaceutical dosage form at any given time t and κ is the constant that incorporates the surface–volume relation [70].

3.2.4.4. Korsmeyer-Peppas model. The Korsmeyer-Peppas equation, better known as the power-law equation, is a widely used and quite simple to apply the model for explaining drug release from polymeric systems [69], [70]. The model is shown below in the following equation [69], [70]:

$$\frac{M_t}{M_\infty} = kt^n \quad (8)$$

Here M_t represents the absolute cumulative amount of drug released at any given time t , M_∞ is similar to M_t , but for infinite time, k is the constant that includes both the geometrical and structural characteristics of the system, and finally, n is the release exponent that specifies the drug release mechanism which is shown in Table 3.1 [69], [70].

Table 3.1: Diffusional drug release from polymeric systems [75].

| Release exponent (n) | | | Drug transport mechanism | Rate as a function of time |
|--------------------------|-------------------|---------------|--------------------------|----------------------------|
| Cylinder | Sphere | Thin film | | |
| 0.5 | 0.43 | 0.5 | Fickian diffusion | $t^{-0.5}$ |
| $0.45 < n < 0.89$ | $0.43 < n < 0.85$ | $0.5 < n < 1$ | Anomalous transport | t^{n-1} |
| 0.89 | 0.85 | 1 | Polymer swelling | Zero order release |

3.2.4.5. Higuchi model. Earlier, the Higuchi equation was introduced as the earliest mathematical quantifier of drug release. The famous square root of time published by Professor Higuchi was originally designed for simple thin-film geometry, but the model has been altered to incorporate other geometries and porous systems [70].

The key advantage of this equation is its simplicity; but, when employing the equation to controlled drug delivery systems, there are several assumptions that must be satisfied before we can use it [69]:

- The initial drug concentration in the system should be greater when compared to drug solubility.
- Drug diffusion only happens in one dimension (neglecting edge effects).
- The drug particle size should be far smaller than the film thickness.
- The carrier material should not dissolve or swell.

- The drug diffusivity is constant (is not dependent on time or position).
- Throughout the experiment, perfect sink conditions are maintained.

$$Q = A\sqrt{D(2C - C_s)C_s t} \quad (9)$$

Here Q represents the amount of drug release per unit time t per unit area A , C stands for the initial drug concentration, C_s is the drug solubility in the matrix, and the diffusion coefficient is represented as D .

Equation (9) can be modified to accommodate systems where the initial concentration is lower than solubility and drug release, in this instance, it occurs through system pores, the adjusted equation is shown below [70]:

$$Q = A \sqrt{\frac{D\delta}{\tau}(2C - \delta C_s)C_s t} \quad (10)$$

Here D again is the diffusion coefficient, δ represents the porosity of the system, τ is the tortuosity of the porous system, and Q , A , C_s , C , and t have the same definitions as mentioned previously.

3.2.4.6. Baker-Lonsdale model. The Baker-Lonsdale model is yet another modified equation of the Higuchi model that is used to explain the release of drugs from spherical matrices, as shown in the equation (11) [83]:

$$f_1 = \frac{3}{2} \left[1 - \left(1 - \frac{M_t}{M_\infty} \right)^{\frac{2}{3}} \right] - \frac{M_t}{M_\infty} = \frac{3D_m C_{ms}}{r_o^2 C_o} - t \quad (11)$$

Here M_t is the amount of drug released at any given time t and M_∞ is the amount of drug released at infinite time, C_{ms} stands for the drug solubility of the system, D_m represents the diffusion coefficient, r_o is the radius of the spherical matrix, and C_o represents the initial drug concentration in the matrix.

The equation can also be further modified to accommodate non-homogeneous matrices and matrices that include some fractures or capillaries, as shown in equation (12) [55]:

$$f_1 = \frac{3}{2} \left[1 - \left(1 - \frac{M_t}{M_\infty} \right)^{\frac{2}{3}} \right] - \frac{M_t}{M_\infty} = \frac{3D_f C_{fs} \varepsilon}{r_o^2 C_o \tau} - t \quad (12)$$

The D_f stands for the diffusion coefficient, C_{fs} represents the drug solubility of the liquid surrounding matrix, τ represents the tortuosity factor of the capillary system, and ε represents the matrix porosity.

The matrix porosity derives from the equation ($\varepsilon = \varepsilon_o + KC_o$) where ε_o represents the initial matrix porosity, K is the drug specific-volume. In the case of ε is too small and can be neglected, equation (12) can be written as [55]:

$$f_1 = \frac{3}{2} \left[1 - \left(1 - \frac{M_t}{M_\infty} \right)^{\frac{2}{3}} \right] - \frac{M_t}{M_\infty} = \frac{3D_f C_{fs} K}{r_o^2 \tau} t \quad (13)$$

For this case, K stands for the release constant, and it corresponds to the slope.

3.2.4.7. Weibull model. This model is an empirical equation representing the cumulative fractional drug release as a function of time which is shown in the equation (14) [57]:

$$\frac{M_t}{M_\infty} = 1 - \exp \left[\frac{-(t - t_{lag})^b}{t_{scale}} \right] \quad (14)$$

Here, t_{lag} is the lag time before drug release, t_{scale} stands for the time scale of the release process, and b characterizes the release curve shape. In the case of $b=1$ the resultant curve will be exponential; if $b>1$, the curve shape will be a sigmoid (S-shape) curve, and if $b<1$, the produced curve is going to be parabolic that has a high initial slope.

3.2.4.8. Hopfenberg model. The Hopfenberg model is a semi-empirical equation that was developed to explain the release of drugs from a degradable drug release system under the assumption that the overall release acts as a zero-order mechanism that is limited to the system's surface area.

This zero-order process can be the outcome of a single or combination of both physical and/or chemical phenomena that happened on the surface. This semi-empirical equation is thus suitable for quantifying the release of the drug from surface-eroding particles due to the fact that it is based on the assumption that the release rate is governed by the dissolution which occurs at the surface [57], [69], [70]:

$$\frac{M_t}{M_\infty} = 1 - \left[1 - \frac{t_{lag}}{C_L \alpha} \right]^n \quad (15)$$

C_L is the initial drug loading throughout the system, α is the systems half-thickness (i.e. the radius of either a sphere or a cylinder), and n represents an exponent that differs with geometry $n=1$ (flat), and $n=2$ (cylindrical), and $n=3$ (spherical).

3.2.4.9. The Mechanical Index and its significance. Ultrasound, as previously discussed, is a form of energy that is being generated by pressure waves, and its effects on living tissue are referred to as bioeffects. Two main bioeffects are observed when applying ultrasound: first is heating (thermal) effects, and second is mechanical (non-thermal) effects. There are two indices derived from the bioeffects: first is the thermal index (TI) and second is the mechanical index (MI), the focus of our discussion will solely be on the latter.

The mechanical index is a quantity that measures the likelihood that exposure to diagnostic ultrasound will cause an adverse biological effect (non-thermal mechanism) [66]. The mechanical index is defined, as shown in equation (16) [66]:

$$MI = \frac{P}{\sqrt{f}} \quad (16)$$

The P here represents the negative-peak pressure in units of (MPa), and f is the frequency in MHz. As seen in the equation, the relation between pressure and mechanical index is directly proportional, while the relation between the square root of frequency and mechanical index is indirectly proportional. In basic terms, the mechanical index is a method for measuring the power of the ultrasound beam applied.

One of the goals measuring the mechanical index is to find whether the system is operating under cavitation conditions and the type and threshold of cavitation [84]. The collapse cavitation threshold is the point at which the inertial cavitation starts to take place in the bubble [66].

Chapter 4. Results

4.1. Comparison of Release from Folated and non-Folated Micelles

A comparison between folated and non-folated micelles drug release is presented in Figure 4.1. The percentage of DOX release was measured at a frequency of 80 kHz as a function of ultrasound power density. The principle used to calculate the release percent is simple. Inside the core of the micelles, DOX fluorescence is considerably higher compared to its quenched fluorescence when exposed to an aqueous environment. The decrease in fluorescence as the DOX leaves the hydrophobic micellar environment and diffuses into the aqueous surroundings is used to calculate the percent drug release shown in Figure 4.1.

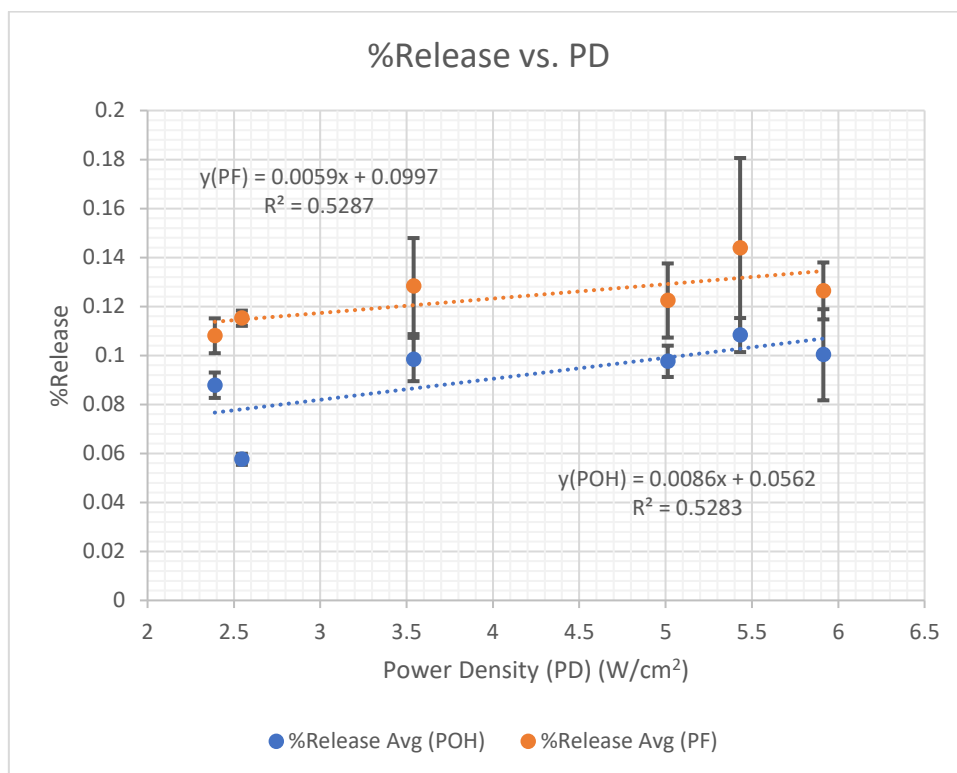


Figure 4.1: Percent release of DOX from folated (PF) and non-folated micelles (POH) as a function of acoustic power density at 80 kHz.

The figure summarizes the percentage release of the drug from both folated and non-folated micelles as a function of acoustic power density at 80 kHz. The release from non-folated micelles is always lower than the release from folated micelles. This may be due to the conjugation of the folate moiety, which renders the micelles more sensitive to ultrasound (sonosensitive), by reducing their stability. Furthermore, the plot

can be split into two separate regions that both folated and non-folated micelles follow. The first area demonstrates a nearly linear trend (increase in drug release with increasing power density) at power densities that are lower than 3.5 W/cm^2 for both the release from folated and non-folated micelles. In the second part of the plot, at power densities higher than 3.54 w/cm^2 , both non-folated and folated micelles are showing a reasonably constant trend.

Based on results shown in Figure 4.2, the mechanical indices corresponding to each power density, are all in the high inertial cavitation region. To realize the significance of this cavitation mode and its effect on drug release, the next paragraph will summarize how the drug is being released via the cavitation phenomenon at the different mechanical indices.

There are three different regions for the mechanical index values. The first case is low mechanical indices with values that range from below 0.3 and up to 0.6 (no inertial cavitation), while the second case involves medium mechanical indices, which ranges from 0.6 to 1.17 (transient inertial cavitation). Finally, the third case is high mechanical indices with values above 1.17 (high inertial cavitation) [85]. Each case will be described briefly as discussed by Boukaz et al. in their study that deals with enhancing the imaging quality of ultrasound and its relationship to the mechanical index. In their paper, Boukaz et al. argued that the mechanical index is important because it helps in identifying the power densities that are safe to operate ultrasound imaging machines without causing biological damage. We will begin with the case of low mechanical indices, at the corresponding power densities, the bubble will expand at a very slow rate and the drug inside the core of micelles will be released at a prolonged rate [85]. For the medium mechanical indices case, the bubbles are contracting and expanding at a faster rate compared to low mechanical indices, which causes the release of the drug from inside the micelles due to cavitating bubbles [85]. Finally, we direct our attention to the high mechanical index case, where the bubbles are expanding and contracting very rapidly, releasing the drug instantaneously with heat being generated in the process [85].

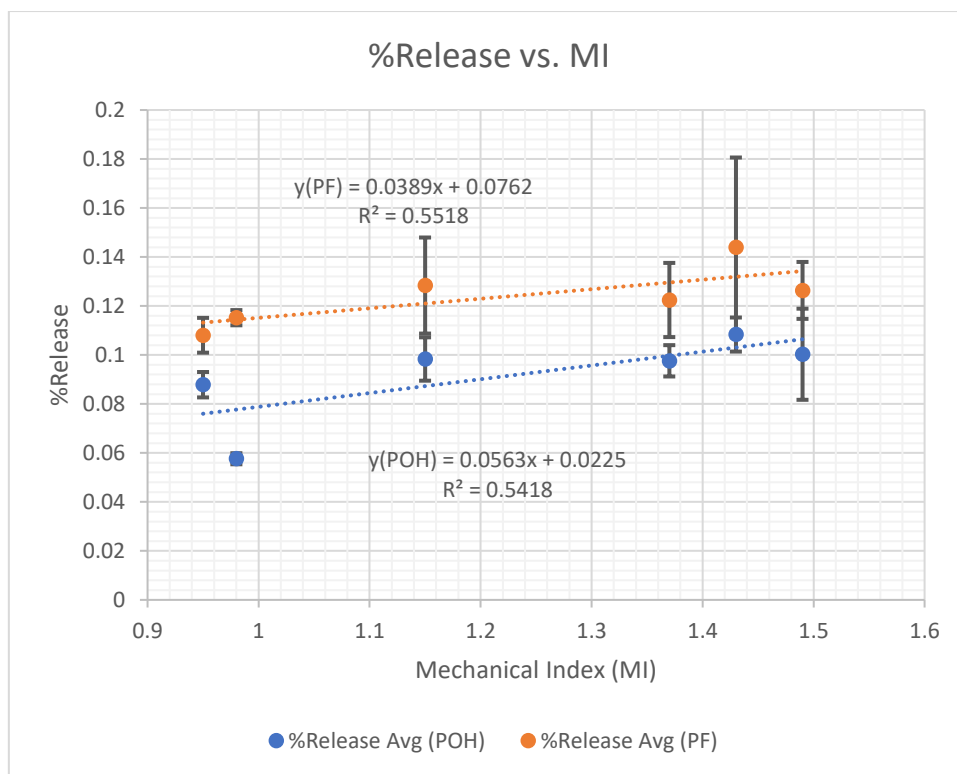


Figure 4.2: Percent release of DOX from folated (PF) and non-folated micelles (POH) as a function of the mechanical index.

This paper studied mechanical indices in the range of 0.95 and 1.49 as seen in Figure 4.2. The plot shows that as the mechanical index increased, so did drug release. This implies that more shear forces are applied to both folated and non-folated micelles, which is caused by an increase in cavitation.

A heat map was generated to show the statistical significance of measured acoustic data for both non-folated and folated micelles at different power densities. Table 4.1 shows that the acoustic release of DOX from non-folated micelles at a power density of 2.39 W/cm² was statistically significant compared to the release measured at 2.55 W/cm². The same analysis can be deduced for folated micelles release.

4.2. Drug Release Percentage for Different Cases

In this thesis, the percentage of drug release from three different micelles and at three different temperatures were studied [51], [54]. Figure 4.3 below shows the percentage of drug released from non-stabilized micelles (POH) at three different temperatures (25°C, 37°C, 56°C), in addition to the drug release percent from stabilized micelles (PNHL and NanoDeliv). These experiments were performed using 70-kHz ultrasound.

Table 4.1: Heat map for %release data for both non-folated and folated micelles.

| | POH (2.39W/cm ²) | POH (2.55W/cm ²) | POH (3.54W/cm ²) | POH (5.01W/cm ²) | POH (5.43W/cm ²) | POH (5.91W/cm ²) | PF (2.39W/cm ²) | PF (2.55W/cm ²) | PF (3.54W/cm ²) | PF (5.01W/cm ²) | PF (5.43W/cm ²) | PF (5.91W/cm ²) |
|---------------------------------|---------------------------------|---------------------------------|---------------------------------|---------------------------------|---------------------------------|---------------------------------|--------------------------------|--------------------------------|--------------------------------|--------------------------------|--------------------------------|--------------------------------|
| POH (2.39W/cm ²) | | 4.29E-06 | 3.63E-02 | 1.64E-02 | 2.39E-04 | 1.68E-01 | 2.70E-05 | 3.28E-06 | 3.16E-03 | 6.89E-05 | 3.41E-05 | 4.29E-08 |
| POH (2.55W/cm ²) | 4.29E-06 | | 5.18E-05 | 5.01E-06 | 2.48E-06 | 2.33E-03 | 1.68E-09 | 2.98E-11 | 2.78E-04 | 8.16E-07 | 2.71E-07 | 7.68E-11 |
| POH (3.54W/cm ²) | 3.63E-02 | 5.18E-05 | | 8.72E-01 | 5.64E-02 | 8.24E-01 | 5.10E-02 | 4.18E-03 | 1.13E-02 | 1.92E-03 | 3.09E-04 | 7.61E-05 |
| POH (5.01W/cm ²) | 1.64E-02 | 5.01E-06 | 8.72E-01 | | 1.96E-02 | 7.49E-01 | 1.23E-02 | 4.47E-04 | 1.05E-02 | 1.00E-03 | 2.40E-04 | 5.04E-06 |
| POH (5.43W/cm ²) | 2.39E-04 | 2.48E-06 | 5.64E-02 | 1.96E-02 | | 3.58E-01 | 9.38E-01 | 6.30E-02 | 5.50E-02 | 3.15E-02 | 2.38E-03 | 9.20E-04 |
| POH (5.91W/cm ²) | 1.68E-01 | 2.33E-03 | 8.24E-01 | 7.49E-01 | 3.58E-01 | | 3.68E-01 | 1.07E-01 | 2.93E-02 | 3.74E-02 | 2.17E-03 | 1.63E-02 |
| PF (2.39 W/cm ²) | 2.70E-05 | 1.68E-09 | 5.10E-02 | 1.23E-02 | 9.38E-01 | 3.68E-01 | | 2.08E-02 | 5.18E-02 | 2.49E-02 | 2.13E-03 | 2.89E-04 |
| PF (2.55 W/cm ²) | 3.28E-06 | 2.98E-11 | 4.18E-03 | 4.47E-04 | 6.30E-02 | 1.07E-01 | 2.08E-02 | | 1.63E-01 | 1.98E-01 | 9.28E-03 | 7.87E-03 |
| PF (3.54 W/cm ²) | 3.16E-03 | 2.78E-04 | 1.13E-02 | 1.05E-02 | 5.50E-02 | 2.93E-02 | 5.18E-02 | 1.63E-01 | | 5.48E-01 | 2.27E-01 | 8.25E-01 |
| PF (5.01 W/cm ²) | 6.89E-05 | 8.16E-07 | 1.92E-03 | 1.00E-03 | 3.15E-02 | 3.74E-02 | 2.49E-02 | 1.98E-01 | 5.48E-01 | | 5.94E-02 | 5.28E-01 |
| PF (5.43 W/cm ²) | 3.41E-05 | 2.71E-07 | 3.09E-04 | 2.40E-04 | 2.38E-03 | 2.17E-03 | 2.13E-03 | 9.28E-03 | 2.27E-01 | 5.94E-02 | | 9.88E-02 |
| PF (5.91 W/cm ²) | 4.29E-08 | 7.68E-11 | 7.61E-05 | 5.04E-06 | 9.20E-04 | 1.63E-02 | 2.89E-04 | 7.87E-03 | 8.25E-01 | 5.28E-01 | 9.88E-02 | |

Table 4.2: Key to Table 4.1

| | |
|-----|-----------------------|
| | P-value < 0.0001 |
| | 0.0001 <P-value<0.001 |
| | 0.001<P-value<0.01 |
| | 0.01<P-value<0.05 |
| | P-value>0.05 |
| POH | non-folated micelles |
| PF | folated micelles |

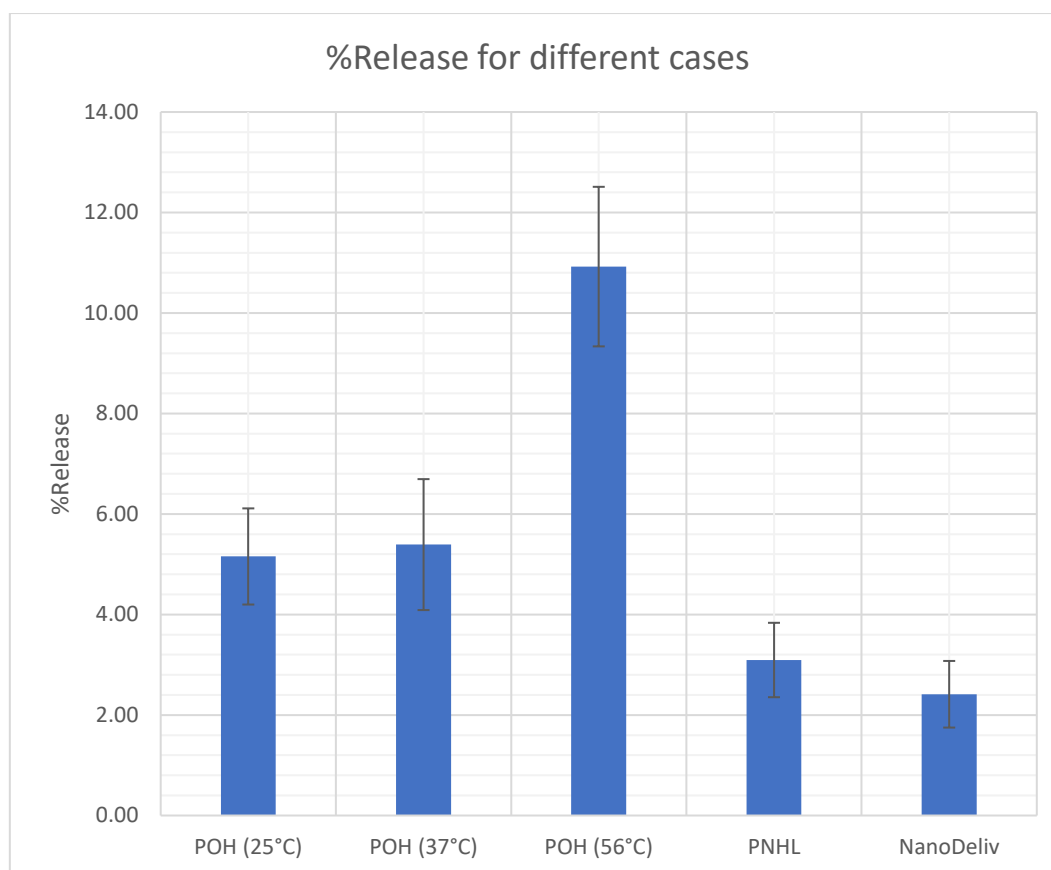


Figure 4.3: Percent release for drug released from non-stabilized P105 micelles (POH) at three different temperatures (25°C, 37°C, 56°C), in addition to the drug release percent from stabilized micelles (PNHL and NanoDeliv).

As illustrated in Figure 4.3, temperature influences the percentage of drug release, which means that as the temperature increases, the release percentage will also increase due to a decrease in micro-viscosity, making it easier to shear and release more drug molecules when ultrasound is applied. When comparing the percentage release of non-stabilized and stabilized (PNHL and NanoDeliv) at 37 °C, results show that the micellar stabilization mechanism (as discussed in sections 3.1.2 and 3.1.3) reduces DOX release. A heat map was generated to show the statistical significance of measured acoustic release from the different types of micelles, and non-stabilized micelles at different temperatures. Table 4.3 shows that acoustic release from PNHL micelles at a power density of 0.76 W/cm² was statistically higher compared to release from NanoDeliv micelles at a power density of 0.76 W/cm². Table 4.3 also shows that release from non-stabilized micelles at 25°C and 37°C was statistically insignificant. On the other hand, when comparing the statistical significance of release at 56°C vs. the other two temperatures, the difference is statistically significant.

Table 4.3: Heat map for data of different types of micelles and micelles at different temperatures at a power density of 0.76 W/cm²

| | POH (25°C) | POH (37°C) | POH (56°C) | PNHL | NanoDeliv |
|------------|------------|------------|-------------|-------------|-------------|
| POH (25°C) | | 0.27617114 | 0.000150724 | 3.4234E-06 | 7.5664E-07 |
| POH (37°C) | 0.27617114 | | 0.000566818 | 9.43755E-08 | 2.11743E-08 |
| POH (56°C) | 0.00015072 | 0.00056682 | | 4.75385E-07 | 3.06017E-07 |
| PNHL | 3.4234E-06 | 9.4376E-08 | 4.75385E-07 | | 0.034993649 |
| NanoDeliv | 7.5664E-07 | 2.1174E-08 | 3.06017E-07 | 0.034993649 | |

Table 4.4: Key to Table 4.3

| | |
|-----|--------------------------|
| | P-value < 0.0001 |
| | 0.0001 < P-value < 0.001 |
| | 0.001 < P-value < 0.01 |
| | 0.01 < P-value < 0.05 |
| | P-value > 0.05 |
| POH | non-folated micelles |

4.3. Kinetic Modeling of Drug Release.

The *Model-dependent methods* were discussed previously and addressed the importance of mathematical modeling in the field of drug delivery that can be used to simulate drug release kinetics. This section derives the kinetic models introduced in the previous chapter, along with the results of fitting these models to release [83], [86]–[89]. The concentration or amount (as the Cumulative Fraction Release drug released from micelles) will be denoted by the (CFR) (defined by equation (5)). To assess the fit of each model, the value of the coefficient of determination, R^2 , which will be acquired from the linearized version of the model equations, will be used to compare. The plots for both folated and non-folated micelles at 3.54 W/cm² for each model are presented after the model derivation, while the rest of the plots are supplied in the appendices.

4.3.1. Zero-Order model: The model assumes the following: First, the form in which the drug is delivered does not disaggregate, and second, the assumption is that a slow release of the drug is occurring. Hence, the amount of drug dissolved per unit time does not change.

- Model equation:

$[C]$ is similar to $Q(t)$ as previously mentioned in chapter 3 as the amount drug that is in solution at any given time t , the equation below hypothesizes exactly how the drug behaves in solution:

$$\frac{d[C]}{dt} = K_0 \quad (17)$$

K_0 is zero-order release constant, which has units of concentration per unit time.

- Model derivation:

- 1- First, we will integrate this differential equation by parts within the bounds of 0 and t , resulting in the equation below:

$$\int_{C_0}^{C_t} d[C] = \int_0^t K_0 dt \quad (18)$$

- 2- After the integration, the equations becomes:

$$C_t - C_0 = K_0(t - 0) \quad (19)$$

$$C_t = C_0 + K_0 t \quad (20)$$

Here C_t is the amount of drug released at any given time t , and C_0 is the initial amount of the drug in solution (generally it very small or equals to 0). Now comes the definition of Cumulative Fraction Released (CFR) that is shown in the equation below:

$$\begin{aligned} CFR &= \frac{\text{Drug released at any time, } t - \text{Initial Amount}}{\text{Total amount of drug present}} \\ &= \frac{C_t - C_0}{C_{Total}} \end{aligned} \quad (21)$$

C_{Total} stands for the total amount of the drug in the system.

- 3- Since C_0 equals zero because the drug is inside the micelles and not released at $t = 0$, the CFR will be modified as shown in the equation below:

$$CFR = \frac{C_t}{C_{Total}} \text{ or } C_t = CFR \times C_{Total} \quad (22)$$

- 4- Replacing C_t in equation (20) with C_t from equation (22), the result becomes:

$$CFR = \frac{K_0}{C_{Total}} t \quad (23)$$

- 5- Introducing the variable $k' = \frac{K_0}{C_{Total}}$, equation (23) will be rearranged, as shown below:

$$CFR = k't \quad (24)$$

It should be noted that **CFR** considers the initial amount of drug/response present within the system; thus, the plot must go through the origin. A plot of **CFR** vs. **Time** would give a straight line with **k'** as its slope. The plots for both non-folated and folated micelles at 3.54 W/cm² for zero-order model are presented in Figures 4.4 and 4.5.

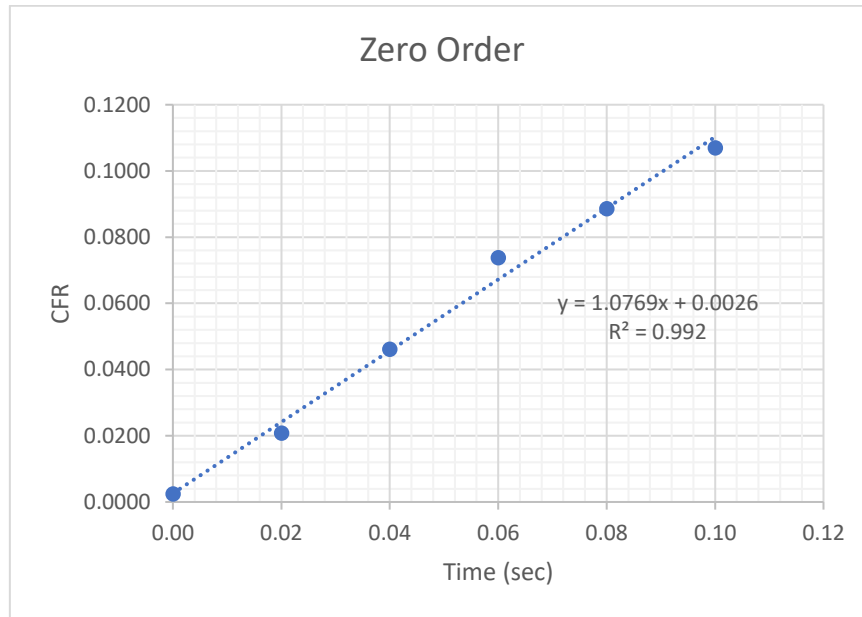


Figure 4.4: The fit of experimental data to the zero-order model for non-folated micelles DOX release at 3.54 W/cm² power density

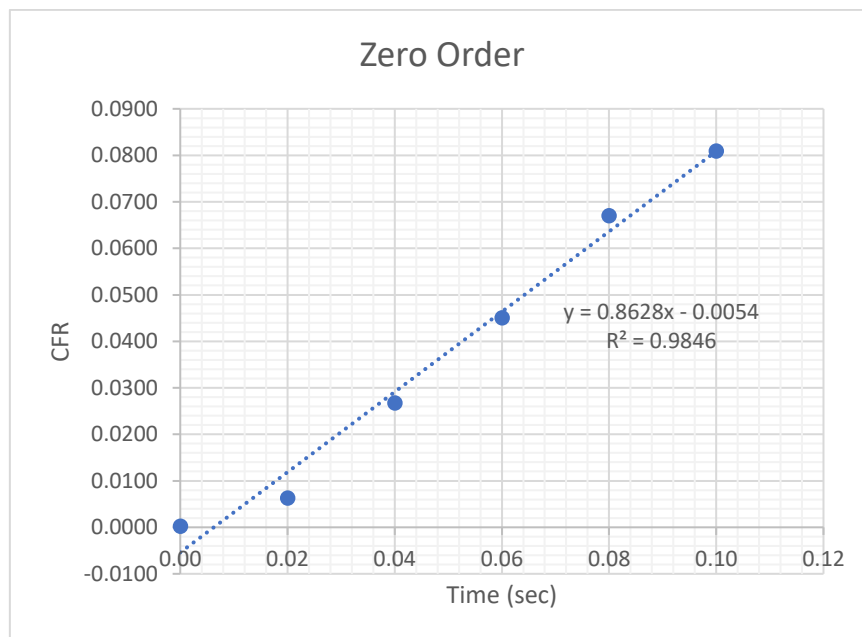


Figure 4.5: The fit of experimental data to the zero-order model for non-folated P105 micellar DOX release at 3.54 W/cm² power density

4.3.2. The First-Order model This model could be utilized to describe drug dissolution of pharmaceutical dosage forms in include water-soluble drugs encapsulated in porous matrices, and it can be expanded to explain the absorption and/or elimination of several drugs from the body. The first-order model follows the assumption that the change in the concentration of the drug in solution is not constant but is a function of the instantaneous concentration. This can be illustrated mathematically, as shown in the following equation:

$$\frac{d[C]}{dt} = -K[C] \quad (25)$$

$[C]$ represents the concentration of the drug in solution at any given time t , and K refers to the first-order release constant with units of time^{-1} . If we take the $[C]$ to be the concentration of the drug in solution, the minus sign in the equation becomes positive as the drug is released into the surrounding media of the nanoparticles. The new rearranged equation becomes:

$$\frac{d[C]}{dt} = K[C] \quad (26)$$

- Model derivation:

1- Integrating by parts between time 0 and t ,

$$\int_{C_0}^{C_t} \frac{d[C]}{[C]} = \int_0^t K dt \quad (27)$$

C_0 has the same definition as in the zero-order kinetic model, which is the initial drug concentration in the surrounding solution, and C_t is the concentration after any given time t . After integrating equation (27), the equation becomes:

$$\ln\left(\frac{C_t}{C_0}\right) = Kt \quad (28)$$

2- Taking the exponential of both sides of the equation yields

$$\frac{C_t}{C_0} = e^{Kt} \quad (29)$$

3- Both sides are then multiplied by C_0 to give,

$$C_t = C_0 e^{Kt} \quad (30)$$

- 4- We will subtract C_0 from both sides and from right side taking C_0 as a common factor,

$$C_t - C_0 = C_0(e^{Kt} - 1) \quad (31)$$

- 5- Once Again, we will use the same *CFR* definition we used in the previous zero-order model,

$$\begin{aligned} CFR &= \frac{\text{Drug released at any time, } t - \text{Initial Amount}}{\text{Total amount of drug present}} \\ &= \frac{C_t - C_0}{C_{Total}} \end{aligned} \quad (32)$$

C_{Total} signifies the total amount of the drug in the system.

- 6- Substituting $C_t - C_0$ using equations (31) and (32) gives,

$$CFR = \frac{C_t - C_0}{C_{Total}} = \frac{C_0(e^{Kt} - 1)}{C_{Total}} \quad (33)$$

Equation (33) is then linearized, but first C_0/C_T will be added to both sides of the equation, yielding

$$CFR + \frac{C_0}{C_{Total}} = \frac{C_0}{C_{Total}} e^{Kt} \quad (34)$$

- 7- Then, the natural logarithm of both sides of equation (37) are taken to yield,

$$\ln\left(CFR + \frac{C_0}{C_{Total}}\right) = \ln\left(\frac{C_0}{C_{Total}}\right) + Kt \quad (35)$$

Equation (35) is simplified by assuming that on the left side C_0/C_{Total} equals to zero when C_0 is negligible but the term $\ln(C_0/C_{Total})$ cannot be disregarded even if C_0 is negligible, as the logarithm of a small number can still have a substantial value. The plot will, therefore, always have a non-zero y-intercept as per equation (36),

$$\ln(CFR) = \ln\left(\frac{C_0}{C_{Total}}\right) + Kt \quad (36)$$

Therefore, plotting $\ln(CFR)$ versus time will give a straight-line graph with a slope of K and y-intercept of $\ln(C_0/C_{Total})$. The plots for both non-folated and folated micelles at 3.54 W/cm^2 for first-order model are presented in Figures 4.6 and 4.7.



Figure 4.6: The fit of experimental data to the first-order model for non-folated micelles DOX release at 3.54 W/cm^2 power density

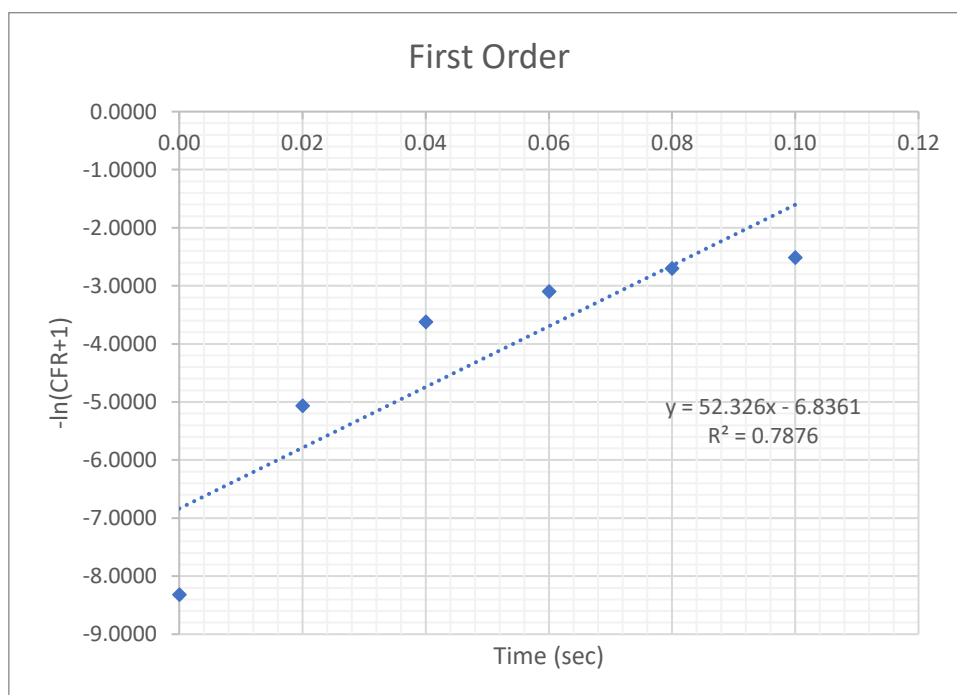


Figure 4.7: The fit of experimental data to the first-order model for folated micelles DOX release at 3.54 W/cm^2 power density

4.3.3. Higuchi model. The Higuchi model was the very first mathematical model derived to describe drug release from a matrix system. This model is designed to describe release from planar systems; but it has been altered and modified to consider other geometries and porous systems. As mentioned in section 3.2.4.5, the equation expressing the Higuchi model is based on the following assumptions (refer to Figure 4.8) [69], [90]:

- The initial drug concentration in the system should be higher compared to drug solubility.
- Drug diffusion only happens in one dimension (neglecting edge effects).
- The drug particle size should be far smaller than the film thickness.
- The carrier material should not dissolve or swell.
- The drug diffusivity is constant (is not dependent on time or position).
- Throughout the experiment, perfect sink conditions are maintained.

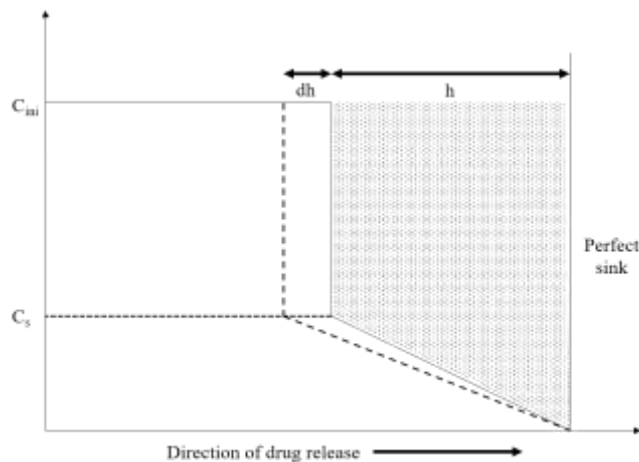


Figure 4.8: Representation of drug concentration profile according to Higuchi model assumptions [91].

- Model derivation:
 - 1- The mass/mole flux of the drug for the system in the above illustration can be defined as:

$$\frac{Q(t)}{A} = h \left(c_{micelles} - \frac{c_s}{2} \right) \quad (37)$$

Here $Q(t)$ refers to the amount of drug released at any given time t , A is the surface area of the DDS in contact with the medium, $c_{micelles}$ is the concentration of the drug inside the micelles (or any other DDS that is used),

and c_s stands for the solubility of the drug in the sink. In order to use this equation, the value of h , which is the distance from the DDS surface, must be known. The value for h , the drug-concentration-distance profile, in equation (37) can be calculated by taking infinitesimal time intervals of dt :

$$\frac{dQ}{A} = dh \left(c_{micelles} - \frac{c_s}{2} \right) \quad (38)$$

- 2- To determine the amount of the drug released after a time interval dt , Fick's 1st diffusion law is used as given in equation (39). Here D is the diffusion coefficient, dc is the differential of concentration, and dx is the differential of distance,

$$J = -D \frac{dc}{dx} = -D \left(\frac{-c_s}{h} \right) = \frac{1}{A} \frac{dQ}{dt} \quad (39)$$

- 3- Equation (39) can be algebraically manipulated to yield:

$$\frac{dQ}{A} = -D \left(\frac{-c_s}{h} \right) dt \quad (40)$$

- 4- Next, we will equate equation (40) to equation (38),

$$-D \left(\frac{-c_s}{h} \right) dt = dh \left(c_{micelles} - \frac{c_s}{2} \right) \quad (41)$$

- 5- By applying separation of variables, and integrating with the limits of 0 to t for time and distance from the surface, from 0 to h,

$$\int_0^t \frac{2Dc_s}{2c_{micelles} - c_s} dt = \int_0^h h dh \quad (42)$$

$$\frac{2Dc_s}{2c_{micelles} - c_s} t = \frac{h^2}{2} \quad (43)$$

$$h = 2 \sqrt{\frac{Dc_s t}{2c_{micelles} - c_s}} \quad (44)$$

- 6- Rearranging equation (37) to get an expression for h ,

$$h = \frac{Q}{A \left(c_{micelles} - \frac{c_s}{2} \right)} \quad (45)$$

7- Equating equation (44) to equation (45) and with some algebraic manipulation,

$$2 \sqrt{\frac{Dc_s t}{2c_{micelles} - c_s}} = \frac{2Q}{A(2c_{micelles} - c_s)} \quad (46)$$

$$Q = A \sqrt{Dc_s t} \frac{(2c_{micelles} - c_s)}{\sqrt{(2c_{micelles} - c_s)}} \quad (47)$$

$$Q = A \sqrt{Dc_s (2c_{micelles} - c_s) t} \quad (48)$$

In this classical Higuchi equation, the Higuchi constant, k_h , is taken to be

$$k_h = A \sqrt{Dc_s (2c_{micelles} - c_s)} \quad (49)$$

8- Taking the newly defined k_h and substituting it back into equation (48),

$$Q = k_h \sqrt{t} \quad (50)$$

9- Once Again, we will use the same *CFR* definition from the previous models,

$$\begin{aligned} CFR &= \frac{\text{Drug released at any time, } t - \text{Initial Amount}}{\text{Total amount of drug present}} \\ &= \frac{Q_t - Q_0}{Q_{Total}} \end{aligned} \quad (51)$$

10- To get a relationship between CFR and time will implement equation (51) as it was performed for previous models, and the following equation results:

$$CFR = \frac{Q - Q_0}{Q_{Total}} = \frac{k_h \sqrt{t}}{Q_{Total}} - \frac{Q_0}{Q_{Total}} \quad (52)$$

11- To simplify equation (52) will define a new term which is k'_h as follows:

$$k'_h = \frac{k_h}{Q_{Total}} \quad (53)$$

Now substituting equation (53), if $Q_0 = Q_{Total}$, we rearrange the equations to get:

$$CFR + 1 = k'_h \sqrt{t} \quad (54)$$

Consequently, if $CFR+1$ is plotted against the square root of time, a linear graph is obtained with a slope of k'_h . The plots for both non-folated and folated micelles at 3.54 W/cm² for the Higuchi model are presented in Figures 4.9 and 4.10. The values of

$CFR+1$ at time equal to zero are outliers. Hence, the plots for Higuchi's model only have five points rather than six points similar to other models.

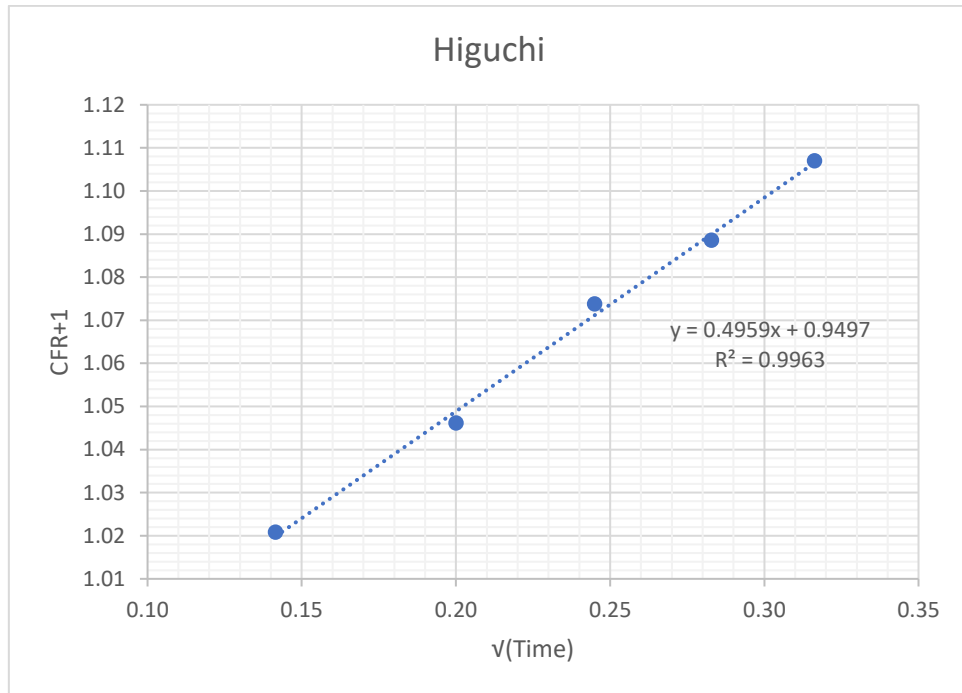


Figure 4.9: The fit of experimental data to the Higuchi model for non-folated micelles DOX release at 3.54 W/cm^2 power density

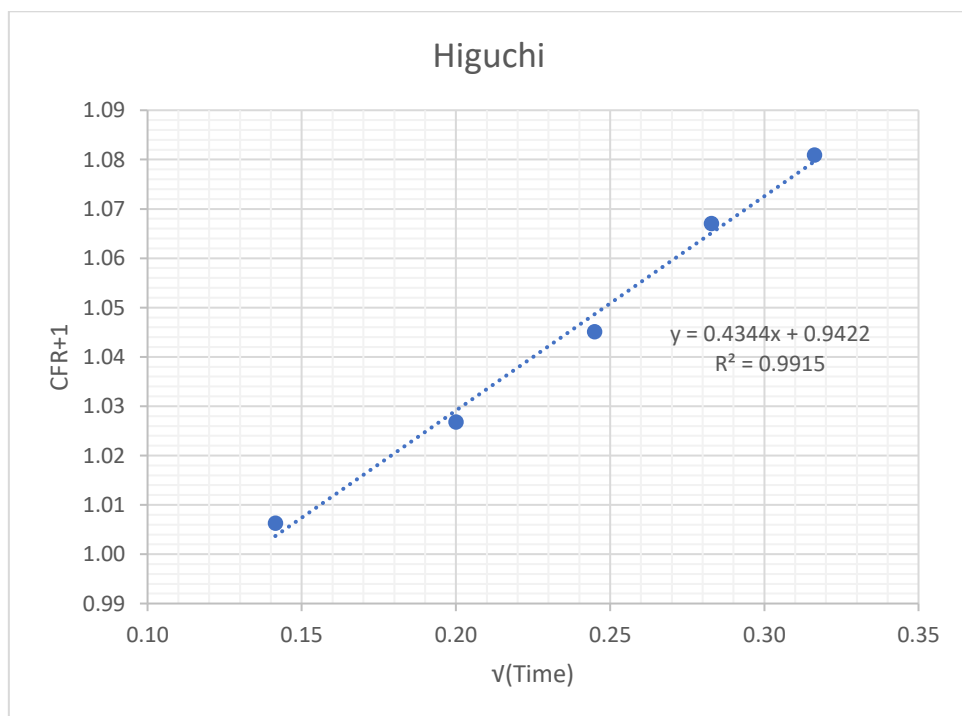


Figure 4.10: The fit of experimental data to the Higuchi model for folated micelles DOX release at 3.54 W/cm^2 power density

4.3.4. Hixson-Crowell model. This model follows the following assumptions: the dissolution occurs normal to the surface of the solute particles, agitation is uniform over the exposed surface, and the nanoparticles have a spherical shape.

- Model derivation:

- 1- Noyes-Whitney equation is a special form of Fick's law which is expressed in the equation below:

$$\frac{dW}{dt} = \frac{kA(C_s - C_\infty)}{l} \quad (55)$$

Where $\frac{dW}{dt}$ stands for rate of dissolution, k is the Noyes-Whitney constant and includes the diffusion constant D , A is the surface area, C_s refers to solute concentration, C_∞ represents the concentration of the bulk solution and is considered to be zero in this case, and l is the diffusion layer. By simplifying equation (55), we will get the following:

$$dW = kA \frac{(C_s)}{l} dt \quad (56)$$

- 2- The mass is expressed as follows, and a minus sign is added because the drug is being released or lost from the core of the nanocarriers,

$$dW = -\rho dV \quad (57)$$

- 3- Pluronic P105 micelles have a spherical shape; hence their volume can be expressed as (note that N is the number of spheres/nanocarriers):

$$V = \frac{4}{3}\pi r^3 N \quad (58)$$

$$A = \frac{dV}{dr} = 4\pi N r^2 \quad (59)$$

- 4- Then, we will combine equations (56) and (57) and substituting for the differential volume and the area will get the following:

$$dW = -\rho 4\pi N r^2 dr = \frac{k 4\pi N r^2 C_s dt}{l} \quad (60)$$

- 5- Canceling out similar terms and integrating on both sides,

$$\int_{r_o}^{r_t} -\rho dr = \frac{k C_s}{l} \int_0^t dt \quad (61)$$

$$-(r - r_o) = \frac{kC_s T}{\rho l} \quad (62)$$

$$r_t = -\frac{kC_s T}{\rho l} + r_o \quad (63)$$

6- In order to use our experimental data in the analysis (i.e., CFR), the weight of dissolution/release W will be used rather than the volume. First, equation (58) will be used to determine the volume for N spheres. Thus, the weight of each sphere can be expressed as:

$$W = \rho \frac{4}{3} \pi r^3 N \quad (64)$$

7- Now, we will raise all variables to the cubic root and rearranging for r to yield:

$$r = \frac{W^{\frac{1}{3}}}{\left(\rho \frac{4}{3} \pi N\right)^{\frac{1}{3}}} \quad (65)$$

8- By substituting r_o and r_t (equation (65)) into equation (63), we will obtain:

$$\frac{W_t^{\frac{1}{3}}}{\left(\rho \frac{4}{3} \pi N\right)^{\frac{1}{3}}} = -\frac{kC_s T}{\rho l} + \frac{W_o^{\frac{1}{3}}}{\left(\rho \frac{4}{3} \pi N\right)^{\frac{1}{3}}} \quad (66)$$

9- Simplifying the above equation into the Hixson-Crowell form, yields:

$$W_t^{\frac{1}{3}} = -\frac{kC_s T}{\rho l} \left(\rho \frac{4}{3} \pi N\right)^{\frac{1}{3}} + W_o^{\frac{1}{3}} \quad (67)$$

10- Now, we define K' as a constant related to the surface, the shape and the density of the particle and will get,

$$W_o^{\frac{1}{3}} - W_t^{\frac{1}{3}} = \frac{kK' C_s T}{l} (N)^{\frac{1}{3}} \quad (68)$$

11- Once Again, we will use the same CFR definition, we used for the zero-order and first-order models to obtain,

$$\begin{aligned} CFR &= \frac{\text{Drug released at any time, } t - \text{Initial Amount}}{\text{Total amount of drug present}} \\ &= \frac{C_t - C_0}{C_{Total}} = \frac{W_t - W_o}{W_o} \end{aligned} \quad (69)$$

12- By dividing both sides by W_o , applying equation (69), and then linearizing equation (68), we will obtain:

$$(1 - CFR)^{\frac{1}{3}} = K_{\beta} t \quad (70)$$

Here K_{β} stands for the release constant.

This model has been utilized to describe the release profile bearing in mind the diminishing surface of the micelles during dissolution/release. Plotting $(1 - CFR)^{\frac{1}{3}}$ against time t will yield a straight line that has a slope of K_{β} . The plots for both non-folated and folated micelles at 3.54 W/cm^2 for Hixon-Crowel model are presented in Figures 4.11 and 4.12.

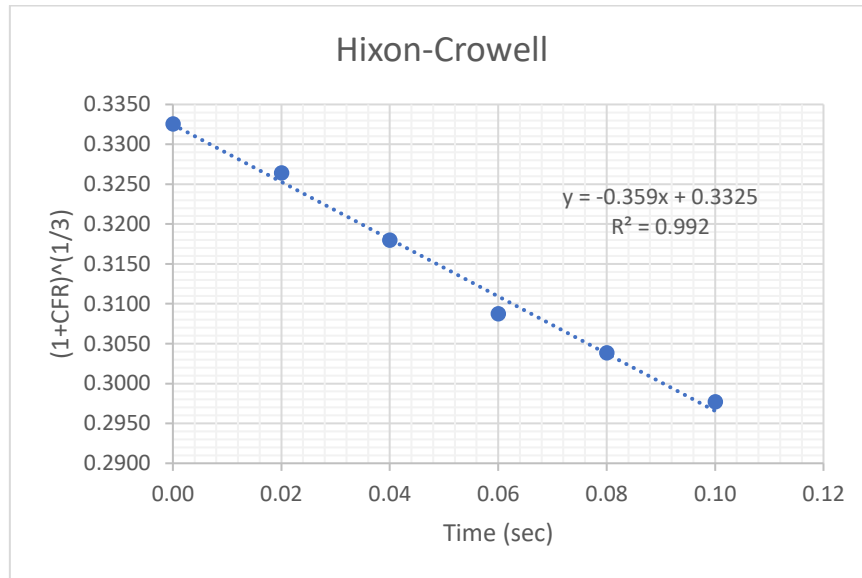


Figure 4.11: The fit of experimental data to the Hixon-Crowell model for non-folated micelles DOX release at 3.54 W/cm^2 power density

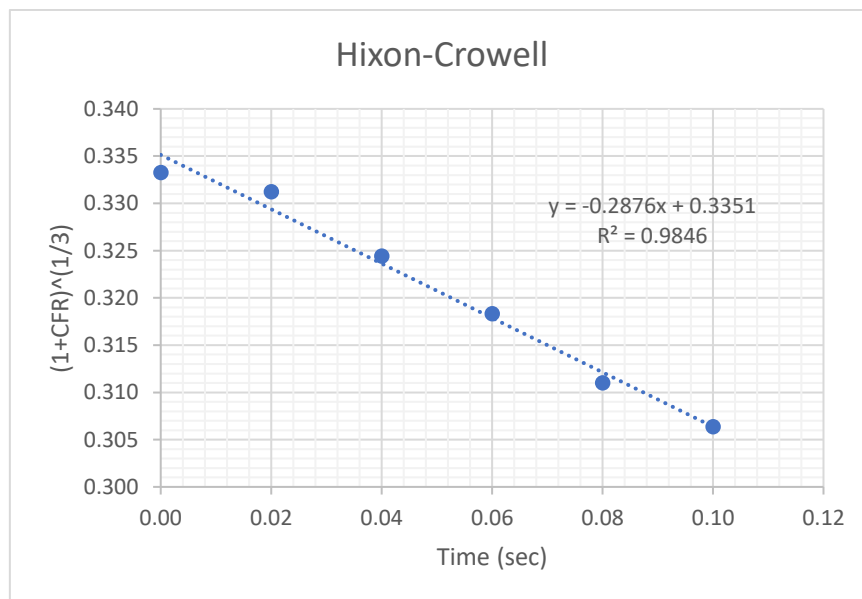


Figure 4.12: The fit of experimental data to the Hixon-Crowell model for folated micelles DOX release at 3.54 W/cm^2 power density

4.3.5. The Korsmeyer-Peppas model (the Power-Law model). Korsmeyer-Peppas model has the following simple form:

$$CFR \approx k_{kp} t^n \quad (71)$$

Here k_{kp} represents the constant in the model that describes and incorporates the structural and geometrical characteristics of the form of the DDS, and n refers to the release exponent that characterizes the drug release mechanism.

- Model derivation:

- 1- Starting from Fick's second law of diffusion, for diffusion from the controlled DDS, where concentration is represented by C in three-dimensional space (x , y , and z) and D is the diffusion coefficient,

$$\frac{\partial C}{\partial t} = D \left(\frac{\partial^2 C}{\partial x^2} + \frac{\partial^2 C}{\partial y^2} + \frac{\partial^2 C}{\partial z^2} \right) \quad (72)$$

- 2- Assuming that the diffusion of the drug is occurring in the x -direction only,

$$\frac{\partial C}{\partial t} = D \frac{\partial^2 C}{\partial x^2} \quad (73)$$

- 3- Equation (73) is a second-order partial differential equation that could be solved utilizing the error function, and numerical methods that were originally described and derived by Crank in 1975 [92].

To solve this differential equation for a non-steady state general boundary conditions, where the surface concentrations are assumed constant and the initial distribution within the DDS is given by a function of position, $f(x)$,

$$\begin{aligned} t \geq 0, \quad x = 0, \quad C &= C_1 \\ t \geq 0, \quad x = l, \quad C &= C_2 \\ t = 0, \quad 0 < x < l, \quad C &= f(x) \end{aligned}$$

- 4- Using the separation of variables method to solve the above partial differential equation, the general solution to equation (73) is found in the form of a trigonometric series:

$$\begin{aligned} C = C_1 + (C_2 - C_1) \frac{x}{l} + \frac{2}{\pi} \sum_1^{\infty} \frac{C_2 \cos(n\pi) - C_1}{n} \sin \frac{n\pi x}{l} e^{-\frac{Dn^2\pi^2 t}{l^2}} \\ + \frac{2}{l} \sum_1^{\infty} \sin \left(\frac{n\pi x}{l} \right) e^{-\frac{Dn^2\pi^2 t}{l^2}} \int_0^1 f(x') \sin \left(\frac{n\pi x'}{l} \right) dx' \end{aligned} \quad (74)$$

The boundary conditions for the case considered in this thesis are uniform initial distribution and equal surface concentrations:

$$\begin{aligned}
t = 0, \quad -\frac{l}{2} < x < \frac{l}{2}, \quad C = C_0 \\
t > 0, \quad x = \pm \frac{l}{2}, \quad C = C_1
\end{aligned}$$

The physical meaning behind these conditions indicates that initially, within the drug carrier, the concentration is uniformly the initial concentration of the drug, C_0 . After that, at any given time t , the concentration of the drug at the boundary between the DDS and the solution is equal and constant at C_1 . These conditions can be translated as *perfect sink* conditions, where the drug has an infinite sink to dissolve into, and the DDS is separated from the solution by a membrane (in our case, the thickness of the micelle).

5- Equation (74) can still be further simplified to be:

$$\begin{aligned}
& \frac{C - C_0}{C_1 - C_0} \\
& = 1 - \frac{4}{\pi} \sum_{n=0}^{\infty} \frac{8}{(2n+1)^2 \pi^2} e^{\frac{-D(2n+1)^2 \pi^2 t}{4l^2}} \cos\left(\frac{(2n+1)\pi x}{2l}\right)
\end{aligned} \tag{75}$$

6- Rearranging and integrating the equation to obtain M_t , which is the total amount of the drug diffused from the micelles into the surrounding medium, and M_∞ , which represents the total amount of the drug diffused after infinite time,

$$\frac{M_t}{M_\infty} = 1 - \sum_{n=0}^{\infty} \frac{8}{(2n+1)^2 \pi^2} e^{\frac{-D(2n+1)^2 \pi^2 t}{4l^2}} \tag{76}$$

7- Now will apply the error function to derive an even simpler form for this equation that is useful for small intervals of time,

$$\frac{M_t}{M_\infty} = 2 \left(\frac{Dt}{l^2}\right)^{\frac{1}{2}} \left(\pi^{-\frac{1}{2}} + 2 \sum_{n=1}^{\infty} (-1)^n \operatorname{ierfc}\left(\frac{nl}{\sqrt{Dt}}\right)\right) \tag{77}$$

Where,

$$\operatorname{erfc}(z) = 1 - \operatorname{erf}(z) = \frac{2}{\sqrt{\pi}} \int_z^{\infty} e^{-t^2} dt \tag{78}$$

And subsequently,

$$\operatorname{ierfc}(x) = \int_x^{\infty} \operatorname{erfc}(z) dz = \frac{1}{\pi^{\frac{1}{2}}} e^{-x^2} - x \operatorname{erfc}(x) \tag{79}$$

As seen in equation (79), the *ierfc* function will increase toward infinity; its value declines to a value near 0. As a result, the smaller the time intervals, the *ierfc* function turns into infinitely large value, yielding a small impact from the *ierfc* term. Due to that reason, the second term from the derived equation approaches 0 and can be omitted when dealing with small intervals of time, giving:

$$\frac{M_t}{M_\infty} = 2 \left(\frac{Dt}{\pi l^2} \right)^{\frac{1}{2}} \quad (80)$$

8- The Korsmeyer-Peppas constant is taken to be:

$$k_{kp} = 2 \left(\frac{D}{\pi l^2} \right)^{\frac{1}{2}} \quad (81)$$

9- To write the above equations in terms of CFR, we will assume that **CFR** will equal to $\frac{M_t}{M_\infty}$ (this done under the assumption that the initial amount of the diffused drug is negligible) and with the introduction of k_{kp} , the equation above becomes:

$$CFR = \frac{M_t}{M_\infty} = k_{kp} t^{\frac{1}{2}} \quad (82)$$

When **CFR** is being plotted against the square root of time, a straight-line is obtained, which features a slope of $2 \left(\frac{D}{\pi l^2} \right)^{\frac{1}{2}}$. This model and derivation hold if the DDS follows Fick's Law. In many cases, the release mechanism departs from Fick's Law, because there is usually more than one release mechanism at play. This led to a broader equation that describes a range of release mechanisms:

$$CFR = \frac{M_t}{M_\infty} = at^n \quad (83)$$

As previously mentioned, n characterizes the different release mechanisms. By applying natural logarithms to both sides of equation (83), the equation is linearized to reach,

$$\ln(CFR) = \ln(a) + n \ln(t) \quad (84)$$

When plotting $\ln(CFR)$ versus the natural logarithm of time, a straight-line results, with a y-intercept of $\ln(a)$ and n as a slope. In this thesis, a and n were obtained

by trial and error procedure using equation (83) instead of using the linearized form of equation (84). The plots for both non-folated and folated micelles at 3.54 W/cm^2 for the Korsmeyer-Peppas model are presented in Figures 4.13 and 4.14.

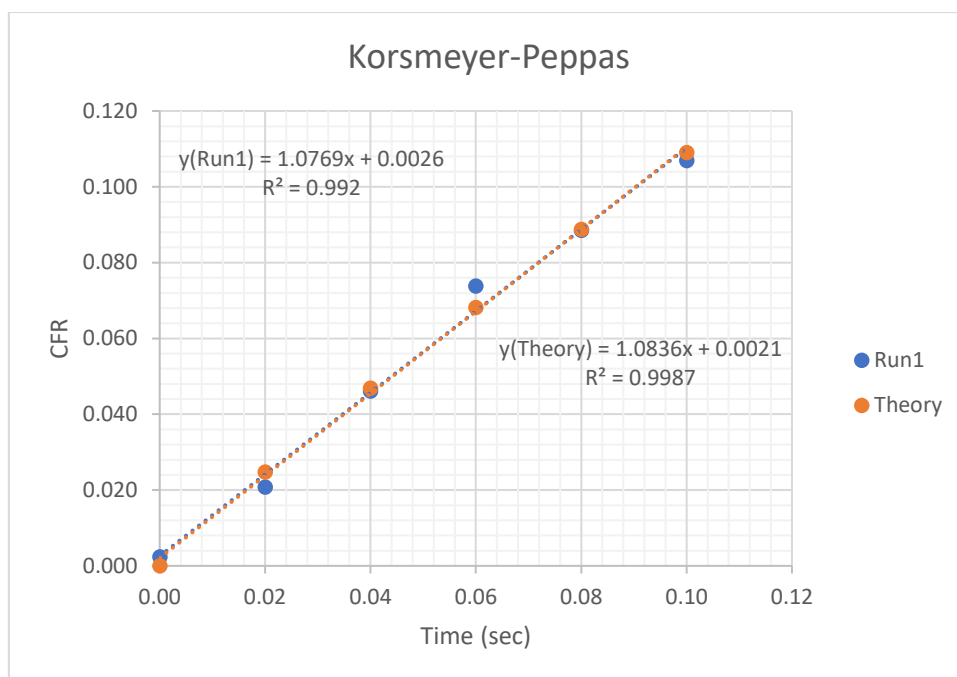


Figure 4.13: The fit of experimental data to the Korsmeyer-Peppas model for DOX release from non-targeted micelles at a power density of 3.54 W/cm^2 .

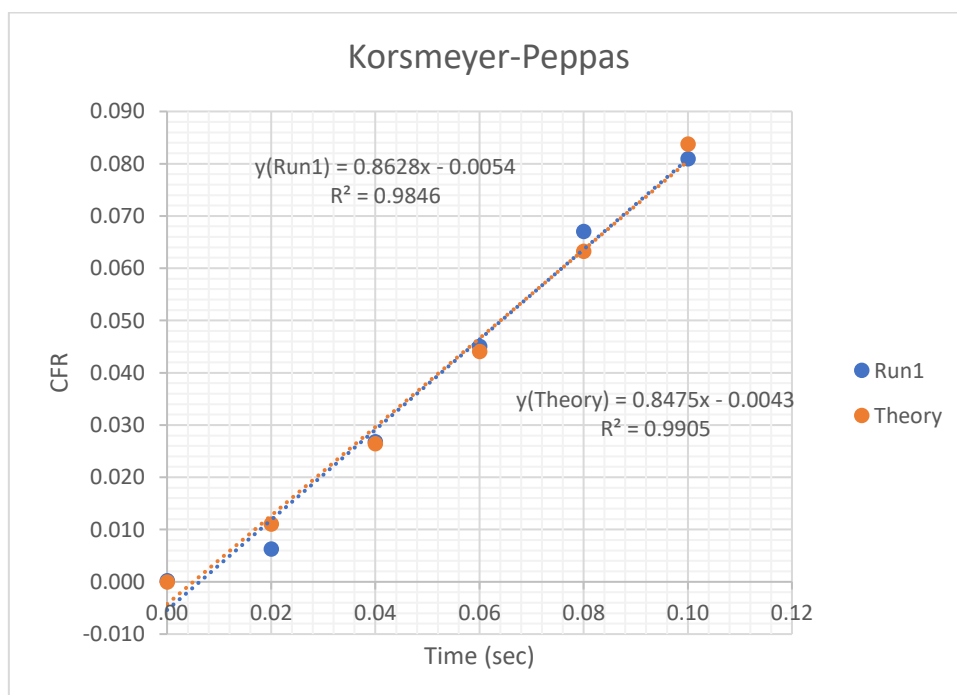


Figure 4.14: The fit of experimental data to the Korsmeyer-Peppas model for DOX release from folated micelles at a power density of 3.54 W/cm^2 .

4.3.6. Weibull model. The Weibull model is an empirical model that has an extended exponential form, and it can be applied to a variety of drug dissolution/release cases. The dosage form geometry has a direct effect on the dissolution properties; the dissolution rates from Euclidean spaces have been explained and described abundantly in literature. Nevertheless, an intriguing issue arises when release device geometry is irregular, e.g., a fractal geometry. Bunde et al. [119] were pioneers in studying the dosage forms dissolution rates with fractal geometries. Their work stated that the release rate could be expressed by using the power-law. Yet, recent studies have discovered that the power-law, or Korsmeyer-Peppas model, is representative of the drug dissolution at initial stages of drug release only. While the Weibull model is better at predicting the release behavior at later stages of the release. Therefore, giving it a broader and more universal view of the release profile [116]. This model is under the assumption that there exist a number of drug particles in the system, N , that are homogeneously dispersed in the percolation cluster (refer Figure 4.14).

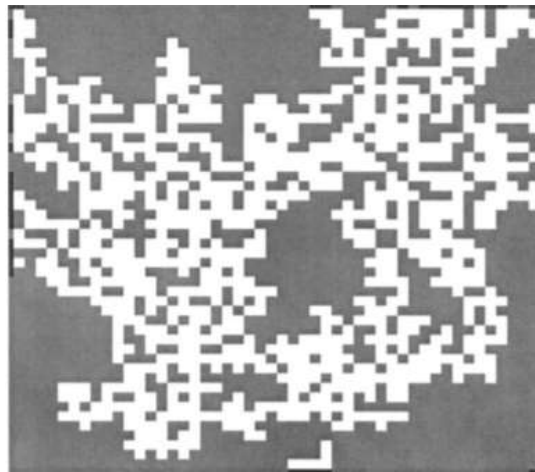


Figure 4.15: Example of a Percolation Fractal Embedded on a 2-dimensional Square Lattice, where the Exits are marked by a dark color, and gray for blocked areas [90].

For these particles to release into the solution, they have to reach an exit and escape from the cluster. The rate of escaping particles (in this case, drug particles) is anticipated to be proportional to the fraction of particles, fr , that can reach an exit in the time interval, dt . As soon as particles escape, depletion zones are created, which results in the de-homogenization of the system, and segregation effects start to have a significant effect on release. For describing these effects, fr will be a function of time $fr(t)$ [87], [90], [92].

- Model derivation:

The process of drug release can be modeled as using fractal kinetics as follows



Where A refers to the particles diffusing (in this case, drug particles), and B are the sites or static particles (the solution). As a result, we will have a differential equation, as shown below:

$$\frac{dN}{dt} = -k'fr(t)N \quad (86)$$

Here k' denotes proportionality constant, which considers a constant concentration of B, and $fr(t)$. N stands for the number of particles that are able to reach an exit in a time interval of dt . The negative sign for the N value signifies that the particles in the DDS are decreasing with time. The key assumption in fractal kinetics that $fr(t)$ has the form illustrated below:

$$fr(t) \approx t^{-m} \quad (87)$$

Then equation (86) can be expressed as follows,

$$\frac{dN}{dt} = -k' \frac{N}{t^m} \quad (88)$$

- 1- By applying the method of separation of variables, and integrating with the limits of 0 to t for the time interval, and N_0 and N respectively, where N_0 represents the initial amount of the drug inside the DDS, or subsequently, the final release of the drug into the solution,

$$\int_{N_0}^N \frac{dN}{N} = \int_0^t -k't^{-m} dt \quad (89)$$

$$\ln\left(\frac{N}{N_0}\right) = -k't^{1-m} \quad (90)$$

$$N = N_0 e^{-k't^{1-m}} \quad (91)$$

If N and N_0 where to be replaced by the amount of drug, or M_d and M_0 , respectively. Then, by multiplying both sides of the equation with the mass of each particle, and a constant b is defined as $b = 1 - m$, a more recognizable version of the Weibull equation is obtained:

$$M_d = M_0 e^{-k't^b} \quad (92)$$

M_d denotes the amount of drug remaining in the DDS, and the drug in solution at any given time, M , is expressed as

$$M = M_0 - M_d = M_0(1 - e^{-k't^b}) \quad (93)$$

- 2- Now will assume that the initial drug concentration in solution is negligible, and once more expressing the equation in CFR terms, CFR will be equal to $\frac{M}{M_0}$. Finally, taking natural logarithm for both sides of the equation and rearrange it to be,

$$\ln(1 - CFR) = -k't^b \quad (94)$$

- 3- Again, by taking natural logarithm for both sides of equation (94) (depending on if the values attained in the release experiment allow it),

$$\ln(\ln(1 - CFR)) = \ln(-k') + b \ln(t) \quad (95)$$

A plot of $\ln(\ln(1 - CFR))$ versus $\ln(t)$ can be generated and have a straight-line graph with a slope of b and a y -intercept value of $\ln(-k')$.

In this thesis, the linearized form was not used to deduce the kinetic parameters, but instead, equation (94) was utilized and to find the values of b and k' by a trial and error procedure. The plots for both non-folated and folated micelles at 3.54 W/cm^2 for the Weibull model are presented in Figures 4.16 and 4.17.

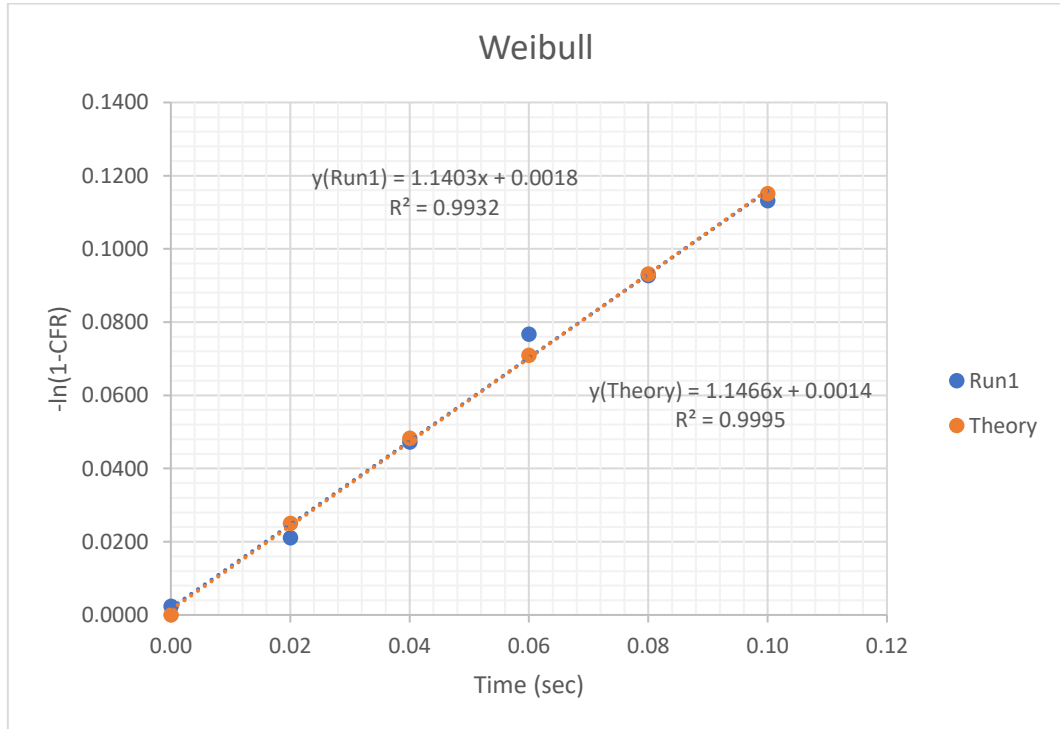


Figure 4.16: The fit of experimental data to the Weibull model for DOX release from non-folated micelles at a power density of 3.54 W/cm^2 .

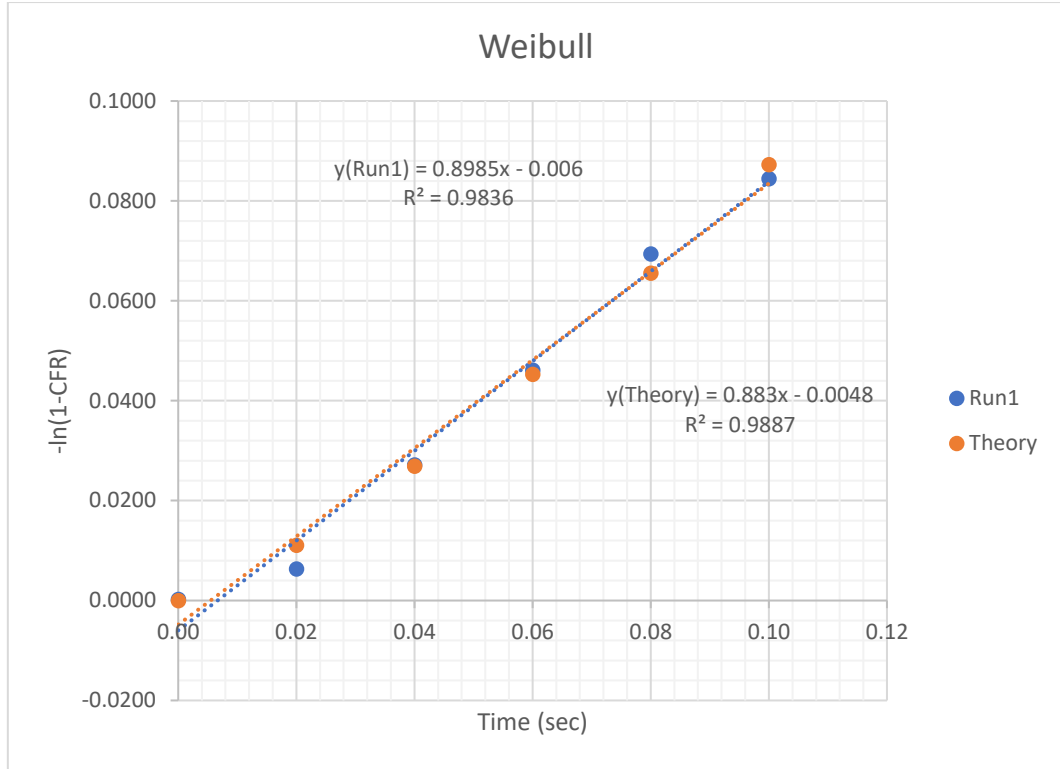


Figure 4.17: The fit of experimental data to the Weibull model for DOX release from folated micelles at a power density of 3.54 W/cm².

4.3.7. Baker–Lonsdale model. The Baker–Lonsdale model was developed by modifying the Higuchi model. This model is used to describe the drug release from spherical matrices, with the assumption that the matrix is homogenous and has no fractures that will result in unintended release. This model can be expressed mathematically as follows:

$$\frac{3}{2} \left[1 - \left(1 - \frac{M_t}{M_\infty} \right)^2 \right] - \frac{M_t}{M_\infty} = \frac{3D_m C_{ms}}{r_0^2 C_0} t \quad (96)$$

Here M_t is the amount of drug released at any given time t and M_∞ is the amount of drug released at infinite time; C_{ms} stands for the drug solubility in the system, D_m represents the diffusion coefficient, r_0 is the radius of spherical matrix and C_0 represents the initial drug concentration in the matrix.

- 1- On the assumption that there is no initial amount of drug released into the surrounding solution and expressing the equation in terms of CFR , yields:

$$\frac{M_t}{M_\infty} = CFR \quad (97)$$

- 2- Substituting equation (97) back into equation (96), and combining all the constants into one parameter:

$$\frac{3}{2} \left[1 - (1 - CFR)^{\frac{2}{3}} \right] - CFR = k_{BL} t \quad (98)$$

- 3- k_{BL} is hence defined as:

$$k_{BL} = \frac{3D_m C_{ms}}{r_0^2 C_0} \quad (99)$$

When $\frac{3}{2} \left[1 - (1 - CFR)^{\frac{2}{3}} \right] - CFR$ is plotted against t , a straight line with slope k_{BL} will be achieved. The plots for both non-folated and folated micelles at 3.54 W/cm^2 for Baker-Lonsdale model are presented in Figures 4.18 and 4.19.

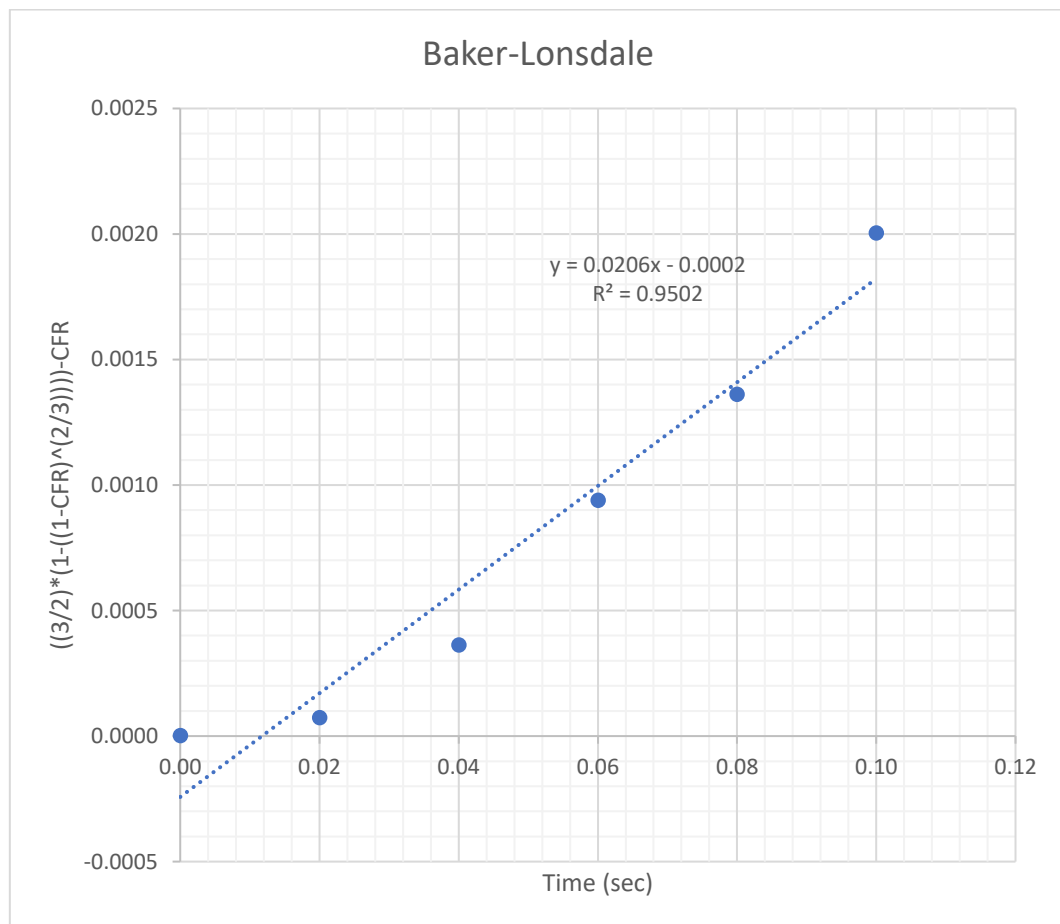


Figure 4.18: The fit of experimental data to the Baker-Lonsdale model for DOX release from non-folated micelles at a power density of 3.54 W/cm^2 .

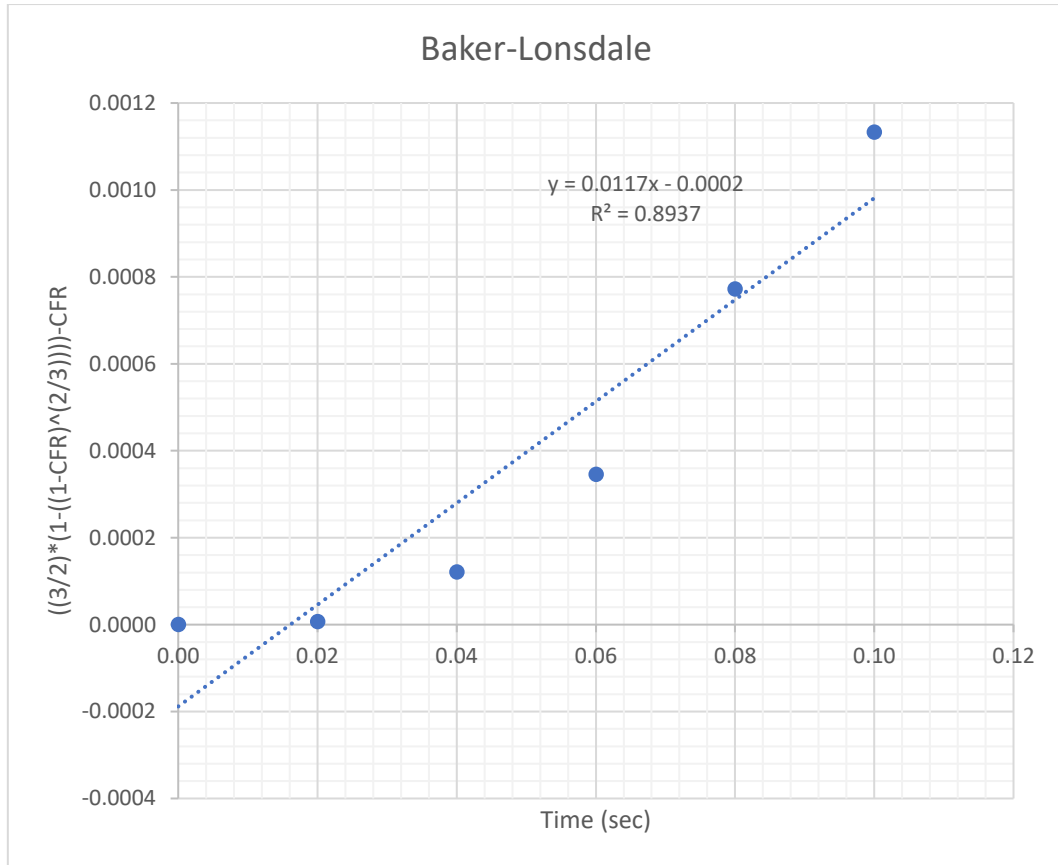


Figure 4.19: The fit of experimental data to the Baker-Lonsdale model for DOX release from folated micelles at a power density of 3.54 W/cm².

4.3.8. The Hopfenberg model. This model was derived to describe the kinetics of drug release from slabs, spheres, and infinite cylinders that go through heterogenous erosion. The model is expressed by the equation below:

$$\frac{M_t}{M_\infty} = 1 - \left[1 - \frac{k_0 t}{C_0 a_0} \right]^n \quad (100)$$

M_t denotes the amount of drug dissolved at any given time t , M_∞ stands for the amount of drug dissolved when the pharmaceutical dosage form has been fully exhausted (after infinite time), k_0 is the erosion rate constant, C_0 refers as the initial drug concentration in the matrix, a_0 represents the initial radius of the sphere/cylinder or half the thickness of the slab, and n represents an exponent that differs with geometry $n=1$ (flat), and $n=2$ (cylindrical), and $n=3$ (spherical).

- 1- Using the assumption that there is no initial amount of drug dissolved and expressing the equation in terms of CFR , we will obtain:

$$\frac{M_t}{M_\infty} = CFR \quad (101)$$

2- Substituting equation (101) into equation (99) and rearranging equation to get:

$$1 - (1 - CFR)^{\frac{1}{n}} = k_{Hf}t \quad (102)$$

3- k_{Hf} is defined as:

$$k_{Hf} = \frac{k_0}{C_0 a_0} \quad (103)$$

4- In the case of micelles, and since they have a spherical shape, then $n = 3$; thus, equation (102) can be expressed in the form:

$$1 - (1 - CFR)^{\frac{1}{3}} = k_{Hf}t \quad (104)$$

When plotting $1 - (1 - CFR)^{\frac{1}{3}}$ versus t a straight line graph will be obtained with a slope of k_{Hf} . The plots for both non-folated and folated micelles at 3.54 W/cm^2 for Hopfenberg model are presented in Figures 4.20 and 4.21.

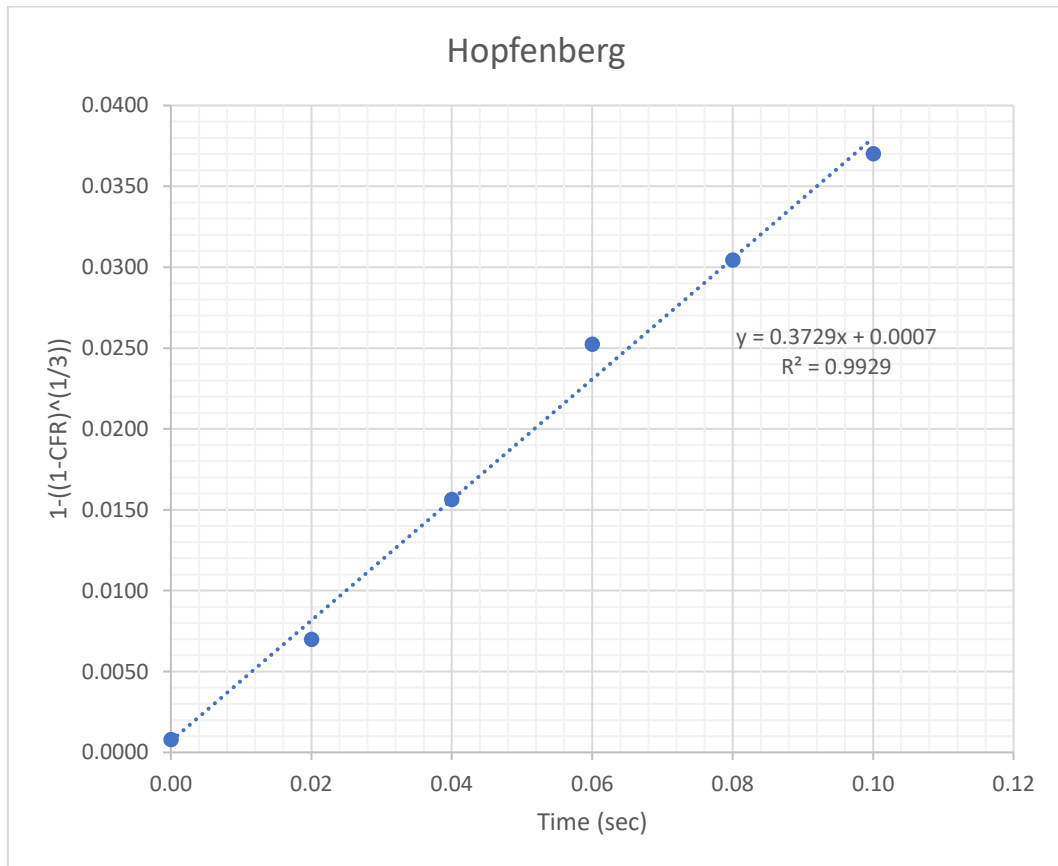


Figure 4.20: The fit of experimental data to the Hopfenberg model for DOX release from non-folated micelles at a power density of 3.54 W/cm^2 .

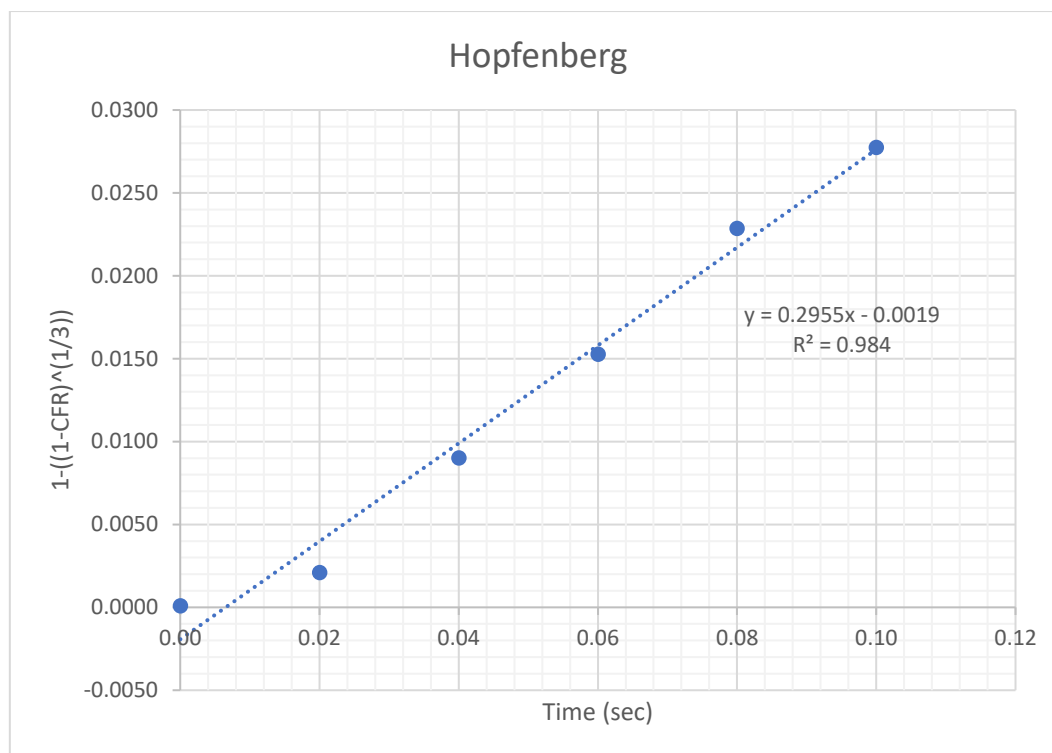


Figure 4.21: The fit of experimental data to the Hopfenberg model for DOX release from folated micelles at a power density of 3.54 W/cm².

4.4. Data Fitting.

As mentioned earlier, the coefficient of determination R² values, obtained using the linear trend line equations of the generated modeling plots, have been used to decide on the best fitting model(s). A summary for both model kinetics constants (k values) and R² values for each model are presented in Tables 4.5 through 4.8 for both folated (PF) and non-folated micelles (POH). According to the tables shown below, the collected data exhibited good adherence to all models; but Higuchi has the highest R² value. In conclusion, the Higuchi model provided the best fit to the acoustically triggered DOX-release from micelles experimental CFR data. It is interesting to note that Higuchi's model was derived based on Cartesian coordinates, and the drug delivery system being investigated in this system deals with spherical structures.

Table 4.5: The average of k values for non-folated for each model at six power densities.

| K values (POH) | | | | | | | | | |
|----------------|--------|--------|-------|---------|---------|--------|---------|---------|------------|
| Power Density | Models | Zero | First | Higuchi | Hix-Cro | Peppas | Weibull | Bak-Lon | Hopfenberg |
| 2.389 | 1.170 | 41.280 | 0.333 | 0.390 | 0.360 | 0.402 | 0.025 | 0.407 | |
| 2.546 | 1.157 | 27.867 | 0.343 | 0.386 | 0.400 | 0.452 | 0.027 | 0.404 | |
| 3.540 | 1.029 | 25.907 | 0.475 | 0.343 | 0.849 | 0.968 | 0.022 | 0.358 | |
| 5.013 | 0.995 | 21.934 | 0.416 | 0.332 | 0.588 | 0.657 | 0.020 | 0.345 | |
| 5.432 | 1.012 | 20.429 | 0.422 | 0.337 | 0.621 | 0.710 | 0.022 | 0.352 | |
| 5.914 | 0.979 | 21.721 | 0.385 | 0.326 | 0.496 | 0.559 | 0.020 | 0.340 | |

Table 4.6: The average of R^2 values for non-folated for each model at six power densities.

| Regression (POH) | | | | | | | | | |
|------------------|------------|-------|-------|---------|---------|--------|---------|---------|------------|
| Power Density | Models | Zero | First | Higuchi | Hix-Cro | Peppas | Weibull | Bak-Lon | Hopfenberg |
| | 2.389 | 0.861 | 0.799 | 0.924 | 0.861 | 0.851 | 0.859 | 0.931 | 0.865 |
| | 2.546 | 0.833 | 0.707 | 0.916 | 0.833 | 0.827 | 0.861 | 0.883 | 0.836 |
| | 3.540 | 0.992 | 0.867 | 0.981 | 0.992 | 0.995 | 0.996 | 0.934 | 0.992 |
| | 5.013 | 0.994 | 0.926 | 0.993 | 0.994 | 0.969 | 0.973 | 0.966 | 0.994 |
| | 5.432 | 0.982 | 0.922 | 0.969 | 0.982 | 0.956 | 0.962 | 0.941 | 0.982 |
| | 5.914 | 0.979 | 0.879 | 0.992 | 0.979 | 0.946 | 0.951 | 0.972 | 0.980 |
| | Avg | 0.940 | 0.850 | 0.962 | 0.940 | 0.924 | 0.934 | 0.938 | 0.942 |

Table 4.7: The average of k values for folated for each model at six power densities.

| K values (PF) | | | | | | | | | |
|---------------|--------|-------|--------|---------|---------|--------|---------|---------|------------|
| Power Density | Models | Zero | First | Higuchi | Hix-Cro | Peppas | Weibull | Bak-Lon | Hopfenberg |
| | 2.389 | 1.536 | 44.078 | 0.677 | 0.512 | 2.259 | 2.960 | 0.032 | 0.534 |
| | 2.546 | 1.658 | 42.224 | 0.763 | 0.553 | 0.940 | 1.024 | 0.037 | 0.578 |
| | 3.540 | 0.902 | 34.578 | 0.407 | 0.301 | 0.844 | 0.941 | 0.016 | 0.311 |
| | 5.013 | 0.711 | 16.261 | 0.281 | 0.237 | 0.308 | 0.341 | 0.014 | 0.247 |
| | 5.432 | 1.058 | 20.033 | 0.342 | 0.353 | 0.540 | 0.655 | 0.029 | 0.372 |
| | 5.914 | 1.360 | 21.373 | 0.568 | 0.453 | 0.997 | 1.187 | 0.042 | 0.481 |

Table 4.8: The average of R^2 values for folated for each model at six power densities.

| Regression (PF) | | | | | | | | | |
|-----------------|------------|-------|-------|---------|---------|--------|---------|---------|------------|
| Power Density | Models | Zero | First | Higuchi | Hix-Cro | Peppas | Weibull | Bak-Lon | Hopfenberg |
| | 2.389 | 0.846 | 0.817 | 0.910 | 0.846 | 0.973 | 0.971 | 0.808 | 0.845 |
| | 2.546 | 0.896 | 0.922 | 0.924 | 0.896 | 0.975 | 0.978 | 0.837 | 0.895 |
| | 3.540 | 0.991 | 0.783 | 0.989 | 0.991 | 0.987 | 0.989 | 0.939 | 0.991 |
| | 5.013 | 0.929 | 0.802 | 0.975 | 0.929 | 0.883 | 0.890 | 0.970 | 0.931 |
| | 5.432 | 0.958 | 0.832 | 0.944 | 0.958 | 0.938 | 0.950 | 0.955 | 0.960 |
| | 5.914 | 0.989 | 0.925 | 0.982 | 0.989 | 0.945 | 0.953 | 0.937 | 0.989 |
| | Avg | 0.935 | 0.847 | 0.954 | 0.935 | 0.950 | 0.955 | 0.908 | 0.935 |

4.5. Release Constant (k) Dependence on Power Density and Temperature.

4.5.1. Release constant dependence on power density. We propose a new parameter to characterize release from micelles using ultrasound, namely the activation power density depicted in Figure 4.22. In order to calculate and obtain the acoustic activation power density, a modified form of the Arrhenius is utilized [52]:

$$k_r = A e^{\frac{-PD_a}{PD}} \quad (105)$$

Here k_r is the release rate constant, A denotes the pre-exponential factor, PD represents the power density, and PD_a stands for the acoustic activation power density.

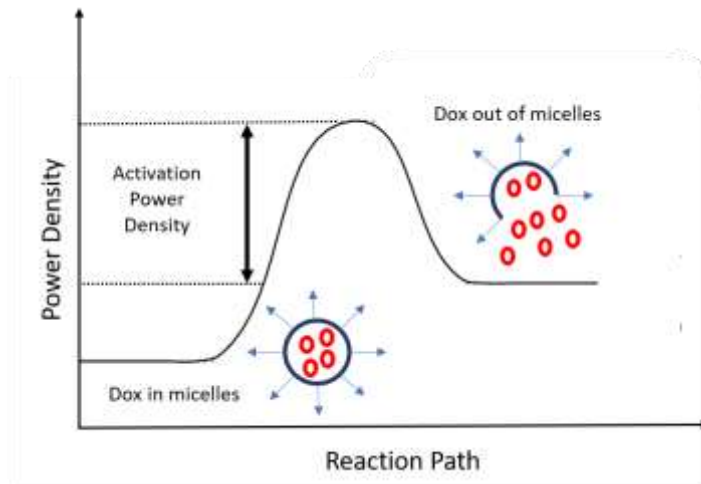


Figure 4.22: Plot illustrating the activation power density required to release encapsulated DOX from micelles [52].

To obtain the values of A and PD_a , the equation must be linearized as follows:

$$\ln(k_r) = \ln(A) - \frac{PD_a}{PD} \quad (106)$$

Therefore, a plot of $\ln(k_r)$ versus $1/PD$ results in a straight line that has a slope of $-PD_a$, or the negative of the acoustic activation power density, and y-intercept of the natural logarithm of the modified-Arrhenius pre-exponential factor. The plots for folated micelles for each of the discussed models and applying equation (90) are presented in Figures 4.23 through 4.30. At the end, a summary Table 4.9 is represented to show the values of A and PD_a for each of the models. Finding the value of PD_a helps to determine the acoustic activation power density that is necessary to shear the micelles and release the drug under the action of ultrasound.

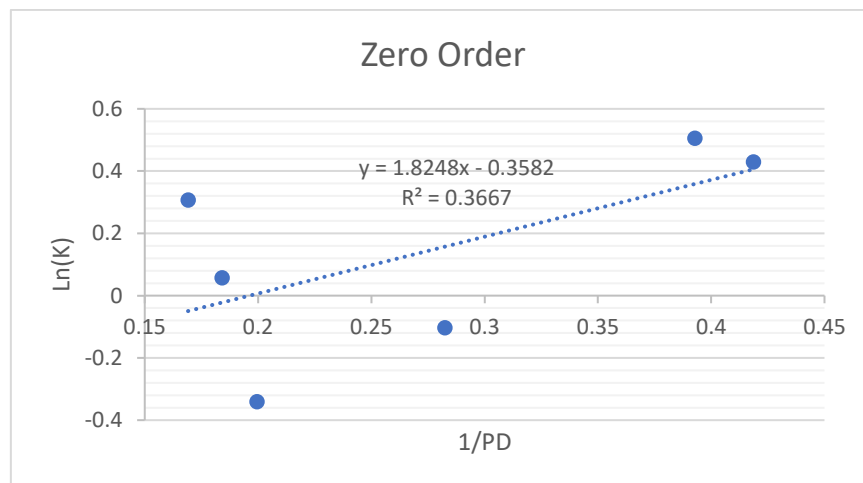


Figure 4.23: Zero-order model plot used to find the acoustic activation power density for release from folated micelles

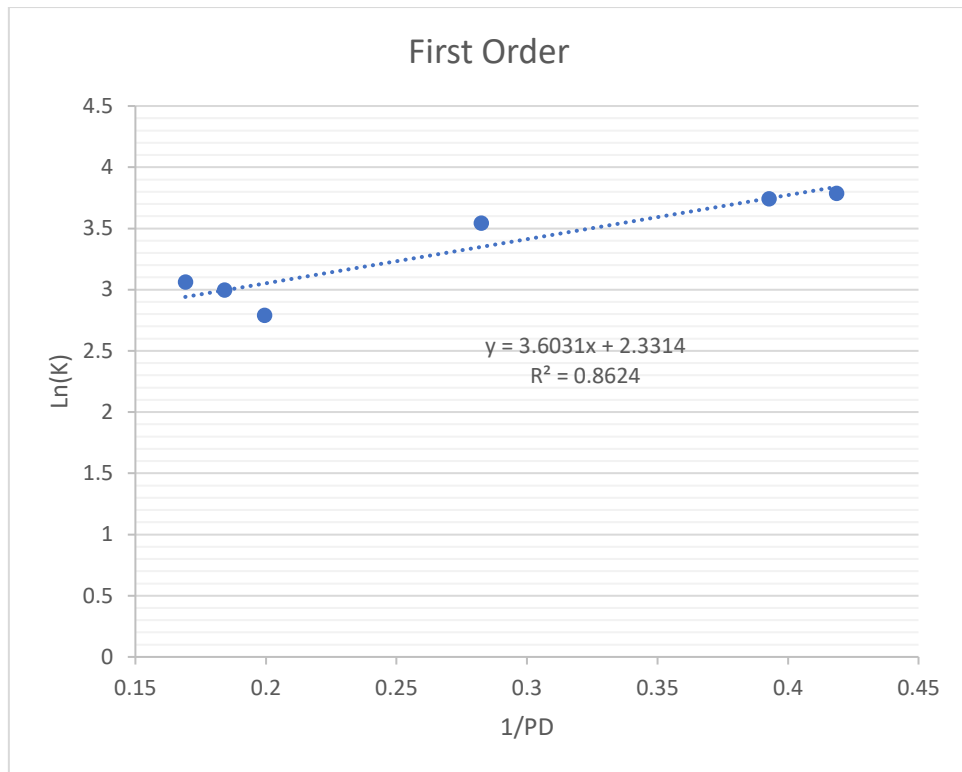


Figure 4.24: First-order model plot used to find the acoustic activation power density for release from folated micelles

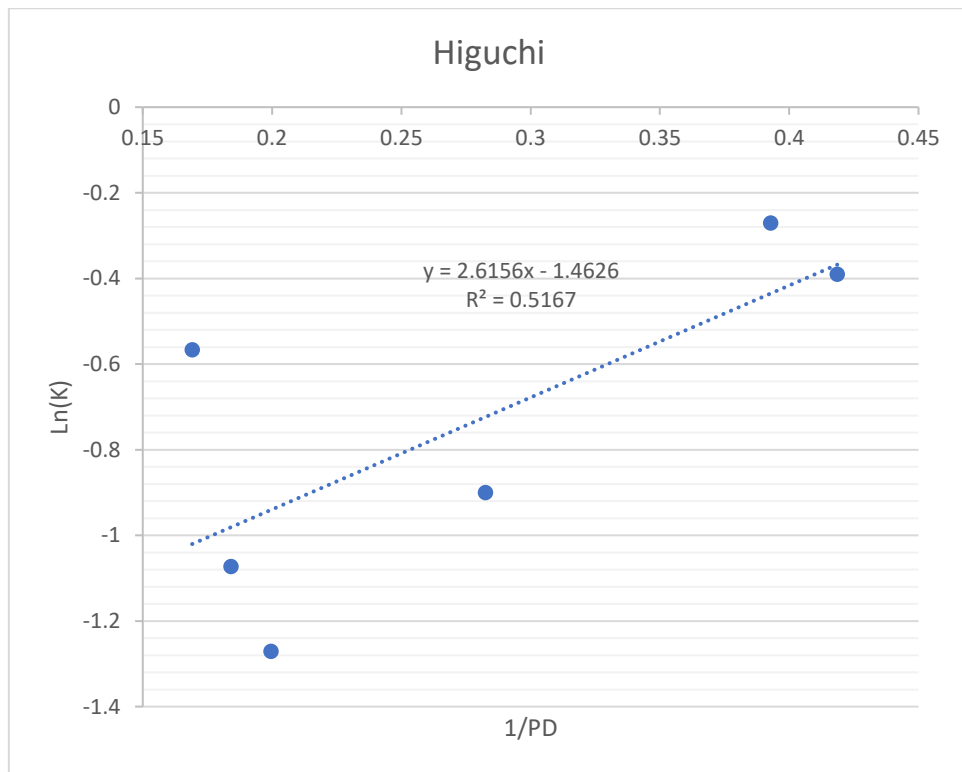


Figure 4.25: Higuchi model plot used to find the acoustic activation power density for release from folated micelles

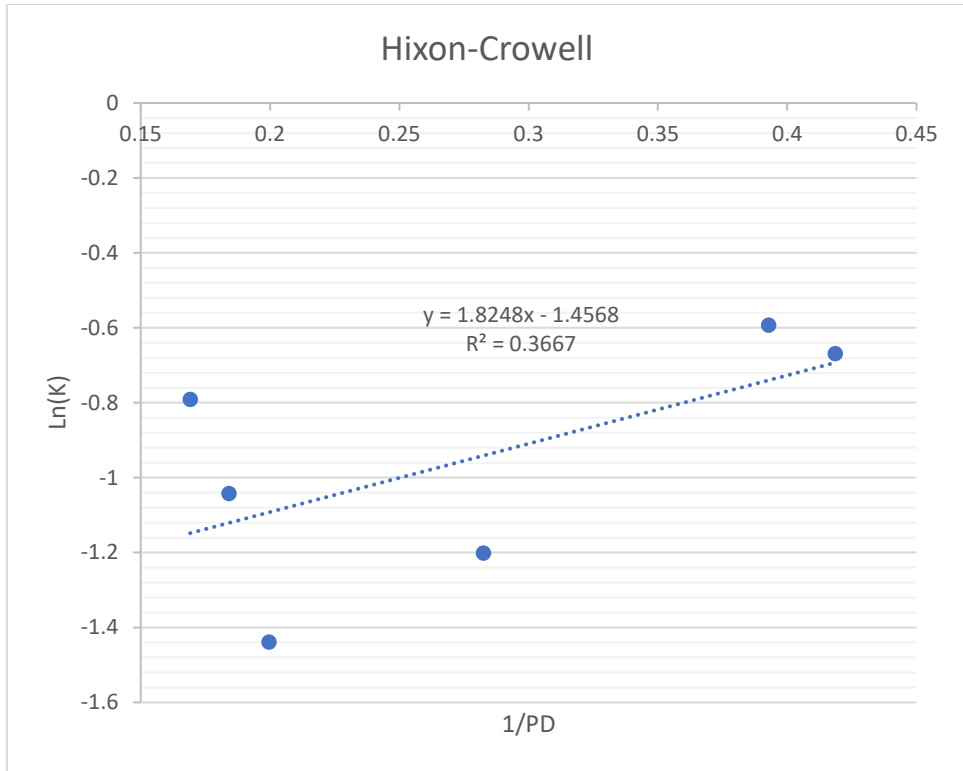


Figure 4.26: Hixon-Crowell model plot used to find the acoustic activation power density for release from folated micelles

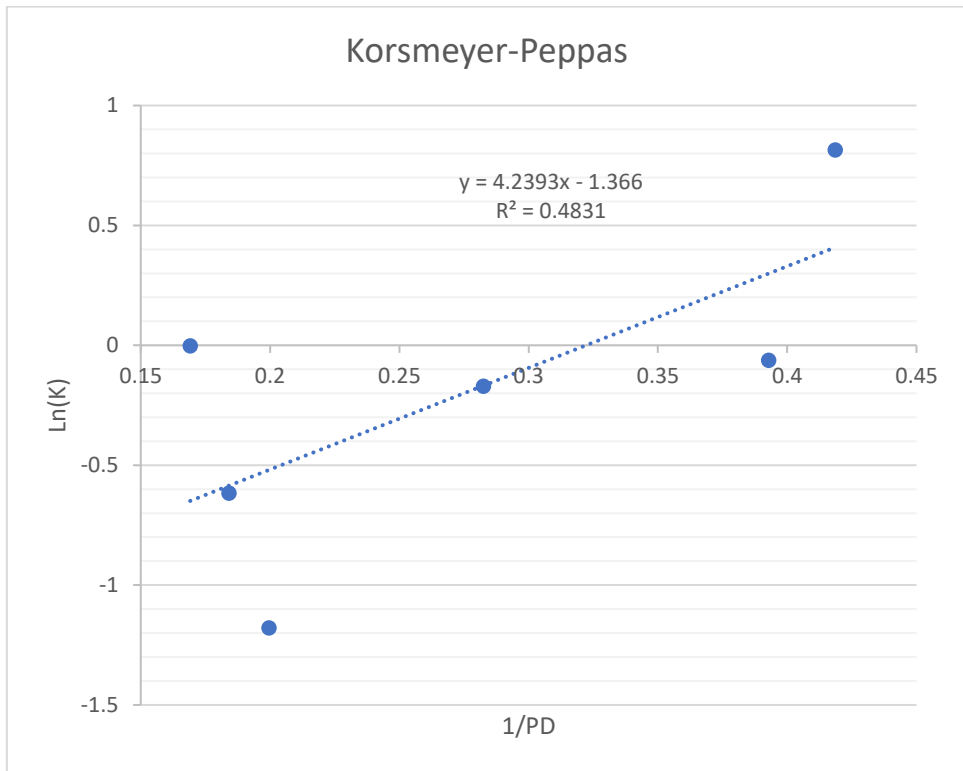


Figure 4.27: Korsmeyer-Peppas model plot used to find the acoustic activation power density for release from folated micelles

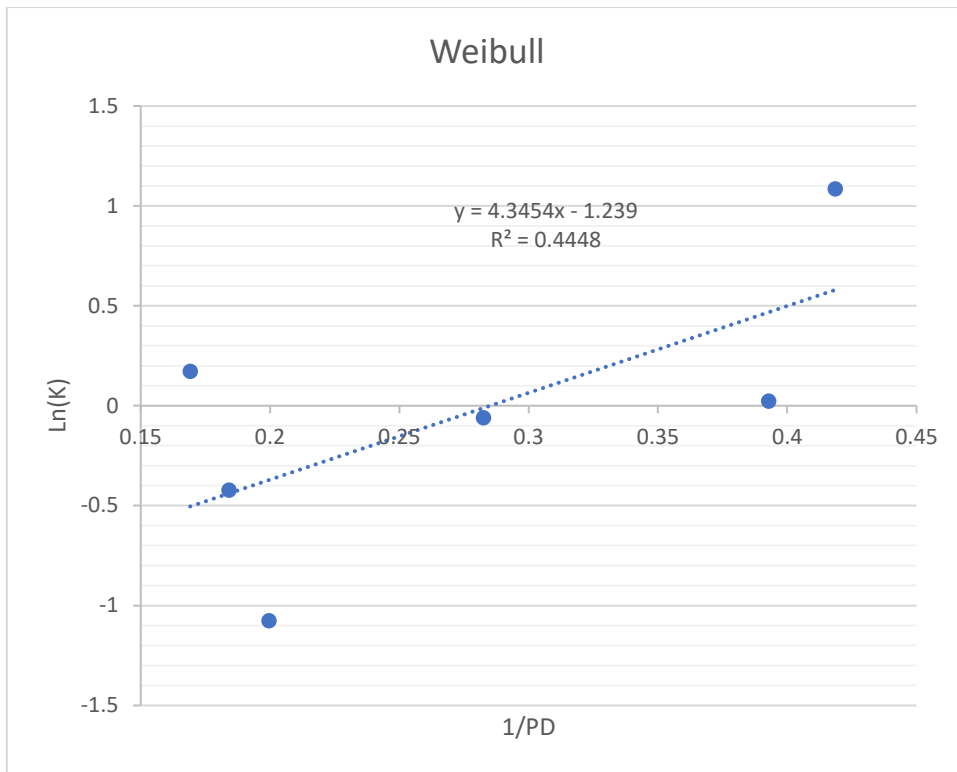


Figure 4.28: Weibull model plot used to find the acoustic activation power density for release from folated micelles

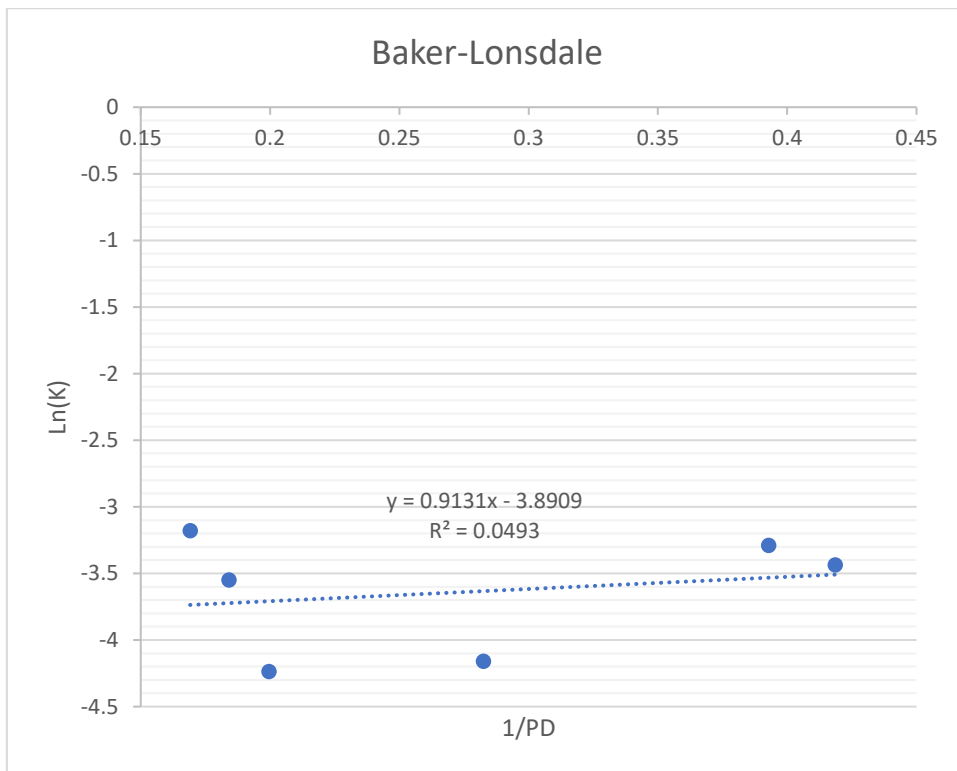


Figure 4.29: Baker-Lonsdale model plot used to find the acoustic activation power density for release from folated micelles

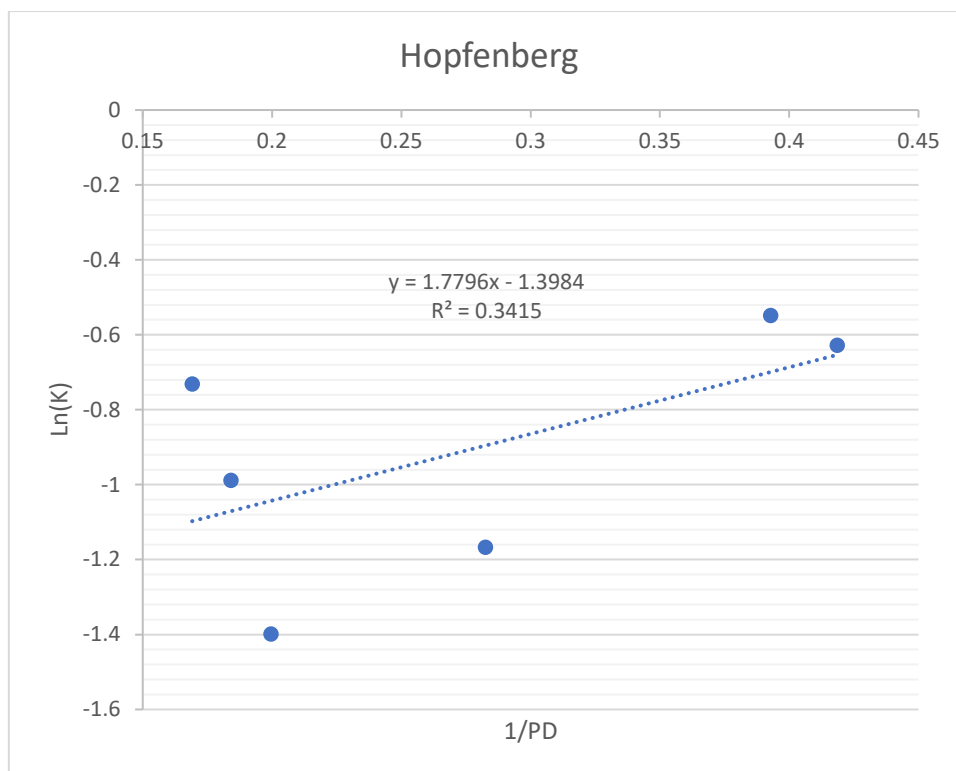


Figure 4.30: Hopfenberg model plot used to find the acoustic activation power density for release from folated micelles

Table 4.9: Values of PDA and A for each model

| Models | PDA | Ln(A) | A |
|--------------------|-------|--------|--------|
| Zero Order | 1.825 | -0.358 | 0.699 |
| First Order | 3.603 | 2.331 | 10.292 |
| Higuchi | 2.616 | -1.463 | 0.232 |
| HixCro | 1.825 | -1.457 | 0.233 |
| Peppas | 4.239 | -1.366 | 0.255 |
| Weibull | 4.345 | -1.239 | 0.290 |
| BakLon | 0.913 | -3.891 | 0.020 |
| Hopfenberg | 1.780 | -1.398 | 0.247 |

4.5.2. Release constant dependence on temperature. Temperature is another critical parameter that controls drug release from micelles, which can be depicted in Figure 4.31. We studied the release by applying the Arrhenius equation:

$$k = A e^{\frac{-E_a}{RT}} \quad (107)$$

Here k is the release rate constant, A denotes the pre-exponential factor, E_a represents the activation energy, R is the universal gas constant, and T stands for the temperature in Kelvin.

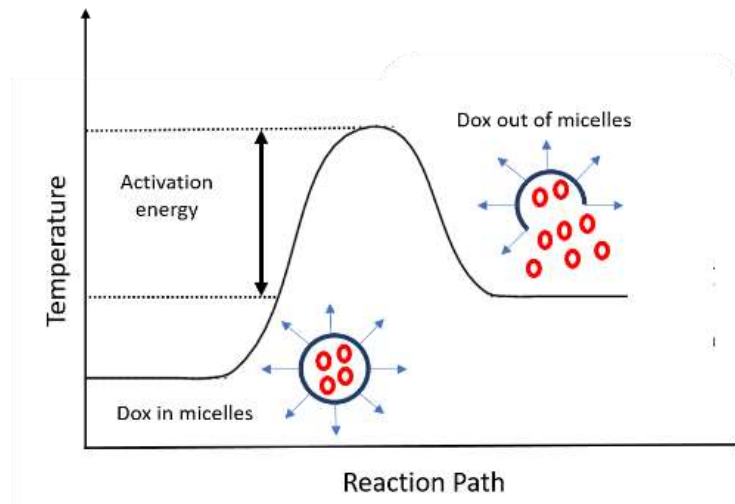


Figure 4.31: Plot illustrating the activation energy required to release encapsulated DOX from micelles [52].

To acquire the values of A and E_a , the equation must be linearized as follows:

$$\ln(k) = \ln(A) - \frac{E_a}{RT} \quad (108)$$

Therefore, a plot of $\ln(k)$ against $\frac{1}{T}$ is generated, which will result in a straight line that has a slope of $\frac{-E_a}{R}$, or the negative of the activation energy, and a y-intercept of the natural logarithm of the Arrhenius pre-exponential factor. The plot for non-folated micelles for each different temperature (25°C, 37°C, and 56°C) (using the Higuchi model) and applying the Arrhenius equation are presented in Figure 4.32. The value of E_a is 18936.25 in units of J/mol, respectively. Finding the value of E_a helps to determine the energy that is needed to shear the micelles and release the drug.

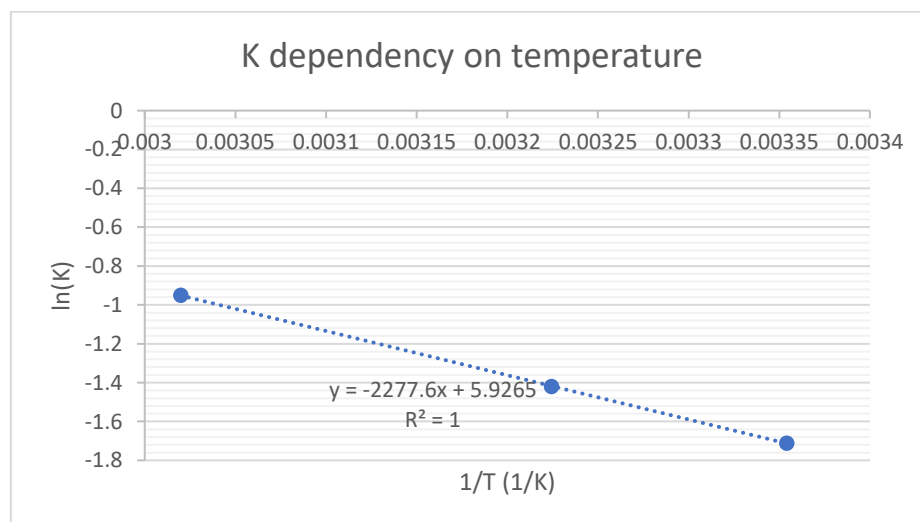


Figure 4.32: Plot used to find the activation energy for release from non-folated micelles for different temperatures

Chapter 5. Conclusion

The focus of this research is to find new ways to treat cancer. Statistics show how cancer is critically viewed as a fatal disease, and what are the available treatment methods and their limitations. Therefore, this thesis is intended to propose a better, safer, and more effective solution to chemotherapy side effects (i.e. heart intoxication, hair loss, etc.). This thesis is focused on studying targeted nanocarrier loaded with anti-cancer drugs. Tests are utilized to confirm the attachment, release experiments are performed, and the results are compared between free DOX and the conjugated nanocarrier. In this research, experimental data for ultrasonic drug release from Pluronic P105 micelles with and without an attached folic acid ligand were analyzed. The thesis also provides a short background on drug delivery systems, recent developments in the field, and different available moieties. The materials and methods section is the preparation methods for different chemical reagents that are used in this study such as the preparation of Pluronic P105 (non-stabilized micelles) stock solutions, the preparation method for P105 micelles stabilized using an interpenetrating network of N,N-diethylacrylamide (NanoDelivTM) and micelles formed by PEO-b-poly(NIPAAm-co-HEMA-lactate_n) (PNHL). The conjugating method followed to synthesize folate-targeted micelles. The second part of the materials and methods section briefly illustrated the design of the setup used to run the experiments and how to measure the kinetics of acoustically activated drug release from micelle. The materials and methods section then extensively discussed the modeling of the acoustic release from different types of micelles. This was achieved using mechanistic models, stochastic models, and statistical models that are used to analyze the results. Finally, a short explanation of the mechanical index and its significance is presented in the methods sections. Release from non-folated micelles is always slightly lower than release from the folated micelles. That is due to the addition of moiety (in this case, folic acid) will make the micelles more ultrasound sensitive (sonosensitive). Moreover, an increase in any of the experimental variables (mechanical index, temperature, or power density); leads to an increase in the percentage of drug released. Finally, the Higuchi model provided the best fit to the release data, which means that the acoustic data available conform to this model's assumptions and release mechanism.

References

- [1] G. M. Cooper, *The cell : a molecular approach*, Sunderland, MA: Sinauer Associates, 2000.
- [2] H. Kasai, "What causes human cancer? Approaches from the chemistry of DNA damage", *Genes and Environment*, vol. 38, no. 1, p. 19, 2016.
- [3] N. Ashford, P. Bauman, H. Brown, R. Clapp, A. Finkel, D. Gee, D. Hattis, M. Martuzzi, A. Saso and J. Sass, "Cancer risk: Role of environment", *Science*, vol. 347, no. 6223, pp. 727-727, 2015
- [4] C. Pritchard, J. Mateo, M. Walsh, N. De Sarkar, W. Abida, H. Beltran, A. Garofalo, R. Gulati, S. Carreira, R. Eeles, O. Elemento, M. Rubin, D. Robinson, R. Lonigro, M. Hussain, A. Chinnaiyan, J. Vinson, J. Filipenko, L. Garraway, M. Taplin, S. AlDubayan, G. Han, M. Beightol, C. Morrissey, B. Nghiem, H. Cheng, B. Montgomery, T. Walsh, S. Casadei, M. Berger, L. Zhang, A. Zehir, J. Vijai, H. Scher, C. Sawyers, N. Schultz, P. Kantoff, D. Solit, M. Robson, E. Van Allen, K. Offit, J. de Bono and P. Nelson, "Inherited DNA-Repair Gene Mutations in Men with Metastatic Prostate Cancer", *New England Journal of Medicine*, vol. 375, no. 5, pp. 443-453, 2016.
- [5] World Health Organization. "Cancer." Internet: <https://www.who.int/news-room/fact-sheets/detail/cancer>, [May 12, 2019].
- [6] A. Mishra, *Nanomedicine for drug delivery and therapeutics*. Beverly, MA: Scrivener Publishing, Wiley, 2013.
- [7] P. Mi and N. Nishiyama. "Polymeric Nanocarriers for Cancer Therapy," in *Nano-Oncologicals: New Targeting and Delivery Approaches*, 1st ed., M. J. Alonso and M. Garcia-Fuentes, Eds. Cham: Springer International Publishing, 2014, pp. 67–94.
- [8] H. Xia, Y. Zhao, and R. Tong. "Ultrasound-Mediated Polymeric Micelle Drug Delivery," in *Therapeutic Ultrasound*, 1st ed., J.-M. Escoffre and A. Bouakaz, Eds. Cham: Springer International Publishing, 2016, pp. 365–384.
- [9] G. Hussein, G. Myrup, W. Pitt, D. Christensen and N. Rapoport, "Factors affecting acoustically triggered release of drugs from polymeric micelles", *Journal of Controlled Release*, vol. 69, no. 1, pp. 43-52, 2000.
- [10] G. Hussein, C. Runyan and W. Pitt, "Investigating the mechanism of acoustically activated uptake of drugs from Pluronic micelles", *BMC Cancer*, vol. 2, no. 1, p. 20, 2002.

- [11] G. Hussein, N. Rapoport, D. Christensen, J. Pruitt and W. Pitt, "Kinetics of ultrasonic release of doxorubicin from pluronic P105 micelles", *Colloids and Surfaces B: Biointerfaces*, vol. 24, no. 3-4, pp. 253-264, 2002.
- [12] M. Muniruzzaman, A. Marin, Y. Luo, G. Prestwich, W. Pitt, G. Hussein and N. Rapoport, "Intracellular uptake of Pluronic copolymer: effects of the aggregation state", *Colloids and Surfaces B: Biointerfaces*, vol. 25, no. 3, pp. 233-241, 2002.
- [13] J. Pruitt, G. Hussein, N. Rapoport and W. Pitt, "Stabilization of Pluronic P-105 Micelles with an Interpenetrating Network of N,N-Diethylacrylamide", *Macromolecules*, vol. 33, no. 25, pp. 9306-9309, 2000.
- [14] G. Hussein, R. El-Fayoumi, K. O'Neill, N. Rapoport and W. Pitt, "DNA damage induced by micellar-delivered doxorubicin and ultrasound: comet assay study", *Cancer Letters*, vol. 154, no. 2, pp. 211-216, 2000.
- [15] G. Hussein, D. Christensen, N. Rapoport and W. Pitt, "Ultrasonic release of doxorubicin from Pluronic P105 micelles stabilized with an interpenetrating network of N,N-diethylacrylamide", *Journal of Controlled Release*, vol. 83, no. 2, pp. 303-305, 2002.
- [16] A. Marin, H. Sun, G. A. Hussein, W. G. Pitt, D. A. Christensen, and N. Y. Rapoport, "Drug delivery in pluronic micelles: effect of high-frequency ultrasound on drug release from micelles and intracellular uptake," *J. Control. Release*, vol. 84, no. 1, pp. 39-47, 2002.
- [17] G. A. Hussein, K. L. O'Neill, and W. G. Pitt, "The comet assay to determine the mode of cell death for the ultrasonic delivery of doxorubicin to human leukemia (HL-60 Cells) from Pluronic P105 micelles," *Technol. Cancer Res. Treat.*, vol. 4, no. 6, pp. 707-711, 2005.
- [18] S. B. Stringham et al., "Over-pressure suppresses ultrasonic-induced drug uptake," *Ultrasound Med. Biol.*, vol. 35, no. 3, pp. 409-415, 2009.
- [19] B. J. Staples, B. L. Roeder, G. A. Hussein, O. Badamjav, G. B. Schaalje, and W. G. Pitt, "Role of frequency and mechanical index in ultrasonic-enhanced chemotherapy in rats," *Cancer Chemother. Pharmacol.*, vol. 64, no. 3, pp. 593-600, 2009.
- [20] B. J. Staples, W. G. Pitt, B. L. Roeder, G. A. Hussein, D. Rajeev, and G. B. Schaalje, "Distribution of doxorubicin in rats undergoing ultrasonic drug delivery," *J. Pharm. Sci.*, vol. 99, no. 7, pp. 3122-3131, 2010.

- [21] T. J. Webster, *Nanomedicine: Technologies and Applications*, 1st ed. Cambridge, UK: Woodhead, 2012.
- [22] D. Douroumis and A. Fahr, *Drug delivery strategies for poorly water-soluble drugs*, 1st ed. Hoboken, UK: John Wiley & Sons, Incorporated, 2013.
- [23] S. Owen, D. Chan and M. Shoichet, "Polymeric micelle stability", *Nano Today*, vol. 7, no. 1, pp. 53-65, 2012.
- [24] R. A. Bader, D. A. Putnam, and A. K. Mishra, *Engineering Polymer Systems for Improved Drug Delivery*. Somerset, NJ: John Wiley & Sons, Incorporated, 2013.
- [25] V. P. Torchilin. "Passive and Active Drug Targeting: Drug Delivery to Tumors as an Example," in *Handbook of Experimental Pharmacology*, 1st ed., M. Schäfer-Korting, Ed. Berlin, Heidelberg: Springer Berlin Heidelberg, 2010, pp. 3–53.
- [26] U. Kedar, P. Phutane, S. Shidhaye, and V. Kadam, "Advances in polymeric micelles for drug delivery and tumor targeting," *Nanomedicine Nanotechnology, Biol. Med.*, vol. 6, no. 6, pp. 714–729, 2010.
- [27] S. D. Steichen, M. Caldorera-Moore, and N. A. Peppas, "A review of current nanoparticle and targeting moieties for the delivery of cancer therapeutics," *European Journal of Pharmaceutical Sciences*, vol. 48, no. 3, pp. 416–427, 2013.
- [28] J. D. Byrne, T. Betancourt, and L. Brannon-Peppas, "Active targeting schemes for nanoparticle systems in cancer therapeutics," *Adv. Drug Deliv. Rev.*, vol. 60, no. 15, pp. 1615–1626, 2008.
- [29] S. K. Sahoo, W. Ma, and V. Labhasetwar, "Efficacy of transferrin-conjugated paclitaxel-loaded nanoparticles in a murine model of prostate cancer," *Int. J. Cancer*, vol. 112, no. 2, pp. 335–340, 2004.
- [30] N. Bertrand, J. Wu, X. Xu, N. Kamaly, and O. C. Farokhzad, "Cancer nanotechnology: The impact of passive and active targeting in the era of modern cancer biology," *Adv. Drug Deliv. Rev.*, vol. 66, pp. 2–25, 2014.
- [31] W. Lu, C. Zhan, and H. Hou. "Targeted Liposomes and Micelles as Carriers for Cancer Therapy," in *Nano-Oncologicals: New Targeting and Delivery Approaches*, 1st ed., M. J. Alonso and M. Garcia-Fuentes, Eds. Cham: Springer International Publishing, 2014, pp. 95–122.

- [32] S. Dhar, F. X. Gu, R. Langer, O. C. Farokhzad, and S. J. Lippard, "Targeted delivery of cisplatin to prostate cancer cells by aptamer functionalized Pt(IV) prodrug-PLGA-PEG nanoparticles," *Proc. Natl. Acad. Sci. U. S. A.*, vol. 105, no. 45, pp. 17356–17361, 2008.
- [33] B. P. Bastakoti and Z. Liu. "Multifunctional polymeric micelles as therapeutic nanostructures: targeting, imaging, and triggered release," in *Micro and Nano Technologies*, A. Fikai and A. M. B. T.-N. for C. T. Grumezescu, Eds. Elsevier, 2017, pp. 261–283.
- [34] J. S. Russell and A. D. Colevas, "The use of epidermal growth factor receptor monoclonal antibodies in squamous cell carcinoma of the head and neck," *Chemother. Res. Pract.*, vol. 2012, p. 1-13, 2012.
- [35] D. R. S. Lopez and A. Lalatsa, "Active Targeting," in *Fundamentals of Pharmaceutical Nanoscience*, I. F. Uchegbu, A. G. Schätzlein, W. P. Cheng, and A. Lalatsa, Eds. New York, NY: Springer New York, 2013, pp. 337–374.
- [36] N. Nasongkla, X. Shuai, H. Ai, B. Weinberg, J. Pink, D. Boothman and J. Gao, "cRGD-Functionalized Polymer Micelles for Targeted Doxorubicin Delivery", *Angew. Chemie Int. Ed.*, vol. 43, no. 46, pp. 6323-6327, 2004.
- [37] H. S. Yoo and T. G. Park, "Folate receptor targeted biodegradable polymeric doxorubicin micelles," *J. Control. Release*, vol. 96, no. 2, pp. 273–283, 2004.
- [38] E. C. Pua and P. Zhong, "Ultrasound-mediated drug delivery," *IEEE Eng. Med. Biol. Mag.*, vol. 28, no. 1, pp. 64–75, 2009.
- [39] S. Ahmed, H. Moussa, A. Martins, M. Al-Sayah and G. Hussein, "Effect of pH, ultrasound frequency and power density on the release of calcein from stealth liposomes", *Eur. J. Nanomedicine*, vol. 8, no. 1, 2016.
- [40] S. Ahmed, N. Awad, V. Paul, H. Moussa and G. Hussein, "Improving the Efficacy of Anticancer Drugs via Encapsulation and Acoustic Release", *Current Topics in Medicinal Chemistry*, vol. 18, no. 10, pp. 857-880, 2018.
- [41] A. Wadi, M. Abdel-Hafez and G. Hussein, "Modeling and Bias-Robust Estimation of the Acoustic Release of Chemotherapeutics from Liposomes", *Journal of Biomedical Nanotechnology*, vol. 15, no. 1, pp. 162-169, 2019.

- [42] S. Ahmed, H. Moussa, A. Martins, Y. Abbas, M. Al-Sayah and G. Hussein, "Factors Affecting the Acoustic In Vitro Release of Calcein from PEGylated Liposomes", *Journal of Nanoscience and Nanotechnology*, vol. 19, no. 11, pp. 6899-6906, 2019.
- [43] A. Wadi, M. Abdel-Hafez, G. Hussein and V. Paul, "Multi-Model Investigation and Adaptive Estimation of the Acoustic Release of a Model Drug From Liposomes", *IEEE Transactions on NanoBioscience*, vol. 19, no. 1, pp. 68-77, 2020.
- [44] N. Awad, V. Paul, M. Mahmoud, N. Al Sawaftah, P. Kawak, M. Al Sayah and G. Hussein, "Effect of Pegylation and Targeting Moieties on the Ultrasound-Mediated Drug Release from Liposomes", *ACS Biomaterials Science & Engineering*, vol. 6, no. 1, pp. 48-57, 2019.
- [45] N. Salkho, V. Paul, P. Kawak, R. Vitor, A. Martins, M. Al Sayah and G. Hussein, "Ultrasonically controlled estrone-modified liposomes for estrogen-positive breast cancer therapy", *Artificial Cells, Nanomedicine, and Biotechnology*, vol. 46, no. 2, pp. 462-472, 2018.
- [46] G. Hussein, W. Pitt and M. Javadi, "Investigating the Stability of eLiposomes at Elevated Temperatures", *Technology in Cancer Research & Treatment*, vol. 14, no. 4, pp. 379-382, 2014.
- [47] G. Hussein, W. Pitt, J. Williams and M. Javadi, "Investigating the Release Mechanism of Calcein from eLiposomes at Higher Temperatures", *Journal of Colloid Science and Biotechnology*, vol. 3, no. 3, pp. 239-244, 2014.
- [48] J. R. Lattin, W. G. Pitt, D. M. Belnap, and G. A. Hussein, "Ultrasound-Induced Calcein Release From eLiposomes," *Ultrasound Med. Biol.*, vol. 38, no. 12, pp. 2163–2173, 2012.
- [49] W. Pitt, G. Hussein, B. Roeder, D. Dickinson, D. Warden, J. Hartley and P. Jones, "Preliminary Results of Combining Low Frequency Low Intensity Ultrasound and Liposomal Drug Delivery to Treat Tumors in Rats", *Journal of Nanoscience and Nanotechnology*, vol. 11, no. 3, pp. 1866-1870, 2011.
- [50] A. Martins, R. Tanbour, M. Elkhodiry and G. Hussein, "Ultrasound-induced doxorubicin release from folate-targeted and non-targeted P105 micelles: a modeling study", *European Journal of Nanomedicine*, vol. 8, no. 1, pp. 17-29, 2016.

- [51] G. Hussein, M. Diaz de la Rosa, E. AlAqqad, S. Al Mamary, Y. Kadimati, A. Al Baik and W. Pitt, "Kinetics of acoustic release of doxorubicin from stabilized and unstabilized micelles and the effect of temperature", *Journal of the Franklin Institute*, vol. 348, no. 1, pp. 125-133, 2011.
- [52] G. A. Hussein, D. Velluto, L. Kherbeck, W. G. Pitt, J. A. Hubbell, and D. A. Christensen, "Investigating the acoustic release of doxorubicin from targeted micelles," *Colloids Surfaces B Biointerfaces*, vol. 101, pp. 153–155, 2013.
- [53] G. Hussein, L. Kherbeck, W. Pitt, J. Hubbell, D. Christensen and D. Velluto, "Kinetics of Ultrasonic Drug Delivery from Targeted Micelles", *Journal of Nanoscience and Nanotechnology*, vol. 15, no. 3, pp. 2099-2104, 2015.
- [54] G. A. Hussein, M. A. Diaz de la Rosa, T. Gabuji, Y. Zeng, D. A. Christensen, and W. G. Pitt, "Release of doxorubicin from unstabilized and stabilized micelles under the action of ultrasound," *J. Nanosci. Nanotechnol.*, vol. 7, no. 3, pp. 1028–1033, 2007.
- [55] N. Shahrin, "Solubility and Dissolution of Drug Product: A Review", *International Journal of Pharmaceutical and Life Sciences*, vol. 2, no. 1, pp. 33-41, 2013.
- [56] P. Deore, M. Pharm. I, Topic: "Theories of Dissolution," Faculty of Pharmacy, R. C. Patel Institute of Pharmaceutical Education and Research, Shirpur, India, Oct. 10, 2014.
- [57] D. Y. Arifin, L. Y. Lee, and C.-H. Wang, "Mathematical modeling and simulation of drug release from microspheres: Implications to drug delivery systems," *Adv. Drug Deliv. Rev.*, vol. 58, no. 12, pp. 1274–1325, 2006.
- [58] D. Stevenson-Abouelnasr, G. A. Hussein, and W. G. Pitt, "Further investigation of the mechanism of Doxorubicin release from P105 micelles using kinetic models," *Colloids Surfaces B Biointerfaces*, vol. 55, no. 1, pp. 59–66, 2007.
- [59] G. A. Hussein, N. M. Abdel-Jabbar, F. S. Mjalli, and W. G. Pitt, "Modeling and sensitivity analysis of acoustic release of Doxorubicin from unstabilized pluronic P105 using an artificial neural network model," *Technol. Cancer Res. Treat.*, vol. 6, no. 1, pp. 49–56, 2007.
- [60] G. Hussein, D. Stevenson-Abouelnasr, W. Pitt, K. Assaleh, L. Farahat and J. Fahadi, "Kinetics and thermodynamics of acoustic release of doxorubicin from non-stabilized polymeric micelles", *Colloids and Surfaces A: Physicochemical and Engineering Aspects*, vol. 359, no. 1-3, pp. 18-24, 2010.

- [61] G. A. Hussein, N. M. Abdel-Jabbar, F. S. Mjalli, W. G. Pitt, and A. Al-Mousa, "Optimizing the use of ultrasound to deliver chemotherapeutic agents to cancer cells from polymeric micelles," *J. Franklin Inst.*, vol. 348, no. 7, pp. 1276–1284, 2011.
- [62] M. A. Diaz de la Rosa, G. A. Hussein, and W. G. Pitt, "Comparing microbubble cavitation at 500 kHz and 70 kHz related to micellar drug delivery using ultrasound," *Ultrasonics*, vol. 53, no. 2, pp. 377–386, 2013.
- [63] M. A. Díaz de la Rosa, G. A. Hussein, and W. G. Pitt, "Mathematical modeling of microbubble cavitation at 70 kHz and the importance of the subharmonic in drug delivery from micelles," *Ultrasonics*, vol. 53, no. 1, pp. 97–110, 2013.
- [64] M. Abdel-Hafez and G. A. Hussein, "Predicting the Release of Chemotherapeutics From the Core of Polymeric Micelles Using Ultrasound," *IEEE Trans. Nanobioscience*, vol. 14, no. 4, pp. 378–384, 2015.
- [65] A. Abusara, M. Abdel-Hafez and G. Hussein, "Measuring the Acoustic Release of a Chemotherapeutic Agent from Folate-Targeted Polymeric Micelles", *Journal of Nanoscience and Nanotechnology*, vol. 18, no. 8, pp. 5511-5519, 2018.
- [66] C. C. Church, "Frequency, pulse length, and the mechanical index," *Acoust. Res. Lett. Online*, vol. 6, no. 3, pp. 162–168, Jun. 2005.
- [67] S.-J. Huang, S.-L. Sun, T.-H. Feng, K.-H. Sung, W.-L. Lui, and L.-F. Wang, "Folate-mediated chondroitin sulfate-Pluronic 127 nanogels as a drug carrier," *Eur. J. Pharm. Sci.*, vol. 38, no. 1, pp. 64–73, 2009.
- [68] N. A. Peppas, "Historical perspective on advanced drug delivery: How engineering design and mathematical modeling helped the field mature," *Adv. Drug Deliv. Rev.*, vol. 65, no. 1, pp. 5–9, 2013.
- [69] J. Siepmann and F. Siepmann, "Mathematical modeling of drug delivery," *Int. J. Pharm.*, vol. 364, no. 2, pp. 328–343, 2008.
- [70] S. Dash, P. Murthy, L. Nath, and P. Chowdhury, "Kinetic Modeling on Drug Release from Controlled Drug Delivery Systems," *Acta Pol. Pharm.*, vol. 67, no. 3, pp. 217–223, May 2010.
- [71] Y. Shi, A. Wan, Y. Shi, Y. Zhang and Y. Chen, "Experimental and Mathematical Studies on the Drug Release Properties of Aspirin Loaded Chitosan Nanoparticles", *BioMed Research International*, vol. 2014, pp. 1-8, 2014.

- [72] D. D. Allen, R. Caviedes, A. M. Cárdenas, T. Shimahara, J. Segura-Aguilar, and P. A. Caviedes, “Cell Lines as In Vitro Models for Drug Screening and Toxicity Studies,” *Drug Dev. Ind. Pharm.*, vol. 31, no. 8, pp. 757–768, 2005.
- [73] T. Higuchi, “Mechanism of sustained-action medication. Theoretical analysis of rate of release of solid drugs dispersed in solid matrices,” *J. Pharm. Sci.*, vol. 52, no. 12, pp. 1145–1149, 1963.
- [74] A. W. Hixson and J. H. Crowell, “Dependence of Reaction Velocity upon surface and Agitation,” *Ind. Eng. Chem.*, vol. 23, no. 8, pp. 923–931, 1931.
- [75] R. W. Korsmeyer, R. Gurny, E. Doelker, P. Buri, and N. A. Peppas, “Mechanisms of solute release from porous hydrophilic polymers,” *Int. J. Pharm.*, vol. 15, no. 1, pp. 25–35, 1983.
- [76] J. Siepmann and N. A. Peppas, “Modeling of drug release from delivery systems based on hydroxypropyl methylcellulose (HPMC),” *Adv. Drug Deliv. Rev.*, vol. 48, no. 2, pp. 139–157, 2001.
- [77] R. W. Baker and L. M. Sanders, “Controlled Release Delivery Systems,” in *Synthetic Membranes: Science, Engineering and Applications*, 1st ed., P. M. Bungay, H. K. Lonsdale, and M. N. de Pinho, Eds. Dordrecht: Springer Netherlands, 1986, pp. 581–624.
- [78] H. B. HOPFENBERG, “Controlled Release from Erodible Slabs, Cylinders, and Spheres,” in *Controlled Release Polymeric Formulations*, vol. 33, American Chemical Society, 1976, pp. 3–26.
- [79] F. Langenbucher, “Letters to the Editor: Linearization of dissolution rate curves by the Weibull distribution,” *J. Pharm. Pharmacol.*, vol. 24, no. 12, pp. 979–981, 1972.
- [80] W. Weibull, “A Statistical Distribution Function Of Wide Applicability,” *J. Appl. Mech.*, vol. 18, pp. 293–297, Jan. 1951.
- [81] Nature, “Statistical methods,” 2018. [Online]. Available: <https://www.nature.com/subjects/statistical-methods>, [May 6, 2020].
- [82] J. Bodycomb, “Interpreting and Understanding Dynamic Light Scattering Data.” Horiba, p. 29, 2012.
- [83] V. Thatipamula, A. Azmeer, and M. Nour, “Drug Release Models: Derivations and Linearization of Plots,” M.Sc. thesis, American University of Sharjah, United Arab Emirates, 2018.

- [84] T. Şen, O. Tüfekçioğlu, and Y. Koza, “Mechanical index,” *Anatol. J. Cardiol.*, vol. 15, no. 4, pp. 334–336, 2015.
- [85] A. Bouakaz, M. Versluis, and N. de Jong, “High-speed optical observations of contrast agent destruction,” *Ultrasound Med. Biol.*, vol. 31, no. 3, pp. 391–399, 2005.
- [86] P. Costa and J. M. Sousa Lobo, “Modeling and comparison of dissolution profiles,” *Eur. J. Pharm. Sci.*, vol. 13, no. 2, pp. 123–133, 2001.
- [87] K. Kosmidis, P. Argyrakis, and P. Macheras, “Fractal kinetics in drug release from finite fractal matrices,” *J. Chem. Phys.*, vol. 119, no. 12, pp. 6373–6377, 2003.
- [88] M. P. Paarakh, P. A. Jose, C. M. Setty, and G. V Peter, “Release kinetics—concepts and applications,” *Int. J. Pharm. Res. Technol*, vol. 10, no. 1, pp. 1–9, 2018.
- [89] M. Mahmoud, “The Effect of Ultrasound on the Drug Delivery of RGD-Targeted Liposomes,” M.Sc. thesis, American University of Sharjah, United Arab Emirates, 2018.
- [90] V. Shah, Y. Tsong, P. Sathe and R. Williams, "Dissolution Profile Comparison Using Similarity Factor, f_2 ", *Dissolution Technologies*, vol. 6, no. 3, pp. 15-15, 1999.
- [91] Thermo Fisher Scientific, “Chemistry of Protein Assays.” [Online]. Available: <https://www.thermofisher.com/ae/en/home/life-science/protein-biology/protein-biology-learning-center/protein-biology-resource-library/pierce-protein-methods/chemistry-protein-assays.html>, [May 6, 2020].
- [92] J. Crank, *The mathematics of diffusion*. Oxford [England]: Clarendon Press, 1975.

Vita

Youssef Ashraf Alhariri was born in 1995, in Dubai, in the United Arab Emirates (UAE). He received his primary and secondary education in Ajman, UAE. He completed his internship at Universal Lubricants in Sharjah, UAE. He received his B.Sc. degree in Chemical Engineering from the American University of Sharjah in 2017. In January 2018, he joined the Chemical Engineering master's program in the American University of Sharjah. He was awarded a graduate assistantship that allowed him to work as a graduate teaching and research assistant from 2018 till 2020. His research interests are in (e.g. drug delivery, biocompatible electrodes, and particle technology).